



Interatomic bonds and the tensile anisotropy of trialuminides in the elastic limit: A density functional study for $\text{Al}_3(\text{Sc}, \text{Ti}, \text{V}, \text{Cr})$

Michal Jahnatek, Marian Krajci, Juergen Hafner

► To cite this version:

Michal Jahnatek, Marian Krajci, Juergen Hafner. Interatomic bonds and the tensile anisotropy of trialuminides in the elastic limit: A density functional study for $\text{Al}_3(\text{Sc}, \text{Ti}, \text{V}, \text{Cr})$. Philosophical Magazine, 2007, 87 (11), pp.1769-1794. 10.1080/14786430601057946 . hal-00513800

HAL Id: hal-00513800

<https://hal.science/hal-00513800>

Submitted on 1 Sep 2010

HAL is a multi-disciplinary open access archive for the deposit and dissemination of scientific research documents, whether they are published or not. The documents may come from teaching and research institutions in France or abroad, or from public or private research centers.

L'archive ouverte pluridisciplinaire **HAL**, est destinée au dépôt et à la diffusion de documents scientifiques de niveau recherche, publiés ou non, émanant des établissements d'enseignement et de recherche français ou étrangers, des laboratoires publics ou privés.



**Interatomic bonds and the tensile anisotropy of
trialuminides in the elastic limit: A density functional study
for $\text{Al}_3(\text{Sc,Ti,V,Cr})$**

Journal:	<i>Philosophical Magazine & Philosophical Magazine Letters</i>
Manuscript ID:	TPHM-06-Aug-0275.R2
Journal Selection:	Philosophical Magazine
Date Submitted by the Author:	27-Sep-2006
Complete List of Authors:	Jahnatek, Michal; University of Vienna, Institute of Material Physics; Slovak Academy of Sciences, Institute of Physics Krajci, Marian; Slovak Academy of Sciences, Institute of Physics; University of Vienna, Center for Computational Materials Science Hafner, Juergen; University of Vienna, Institute of Material Physics
Keywords:	aluminium alloys, anisotropic elasticity, atomistic simulation, computer modelling, density-functional methods
Keywords (user supplied):	
Note: The following files were submitted by the author for peer review, but cannot be converted to PDF. You must view these files (e.g. movies) online.	
al3xym.tex figures.tex tables.tex	

1
2
3
4
5
6
7
8
9
10
11
12
13
14
15
16
17
18
19
20
21
22
23
24
25
26
27
28
29
30
31
32
33
34
35
36
37
38
39
40
41
42
43
44
45
46
47
48
49
50
51
52
53
54
55
56
57
58
59
60

For Peer Review Only

Inter-atomic bonds and the tensile anisotropy of trialuminides in the elastic limit: A density functional study for $\text{Al}_3(\text{Sc}, \text{Ti}, \text{V}, \text{Cr})$

M. JAHNÁTEK ^{*†‡}, M. KRAJČÍ^{†‡} and J. HAFNER[†],

[†] Institut für Materialphysik and Center for Computational Materials Science, Universität Wien, Sensengasse 8/12,
A-1090 Wien, Austria

[‡] Institute of Physics, Slovak Academy of Sciences, Dúbravská cesta 9, SK-84511 Bratislava, Slovak Republic

(September 27, 2006)

The tensile anisotropy in the elastic limit of $\text{Al}_3(\text{Sc}, \text{Ti}, \text{V}, \text{Cr})$ intermetallic compounds in both $L1_2$ and $D0_{22}$ crystal structure have been investigated using first-principles density-functional calculations. In both crystal structures the main bonding character comes from the saturation of dominant d^3 ($L1_2$) and d^4 ($D0_{22}$) hybrid orbitals located on the TM atoms. The series $\text{Al}_3\text{Sc} \rightarrow \text{Al}_3\text{V}$ corresponds to the gradually d -band filling and leads to a gradual increase of bond-strength and covalent bond formation. The magnetism of Cr breaks this trend in the Al_3Cr compound (for both ferromagnetic and anti-ferromagnetic configurations). In this series, a trend towards an increased anisotropy of the elastic constants, Young modulus Y and Poisson ratio ν is observed. The easy and hard directions of tension can be simply identified by the variation of Y , which corresponds to the presence or absence of covalently bonded $-\text{Al}-\text{TM}-$ chains. A high anisotropy of Poisson ratio arises also from an alternation of atoms in the lateral directions and can be understood in the same terms.

1 Introduction

Aluminium-rich compounds with transition-metal (TM) elements have attracted wide attention due to the need for high-performance structural materials in the aerospace, aircraft, and automobile industries. Trialuminides (Al_3TM) are among the most promising candidates. Mainly the compounds with the first three early transition elements ($\text{TM} = \text{Sc}, \text{Ti}, \text{V}$) are of interest for lightweight structural applications. Trialuminides meet several exacting demands like light-weight, low density, good thermal conductivity, high melting point, acceptable low-temperature damage tolerance, sufficient creep resistance, high specific strength and moduli [1–3], oxidation resistance, low diffusivity and solubility in aluminium resulting in low coarsening rate at elevated temperature, etc. In many respects, trialuminides are competitive with the currently used Ni-base super-alloys [4]. However, trialuminides are extremely brittle at low temperature. This drawback limits their practical application and extensive experimental efforts aim to make these compounds ductile at room temperature.

The $\text{Al}_3(\text{Sc}, \text{Ti}, \text{V})$ series of trialuminides crystallises in the cubic $L1_2$ (space group $Pm\bar{3}m, \#221$) and tetragonal $D0_{22}$ (space group $I4/mmm, \#139$) crystal structures [5]. Al_3Cr represents a hypothetical phase, which exists in none of both crystal structures. We used it just to extend the series and to generalise the observed trends. The low symmetry of the $D0_{22}$ structure is often considered as the main reason for the poor ductility of $\text{Al}_3(\text{Ti}, \text{V})$. Their low ductility is probably associated with an insufficient number of slip systems in polycrystalline aggregates [6]. In contrast, the $L1_2$ structure has higher symmetry and hence a larger number of slip systems as required for better ductility. Therefore attempts have been made to transform the $D0_{22}$ into the $L1_2$ structure by the addition of ternary elements [7–10]. However, preliminary results for the stable Al_3Sc ($L1_2$) compound are not encouraging. The stable Al_3Sc ($L1_2$) fractures in an extremely brittle manner by transgranular cleavage along $\{110\}$ planes [11]. Single phase samples of Al_3Ti ($L1_2$) also do not show high ductility [12] and $L1_2$ -phase Al_3V [13] has been not produced as yet.

Since experiment shows that the mere conversion of $D0_{22}$ into $L1_2$ will not lead to a good ductility of trialuminides, a better understanding of the intrinsic mechanisms causing their brittleness is necessary.

*Corresponding author. Email: michal.jahnatek@univie.ac.at

We have recently performed detailed *ab-initio* studies of the crystal and electronic structures of $\text{Al}_3(\text{Ti}, \text{V})$ both in the $D0_{22}$ and $L1_2$ phases, i.e. in a stable and a metastable phase [14, 15]. In both structures we found an enhanced charge density along the Al-(V,Ti) bonds, a characteristic feature of covalent bonding. A strong directional bonding has been suggested also by NMR studies [16–19] of Al_3V and the structural analysis: short Al-V distances [20] indicate that the bonding may have a covalent character. The COOP (Crystal Orbital Overlap Population) analysis [21] reveals that the bonds in Al_3V are more saturated and stronger than the corresponding bonds in Al_3Ti (because of a higher *d*-band filling) and the high symmetry of the transition-metal sites in the $L1_2$ structure leads to higher metallicity of alloys assuming this structure. The enhanced covalency of bonds between Al and transition metals in transition-metal aluminides has a significant influence on the mechanical properties in two respects. Covalency increases the bond strength [14, 22] and consequently leads to higher mechanical strength and hardness, but on the other hand it leads also to an undesired higher brittleness.

In this paper we present results of an *ab-initio* investigation of the mechanical properties of $\text{Al}_3(\text{Sc}, \text{Ti}, \text{V}, \text{Cr})$ compounds with the $D0_{22}$ and $L1_2$ structures in the elastic limit. We consider this study as the first step of an investigation of the intrinsic properties of these compounds causing their brittleness. It has been suggested that the transformation from the stable low-symmetry $D0_{22}$ structure to the more symmetric $L1_2$ structure could be sufficient to satisfy the von Mises criterion for slip deformation [23]. Although this may be considered as a rather naive attempt, in some case modest improvements have been achieved [8]. In general, brittle or ductile behaviour depends on the competition between cleavage and shear slip, and hence on the maximum stress sustained by the material. Furthermore, beyond an exclusively microscopic picture, the fracture mechanics of a material depends on factors such as the formation and mobility of dislocations, length of Burgers, surface energies etc. [8, 24]. The present study, however, has been deliberately limited to the elastic region, where the elastic constants are sufficient to characterise the mechanical properties. Our aim is to explain the differences and similarities between these alloys in terms of the picture of their chemical bonding which we have recently presented [14, 15]. We concentrate on the Young modulus Y and the Poisson ratio ν which are directly related to the tensile deformation. Although this paper deals with the ideal crystal structures only, our results are relevant for polycrystalline samples as well, as the single-crystalline grains represent the main strengthening components [25, 26] of polycrystalline aggregates. The effective elastic constants of polycrystalline materials can be derived from the single-crystal elastic constants by various averaging methods [27–31].

2 Computational methodology

In the present paper all results are obtained using density-functional theory (DFT) as implemented in the Vienna *ab-initio* simulation package (VASP) [32, 33], based on the projector-augmented-wave (PAW) method [34, 35]. We used the generalised gradient approximation (GGA) to the exchange-correlation functional according to Perdew *et al.* [36] (known as PW91). For all elements we used the standard PAW pseudopotentials (PP) distributed by VASP with reference configurations $_{13}\text{Al}$: [Ne] $3s^2 3p^1$, $_{21}\text{Sc}$: [Ar] $3d^2 4s^1$, $_{22}\text{Ti}$: [Ar] $3d^3 4s^1$, $_{23}\text{V}$: [Ar] $3d^4 4s^1$, and $_{24}\text{Cr}$: [Ar] $3d^5 4s^1$. The plane-wave basis set contained components with energies up to 300, 194, 222, 240, and 284 eV for Al(fcc) and $\text{Al}_3(\text{Sc}, \text{Ti}, \text{V}, \text{Cr})$, respectively. The Brillouin zone (BZ) was sampled using $25 \times 25 \times 25$ meshes for the cubic $L1_2$ structures and $20 \times 20 \times 10$ meshes for the tetragonal $D0_{22}$ structures, constructed according to Monkhorst-Pack scheme [37]. The integration over the BZ used the tetrahedron method with Blöchl corrections [38]. The total energy was calculated with a high precision, converged to 10^{-7} eV/atom. The partial (projected) density of states (PDOS) were calculated from the projections of wavefunctions onto spherical harmonics centred at the position of the ions within atom-centred spheres with radii of 1.402, 1.312, and 1.323 Å for Al, Sc, and (Ti, V, Cr), respectively. For Al_3Cr the local magnetic moments were calculated by integrating the magnetisation densities within the same atom-centred spheres through a spin-polarised DFT approach using the spin interpolation formula of Vosko, Wilk, and Nusair [39].

For the calculation of the elastic constants we used the symmetry-general least-squares extraction method proposed by Le Page and Saxe [40] in connection with VASP. This novel method allows an automated approach to the calculation the elastic constants for crystals of arbitrary symmetry. The input

consists of a set of values of the total energy for special strained states of the crystal. For cubic $L1_2$ symmetry we applied the strains $\pm\epsilon_1$, $\epsilon_1 \pm \epsilon_2$, and $\pm\epsilon_4$; for tetragonal $D0_{22}$ symmetry we add the strains $\epsilon_1 \pm \epsilon_3$, $\pm\epsilon_3$, and $\pm\epsilon_6$. For each set of strains $\pm\epsilon_i$ three different magnitudes 0.25%, 0.5% and 0.75% were used. The small total energy differences between the strained states ask for calculation with a very high precision as stated before.

3 Crystal structure and inter-atomic bonding

The $\text{Al}_3(\text{Sc,Ti,V,Cr})$ trialuminides have been investigated in two possible crystal structures — cubic $L1_2$ ($Pm\bar{3}m, \#221$) and tetragonal $D0_{22}$ ($I4/mmm, \#139$). All computed structural parameters are collected in Tab. 1. The Al_3Ti and Al_3V compounds are stable in the $D0_{22}$ crystal structure, while Al_3Sc favours the $L1_2$ structure [5]. The Al_3Cr compound does not exist in any of these crystal structures. The $D0_{22}$ structure in the anti-ferromagnetic configuration was found to be lower in energy by ~ 174 meV than the ferromagnetic phase. In the ferromagnetic state, both the $L1_2$ and the $D0_{22}$ phases exhibit a high spin magnetic moment of the chromium atoms (2.57 and $1.98\mu_B$, respectively). The anti-ferromagnetic configuration of $D0_{22}$ structure leads to lower values of the spin magnetic moments ($\pm 1.87\mu_B$).

The bonding picture of both $L1_2$ and $D0_{22}$ crystal structures was analysed in our previous work [14,15]. We briefly recapitulate the basic facts of this picture and include some novel facets. A comprehensive analysis of the stability of $\text{Al}_3(\text{Sc,Ti})$ interpreted in a chemical language of inter-atomic bonding was performed recently by Bester and Fähnle [41] and leads to the same conclusion. A similar new look at the bonding in trialuminides has been presented also by Condon *et al.* [42].

3.1 $L1_2$ structure

The $L1_2$ ($Pm\bar{3}m, \#221$, *Strukturbericht* Cu_3Au) structure has all atoms located on the sites of a face-centred-cubic lattice, see Fig. 1(left). TM atoms are located at the cell corners, aluminium atoms occupy the face centres. There is one Al-site (3c) and one TM-site (1a). In this usual orientation it can be viewed as an $-ABAB-$ stacking of the A and B planes; where the plane A consists of Al and TM atoms occupying vertices of a square network and the plane B consists of Al atoms only. Each TM atom is surrounded by 12 equivalent aluminium nearest neighbours forming a regular cuboctahedron. Hence it has full O_h point symmetry.

The bonding picture in the $L1_2$ structure is relatively simple as here only one type of bonding exists, namely TM-Al bonding. In our previous work [14,15] we have shown that bonding results from the overlap of d -orbitals with e_g symmetry from the TM side and sp^2d hybrid orbitals from the Al side. The COOP analysis shows a very weak saturation by electrons. The nearest-neighbour shell of the TM-site with full O_h symmetry leads to the well know e_g-t_{2g} splitting of d -orbitals in a local field of octahedral geometry. The symmetrised hybrid orbitals are oriented from the central TM atom to the twelve Al atoms located at vertices of the cuboctahedron. These orbitals form the basis of a reducible representation Γ^{hyb} of the O_h group. Reduction yields four one-dimensional representations (A_{1g} , A_{1u} , A_{2g} , A_{2u}), two two-dimensional representations (E_g and E_u), and four three-dimensional (T_{1g} , T_{1u} , T_{2g} , T_{2u}) representations. The assignment of atomic orbitals to irreducible representations with the same transformation properties is $\Gamma^{\text{hyb}} = A_{1g} \oplus E_g \oplus T_{1u} \oplus T_{2g} \oplus T_{1u}$; where A_{1g} : s , E_g : (d_{z^2} , $d_{x^2-y^2}$), T_{1u} : (p_x, p_y, p_z) or ($f_{x^3}, f_{y^3}, f_{z^3}$), T_{2g} : (d_{xy}, d_{xz}, d_{yz}), T_{2u} : [$f_{x(z^2-y^2)}$, $f_{y(z^2-x^2)}$, $f_{z(x^2-y^2)}$]. This leads to $sp^3d^5f^3$ or sd^5f^6 hybrid orbitals on the TM atom [43]. It can be shown that the contribution of p and f states to the TM atom density of states (DOS) is negligible. Therefore sd^5 hybridisation dominates the bonding (the contribution of s states is also small, hence a d^5 dominant hybridisation can be considered too). In this case (considering that there are only s and d orbitals on the TM atom), the hybrid irreducible representation can be expressed as $\Gamma^{\text{hyb}} = A_{1g} \oplus E_g \oplus T_{2g}$. The preference for specific bonding directions of sd^5 hybrids is hard to follow, hence a decomposition according to the D_{3d} and D_{4h} subgroups of O_h symmetry is useful and leads to a series of hybrid orbitals located around three-fold and four-fold rotational axes.

3.1.1 Decomposition according to D_{3d} symmetry. The cuboctahedron has four three-fold axes ($4C_3$) oriented along the $\langle 111 \rangle$ directions of the cubic $L1_2$ cell. In this direction the $L1_2$ structure can be viewed as $-CDE-$ stacking of close-packed planes, where Al and TM atoms occupy vertices of a hexagonal network. For the analysis we rotate the bonding configuration around a TM atom in such a way that the three-fold axis along the $[111]$ direction coincides with the z -axis [Fig. 2(a)]. Omitting the 6 atoms from the basal plane ($z=0$), the point-group symmetry of bonding configuration of the TM atom can be identified as D_{3d} . Since the O_h symmetry of cuboctahedron correlates with D_{3d} symmetry, the irreducible representation created by the sd^5 hybrids can be directly rewritten¹ as $\Gamma^{\text{hyb}} = 2A_{1g} \oplus 2E_g$; where A_{1g} : s or d_{z^2} , E_g : $(d_{x^2-y^2}, d_{xy})$ or (d_{yz}, d_{zx}) . The resulting irreducible representation can be written as $\Gamma^{\text{hyb}} = (A_{1g} \oplus E_g) \oplus (A_{1g} \oplus E_g)$, indicating that the two different $A_{1g} \oplus E_g$ hybridisations are active at the same time. Each of them represents a d^3 or sd^2 hybrid orbital. For our bonding geometry, this decomposition has a simple interpretation: (i) The d^3 hybrids formed by d_{z^2} , d_{yz} , d_{zx} atomic orbitals act along the z axis and create inter-planar $-C-D-E-$ bonds between hexagonal planes. They promote the formation of 6 bonds oriented from one TM atom in plane D to 6 aluminium atoms in planes C and E (3 on top and 3 on bottom) [Fig. 2(a)]. We note that this type of bonding is typical for all aluminium-rich vanadium compounds and is able to form $-Al-V-$ chains of covalent bonds (forming, e.g., the tetrahedral network in $Al_{10}V$ [22], via the overlap of $V(sd^3)-Al(sp)$ hybrid orbitals). Aluminium atoms form sp hybrids. (ii) The remaining atomic orbitals, i.e. s , $d_{x^2-y^2}$, d_{xy} , form sd^2 hybrids and independently act in the basal plane ($z=0$), producing in-plane bonds between the central TM atom and the surrounding 6 Al atoms in plane D forming sp^2 hybrids. We note that since the C, D, and E planes are qualitatively equivalent the same in-planar bonds are active in all of them.

3.1.2 Decomposition according to D_{4h} symmetry. The orientation of the cuboctahedron around each site in the $L1_2$ structure leads to the coincidence of its three four-fold axes ($3C_4$) with the three $\langle 100 \rangle$ directions. Along these axes the $L1_2$ structure can be viewed as an $-ABAB-$ stacking of A and B planes. Taking the $[001]$ direction as one of the four-fold axes and omitting the 4 nearest Al atoms of the central TM atom in the basal plane A ($z=0$), the point-group symmetry of the bonding configuration of the TM atom with the 8 aluminium atoms (4 top and 4 bottom) in the B planes is D_{4h} [Fig. 2(b)]. The O_h symmetry of the cuboctahedron also contains the D_{4h} group, hence the irreducible representation in the basis of the sd^5 hybrids can be rewritten¹ as $\Gamma^{\text{hyb}} = 2A_{1g} \oplus E_g \oplus B_{1g} \oplus B_{2g}$; where A_{1g} : s or d_{z^2} , E_g : (d_{yz}, d_{zx}) , B_{1g} : $d_{x^2-y^2}$, and B_{2g} : d_{xy} . This representation can be rewritten as $\Gamma^{\text{hyb}} = (A_{1g} \oplus E_g \oplus B_{1g}) \oplus (A_{1g} \oplus B_{2g})$, indicating that two hybridisations are active at the same time: (i) The first, $A_{1g} \oplus E_g \oplus B_{1g}$, leads to the formation of d^4 hybrids of d_{z^2} , d_{yz} , d_{zx} , and $d_{x^2-y^2}$ atomic orbitals; promoting the formation of 8 bonds oriented from the central TM atom in plane A or A' towards 8 aluminium atoms from two B planes (4 on top and 4 on bottom) [Fig. 2(b)]. We note that this type of bonding is active also in the $D0_{22}$ structure. The TM d^4 hybrids overlap with sp^3 hybrids on the Al sites. (ii) The second representation, $A_{1g} \oplus B_{2g}$, leads to sd hybrids of s and d_{xy} atomic orbitals located on the TM atom. These hybrid orbitals form in-planar bonds between a TM atom and 4 aluminium atoms via sp^2 hybrids.

3.2 $D0_{22}$ structure

The $D0_{22}$ (*Immm*, #139, *Strukturbericht* Al_3Ti) crystal structure has a tetragonal elementary cell which can be considered as a consisting of two $L1_2$ cubes stacked along the z direction, with a $[\frac{1}{2}, \frac{1}{2}, 0]$ anti-phase shift between these cubes [44], see Fig. 1(right). There are one TM crystallographic site (2a) and two aluminium sites Al_1 (2b) and Al_2 (4d). The structure can be viewed as a stacking of two types of planes. Plane A consists of Al_1 and TM atoms occupying the vertices of a square network, plane B consists of Al_2 atoms only. The stacking of the planes is $-ABA'B-$, where A' is an A plane shifted horizontally with respect to A by half of a square diagonal. Considering only nearest neighbours, the point-group symmetry

¹Using the correlation table $O_h:A_{1g} \rightarrow D_{3d}:A_{1g}$, $O_h:E_g \rightarrow D_{3d}:E_g$, $O_h:T_{2g} \rightarrow D_{3d}:A_{1g} \oplus E_g$.

¹Using the correlation table $O_h:A_{1g} \rightarrow D_{4h}:A_{1g}$, $O_h:E_g \rightarrow D_{4h}:A_{1g} \oplus B_{1g}$, $O_h:T_{2g} \rightarrow D_{4h}:B_{2g} \oplus E_g$.

of the TM-site would be O_h , but nonequivalent neighbours from the second and higher shells reduce the point-group symmetry to D_{4h} . Although bonding in the $D0_{22}$ structure was discussed elsewhere [14], we recapitulate the main results and confront them to our analysis of bonding in the $L1_2$ structure.

The coordination polyhedron around a TM site is a tetragonally deformed cuboctahedron (in the orientation where $\langle 001 \rangle$ directions coincide with its four-fold axes). The basal plane corresponds to plane A or A'. The TM atoms in this plane interact with 4 nearest neighbour Al_1 atoms situated in the same plane [see dot-dashed line segments on the Fig. 1 (right)] and with 8 Al_2 atoms (4 on top and 4 on bottom) in two B planes located [dashed lines on the Fig. 1 (right)]. Two sets of hybridised orbitals oriented from the central TM atom to the 8 Al_2 atoms and 4 Al_1 atoms form a reducible representation Γ^{hyb} of the D_{4h} group. As was shown previously [14]: (i) The first bonding geometry (TM–8 Al_2 , an inter-planar –B–A'–B–bonds) results from the reduction to irreducible representations in $\Gamma^{hyb} = A_{1g} \oplus A_{2u} \oplus B_{1g} \oplus B_{2u} \oplus E_g \oplus E_u$; and based on sp^3d^3f or p^3d^4f hybrid orbitals on the TM atom. Considering only s and d orbitals (since the contributions of p and f states to the TM atom DOS are negligible), sd^3 or d^4 hybrids remain (the active irreducible representation is $\Gamma^{hyb} = A_{1g} \oplus E_g \oplus B_{1g}$). This corresponds to the inter-planar bonding in the $L1_2$ structure as derived by decomposition according to D_{4h} symmetry. On the Al_2 side sp^3 hybridisation is active. It was shown that the main bonding contribution from d^4 hybrids comes from the d_{zx} and d_{yz} components. The COOP analysis reveals a full saturation by electrons in case of Al_3V . In series $Al_3V \rightarrow Al_3Sc$ this saturation decreases. (ii) The bonding between the central TM atom and the four Al_1 atoms in planes A or A' was previously identified as resulting from the overlap of symmetrised hybrid sp^2d orbitals centred on all Al_1 and TM atoms. However, the contribution of s and p states in case of the TM atom is negligible, hence the d_{xy} orbital is dominant. Generally it represents sd hybridisation (the active irreducible representation is $\Gamma^{hyb} = A_{1g} \oplus B_{2g}$), corresponding to the in-planar bonding in $L1_2$ structure obtained by decomposition according to D_{4h} symmetry. For Al_3V the COOP analysis shows that the states below the Fermi level have almost completely bonding character while above the Fermi level the states are anti-bonding. For $Al_3(Sc,Ti)$ the bonding orbitals are not fully saturated. Finally, in plane B each Al_2 atom interacts with four Al_2 neighbours. These bonds are formed by the overlap of sp^2d symmetrised hybrid orbitals centred on all Al_2 atoms. Although the bond exhibits enhanced covalency, it is only partially populated by electrons.

4 Elastic anisotropy

The anisotropic behaviour of the Young modulus (Y) and Poisson ratio (ν) can be calculated using the general transformation rule for fourth-order tensors [45–47]. Following Cazzani and Rovati [48, 49], the reciprocal value of Young modulus for uniaxial tension in the direction of the unit vector \mathbf{n} can be expressed as

$$\varepsilon(\mathbf{n}) = \frac{1}{Y(\mathbf{n})} = \mathbf{n} \otimes \mathbf{n} \cdot \mathbf{S}[\mathbf{n} \otimes \mathbf{n}], \quad (1)$$

where \otimes and dot denote the dyadic and the inner product, respectively. The expression $\mathbf{S}[\mathbf{n} \otimes \mathbf{n}]$ represents an associated strain field ε due to the stress field $\sigma = \mathbf{n} \otimes \mathbf{n}$ according to Hookes law, e.i. $\varepsilon = \mathbf{S}\sigma$ or $\sigma = \mathbf{C}\varepsilon$, where $\mathbf{S} = \mathbf{C}^{-1}$. The \mathbf{S} and \mathbf{C} represents the fourth-order compliance and elastic tensors, respectively. If an orthogonal Cartesian reference frame is considered, the expression (1) transforms to

$$Y(\mathbf{n}) = \frac{1}{n_i n_j S_{ijkl} n_k n_l}, \quad (2)$$

where the indices i, j, k, l run from 1 to 3, and the usual sum rule over repeated subscript is assumed.

The Poisson ratio is defined as the negative ratio between transversal and longitudinal strain. Supposing two orthogonal unit vectors \mathbf{m} and \mathbf{n} (i.e. $\mathbf{m} \cdot \mathbf{n} = 0$), where the vector \mathbf{n} is oriented in the direction of tension (longitudinal strain) and the vector \mathbf{m} in the direction of transversal strain, the Poisson ratio can

be expressed as [50]

$$\nu(\mathbf{n}, \mathbf{m}) = -\frac{\varepsilon(\mathbf{m})}{\varepsilon(\mathbf{n})} = -\frac{\mathbf{m} \otimes \mathbf{m} \cdot \mathbf{S}[\mathbf{n} \otimes \mathbf{n}]}{\mathbf{n} \otimes \mathbf{n} \cdot \mathbf{S}[\mathbf{n} \otimes \mathbf{n}]}, \quad (3)$$

where $\varepsilon(\mathbf{m})$ and $\varepsilon(\mathbf{n})$ represents the transversal and longitudinal strain due to the stress field $\sigma = \mathbf{n} \otimes \mathbf{n}$; they are expressed by projecting of the stress field along the direction of \mathbf{n} and \mathbf{m} vectors. In the Cartesian reference frame we have

$$\nu(\mathbf{n}, \mathbf{m}) = -\frac{m_i m_j S_{ijkl} n_k n_l}{n_m n_n S_{mnop} n_o n_p}. \quad (4)$$

5 Results and discussion

5.1 Variation of bonding with *d*-band filling

In Sec. 3 we have analysed bonding in the both $L1_2$ and $D0_{22}$ crystal structures from the symmetry point of view. This description suggests the formation of covalent bonds. We now analyse how this picture is realized in real alloys. In the series $\text{Al}_3\text{Sc} \rightarrow \text{Al}_3\text{V}$ we expect that the gradual filling of the *d*-band results in the saturation of in-planar and inter-planar bonds.

5.1.1 $L1_2$ structures. Fig. 3 shows the total and partial density of states (DOS and PDOS) of $\text{Al}_3(\text{Sc}, \text{Ti}, \text{V}, \text{Cr}^{\text{fm}})$ in the $L1_2$ crystal structure. To analyse the bonding properties, we show the contributions of the *d* atomic orbitals localised on the TM atom, grouped into two contributions according to the decomposition of the sd^5 hybrid orbitals under D_{3d} symmetry. It is clearly seen that the d_{z^2} , d_{yz} , and d_{zx} atomic orbitals (leading to d^3 hybridisation) are occupied already at a low degree of band filling. As the number of *d*-electrons increases, no qualitative change is observed. The orientation of the d^3 hybrid orbitals suggests a concentration of charge along the $\langle 111 \rangle$ directions, i.e. in the inter-planar –CDE– region, between the hexagonal C, D, and E planes. The population of d_{xy} and $d_{x^2-y^2}$ atomic orbitals (leading with the *s* orbital to sd^2 hybridisation) increases only gradually by addition of *d* electrons. The dominant contribution in the series $\text{Al}_3\text{Sc} \rightarrow \text{Al}_3\text{V}$, comes from the d_{xy} orbital. The contribution of the $d_{x^2-y^2}$ orbital can be identified with the dominant peak in the PDOS which is located above the Fermi level (E_F) in Al_3Sc , but overlaps with E_F in Al_3Ti and Al_3V . This shows that the inter-planar bonds between C, D, and E planes are strong already for insufficient *d*-band filling, strong in-planar bonding is achieved only at an increased number of *d*-electrons.

A similar analysis shows (based in the decomposition of the sd^5 hybrids according to D_{4h} symmetry) that in-planar bonding (based on *s* and d_{xy} states) is strong already in Al_3Sc , while the gradual filling of the *d*-band adds strength to the bonds between atoms in A (A') and B planes.

Including the Al_3Cr compound in the series $\text{Al}_3(\text{Sc}, \text{Ti}, \text{V})$ shows the limits of the saturation process. The COOP analysis of bonding through d^3 hybrids [22] or a d_{xy} atomic orbital [14] located on the TM atom with the Al atoms has shown that almost full saturation is achieved already for Al_3V with only non-bonding states above Fermi level in a narrow energy range. Therefore, adding more *d*-electrons (as for Al_3Cr) leads to the occupation of non-bonding E_g and later anti-bonding T_{2g} states. Moreover, the magnetism of Cr atoms leads to substantial redistribution of charge and negatively affects conditions for covalent bond formation.

5.1.2 $D0_{22}$ structures. Fig. 4 shows the DOS and PDOS of $\text{Al}_3(\text{Sc}, \text{Ti}, \text{V}, \text{Cr}^{\text{fm}}, \text{Cr}^{\text{afm}})$ in the $D0_{22}$ crystal structure. The contributions of the *d* atomic orbitals localised on the TM atom are grouped into two contributions d^4 and sd — according to the decomposition of the sd^5 hybrid orbitals under D_{4h} symmetry. As can be seen the dominant d^4 hybrids are well occupied already at a low band filling (case of Al_3Sc). The occupation of the d_{xy} atomic orbital (leading with the *s* orbital to sd hybridisation) is

small for the same case. The major contribution of the d^4 hybrids comes from the d_{z^2} , d_{yz} , and d_{zx} atomic orbitals (in accordance with d^3 hybrids in $L1_2$ structure). The additional $d_{x^2-y^2}$ atomic orbital donation can be identified with the dominant peak located in the PDOS above the Fermi level. The region between E_F and the dominant peak is characterised by the formation of deep pseudo-gap. It was show elsewhere that this feature is associated with the formation of inter-planar $-B-A'-B-$ covalent bonds [15].

The series $Al_3Sc \rightarrow Al_3V$, connected with increasing d -band filling, leads to higher occupation of both d^4 and sd hybrids. An important qualitative change is the shift of the position of the pseudo-gap closer to the E_F and its increasing depth. The saturation process leads finally to the formation of in-planar and inter-planar covalent bonds and of a deep pseudo-gap at E_F (for Al_3V). In this case, the COOP analysis [14, 15] exhibits full saturation of both bonding geometries with only non-bonding states above Fermi level in a narrow energy range. The presence of well saturated d^3 hybrids (as part of the d^4 hybrids) at a low saturated d -band indicates strong inter-planar bonds between $\{112\}$ planes (and higher resistance against tension along $\langle 112 \rangle$ directions). For lower occupation of sd hybrids, i.e. $Al_3(Sc, Ti)$, there exists only weak (almost no) in-planar bonds in A or A' planes.

The limits of the saturation process can be noticed in the DOS and PDOS of the Al_3Cr compound. Further addition of d -electrons leads to the occupation of non-bonding (A_{1g}, B_{1g}) and later anti-bonding (B_{2g}, E_g) states. Similar to $L1_2$ the magnetism of Cr atoms caused an substantial redistribution of charge and worsens the conditions for covalent bond formation.

5.2 Elastic constants – trends

All technical details about our calculations of the elastic constants have been described already in Sec. 2. The final values are collected in Tab. 1. The presence of the strong inter-atomic bonds can be read from the trends in the elastic constants presented in Fig. 5. First of all, the increasing strength of inter-atomic bonds can be seen in the trend of the bulk modulus B [Fig. 5(a)], where all bonds collectively act against the volume deformation. We note that the trends in B for both crystal structures are almost identical, since the values of bulk modulus do not differ substantially. B decreases for Al_3Cr due to the over-saturation of bonds, anti-bonding states occupation and magnetic effects.

The consequences of strong directional inter-atomic bonds can be seen in the trends of the c_{11} and c_{33} elastic constants of the $D0_{22}$ structures [Figs. 5(f,g)]. Both c_{11} and c_{33} measure the resistance against tension in x and z directions, respectively, and the increasing trend indicates the gradual strengthening of bonds acting along these directions. The increase of c_{33} (158→216→258 GPa) reflects the saturation of inter-planar ($-BA'B-$) bonds (as well as saturation of d^4 hybrids); the increase of c_{11} (158→192→233 GPa) arises from the strengthening of the in-plane bonds in A and A' planes (as well as saturation of d_{xy} atomic orbital on the TM-site). The monotonous increase is broken for Al_3Cr . The trends in the other elastic constants, see Figs. 5(e,h,i,j), are not so striking, but a small increase at increasing d -band filling can be noticed in all of them, except for c_{13} which remains constant. The elastic shear constants c_{44} and c_{66} also determine the values of the shear modulus for two shear systems: $G_4 = c_{44}$ for (001)[010] and $G_6 = c_{66}$ for (010)[100]. Hence increasing values of the elastic shear constants lead to a reduced shear mobility required for ductile behaviour.

The trends in the elastic constant are different for the $L1_2$ structures. The initial increase of c_{11} (179→192→178 GPa) [Fig. 5(b)] is disturbed by a small decrease for Al_3V . Later we will show than this decline is connected to a reconfiguration of bonds as a consequence of saturation. A systematic increase of c_{12} can be noticed also for this crystal structure, indicating a strong correlation between tension and lateral contraction. The constant values of $c_{44} = G$ indicate small changes in the elasto-plastic properties. We note that the ferromagnetic Al_3Cr compound has almost the same elastic properties as Al_3Ti (see Tab. 1).

All calculated elastic constants were checked for the consistency. There exists two consistency tests. First, the bulk modulus B can be computed from the elastic constants and independently also from the energy vs. volume curve. In this case, we obtained an excellent agreement between these two approaches. Second, the Young modulus Y can be computed from the elastic constants (2) and also extracted from the stress-strain curves for uniaxial tensile deformation as the slope of this curve at the origin. We obtained an

excellent agreement too. These results together with others analysis of trialuminides under tensile loading beyond the elastic limit will be published later. Moreover our computed values can be directly compared to experimental values, e.g. Al [51,52], Al₃Ti [53], Ni₃Al [54], or to the computed values by other authors, e.g. Al [40], Al₃Sc [55], Al₃Ti [55,56], Ni₃Al [54]. Generally, we are in a good agreement with all previous results.

5.3 Anisotropy of Young modulus

Investigation the anisotropy of Young modulus is the first step in the study of tensile anisotropy. A high value of Y often correlates with a high value of ideal strength, but also with a higher brittleness of the material. Generally, the value of Y for a given direction determines the initial slope of the stress-strain curves for small tensile deformation. The anisotropic behaviour of Young modulus can be calculated using the general transformation rule for 4th-rank tensors (Sec.4). We have calculated it for specific paths linking high symmetry directions, as sketched on Fig. 6. Due to high symmetry of the cubic lattice ($L1_2$ and $A1$) a very short path is sufficient for a full characterisation of the anisotropy ($[100] \rightarrow [110] \rightarrow [111] \rightarrow [100]$); for the tetragonal $D0_{22}$ structure it is necessary to link a further path ($[100] \rightarrow [101] \rightarrow [001] \rightarrow [111] \rightarrow [101]$).

5.3.1 $L1_2$ structures. The anisotropic behaviour of Young modulus for $L1_2$ crystal structures is presented in Fig. 7(left). The effect of the saturation of inter-atomic bonds by addition of d electrons can be seen in the variation of curves. We shall refer to the difference between the maximal and the minimal value of Y as the level of anisotropy Δ (LOA). Fig. 7(right) shows a histogram of Y evaluated for the irreducible part of the cell. The experimentally stable Al₃Sc compound exhibits very low variation with $\Delta = 16.4$ GPa. The next compound from the series, Al₃Ti with two d electrons more per elementary cell, does not change this situation substantially. The anisotropy behaviour is similarly weak with a stronger decline of Y in the $\langle 100 \rangle$ directions ($\Delta = 21.7$ GPa). This weak dependence on the saturation of bonds is broken for Al₃V compound, where the LOA is really high ($\Delta = 90.1$ GPa). The reason for this increased anisotropy is the increase and decrease of Young modulus in the $\langle 111 \rangle$ and $\langle 100 \rangle$ directions, respectively. Further band filling in Al₃Cr, does not lead to a further increase of LOA, but to a return to the weak response regime similar to Al₃(Sc,Ti), with $\Delta = 19.5$ GPa.

The pronounced variation of the anisotropy of Y can be explained by a reconfiguration of bonds with increasing d -band filling. Generally bonding in these alloys has a metallic and a covalent component — the tendency to form covalent bonds depends on the crystal structure and the d -band filling, as discussed in the preceding section. The relative importance of metallic and covalent bonding is reflected in the difference electron density, i.e. the total self-consistent electron density minus a linear superposition of the atomic electron densities. Covalent bonding leads to an accumulation of electrons halfway between the interacting atoms, i.e. to the formation of bond charges. Fig. 8 shows the iso-surfaces of the difference charge density at the $27 \times 10^{-3} \text{ e}/\text{\AA}^3$ level in the elementary cell of all compounds¹.

For Al₃Sc [Fig. 8(a)] and Al₃Ti [Fig. 8(b)] the difference electron density is rather de-localised (indicating a substantial metallic component of the bonding), with maxima along the body diagonals of the unit cell and between Al atoms in plane B. The former arise from the occupation of bonding states between the d^3 hybrids on the TM atoms and Al- sp hybrid orbitals (see Fig. 3) and reflect the covalent bonding between atoms in planes C, D, and E. The latter arise from the bonding overlap of Al- sp^2d hybrids [14]. The fact that the distribution of the difference electron density is always isotropic explains the weak anisotropy of Young modulus. The change from Al₃Sc to Al₃Ti easily modest — the difference electron density increases along the $\langle 111 \rangle$ diagonal and is reduced in the Al-Al bonds, reflecting a slight increase of the inter-planar -C-D-E- bonds at the expense of in-planar Al-Al bonds in plane B.

Fig. 8(c) shows the iso-surface of difference charge density for Al₃V at the same level. The enhanced bonding charge in the -CDE- inter-planar region comes from the high population of d^3 hybrids (see PDOS

¹We choose the $27 \times 10^{-3} \text{ e}/\text{\AA}^3$ value due to the best viewing of the bonding charge in the Al₃V compound. At this level the covalent contribution to the Al-V bonds can be seen easily.

on Fig. 3) oriented along $\langle 111 \rangle$. In addition, an increased occupation of sd^2 hybrids rapidly (predominantly due to a d_{xy} atomic orbital contribution) leads to an enhanced charge density roughly in the middle between V–Al atoms in plane A on Fig. 8(c). This indicates covalent bonding, as confirmed by the COOP analysis and identified as bonding $V(d_{xy})$ – $Al(sp^2d)$ hybrid orbitals in plane A [14]. Since the $L1_2$ crystal structure can be seen as an –CDE– stacking of close-packed hexagonal C, D, and E planes along the $\langle 111 \rangle$ direction, the covalent in-planar bonds between V–Al atoms in plane A can be seen as inter-planar bonds between the C–D and D–E planes. It is obvious that this bonding is relatively strong, since it is moderated by 6 directional covalent bonds between one vanadium atom in plane D and 6 aluminium atoms in planes C and E, see Fig.2(left). This type of bonding is typical for all aluminium rich vanadium compounds and able to form strong wide-extended –Al–V– chains of covalent bonds (e.g. tetrahedral network in $Al_{10}V$, ref. [22]). These strong bonds promote the high resistance of the Al_3V compound against all tensile deformations where the distance between –CDE– planes increases and results in the high value of Y along $\langle 111 \rangle$. On the other hand, the density maxima representing Al–Al bonds in the B planes roughly between A and B planes (cf. Fig. 1) have disappeared. This leads to a low resistance against an increasing A–B inter-planar distance and hence a low value of Y along $\langle 100 \rangle$. Hence the anisotropy of the Young modulus results from a reconfiguration of partially covalent inter-planar bonds due to the increased d -band filling.

The bonding situation for ferromagnetic Al_3Cr is presented in Fig. 8(d). The PDOS on Fig. 3 indicates a high saturation of both hybrid groups (d^3 and sd^2), however, in comparison with Al_3V , no enhanced bonding charge leading to covalent Cr–Al bonds can be noticed in plane A. The difference electron density has maxima in the tetrahedral holes of the $L1_2$ structure, the vertices of each tetrahedron are occupied by 3 Al and one Cr atom. Such a difference electron density indicates a multi-centre — i.e. predominantly metallic bond — and thus is compatible with a very low anisotropy of Young modulus.

It is interesting to perform a similar analysis for Al (fcc) and Ni_3Al ($L1_2$). The anisotropy curves of Y and the iso-surfaces of the difference charge density are presented in Figs. 7 and 8(e,f), respectively. Aluminium reacts almost isotropically to uniaxial tension ($\Delta = 2.2$ GPa). The difference electron densities are very similar in Al and Al_3Cr — in these cases the low anisotropy of Y is a consequence of predominantly metallic bonding. On the other hand, the low anisotropy of $Al_3(Sc,Ti)$ results from the interplay of two different types of partially covalent –Al–TM– bonding along $\langle 111 \rangle$ and Al–Al along $\langle 110 \rangle$ promoting again a similar resistance against tensile deformations in all directions. The high anisotropy of Al_3V is comparable to Ni_3Al compound ($\Delta = 180.8$ GPa). The anisotropy of the Ni_3Al single crystals has been confirmed also experimentally by nano-indentation measurements [57]. The difference electron density of Ni_3Al shows a pattern similar to that of Al_3V , with an even more pronounced charge accumulation.

5.3.2 $D0_{22}$ structures. The anisotropy of Young modulus for all $D0_{22}$ phases is presented on Fig. 9. All of them present a relatively high level of anisotropy [$\Delta = 60.7, 97.9, 71.7, 114.3$, and 79.7 GPa for $Al_3(Sc,Ti,V,Cr^{fm},Cr^{afm})$, respectively]. Generally, the gradual filling of the d -band results in a shift to higher values with only a slight impact on the shape. These small changes of shape can be associated with the creation/destruction of bonds during saturation, similar to the $L1_2$ structures. We try to explain this anisotropy on the basis of the results for the $L1_2$ structures, since the $D0_{22}$ structure may be considered as consisting of two $L1_2$ cubes stacked along the z direction, with a $[\frac{1}{2}, \frac{1}{2}, 0]$ anti-phase shift between these cubes [44].

A central TM atom in the A' plane is surrounded by twelve Al atoms in slightly deformed cuboctahedron. Thus can be directly compared to a surroundings of TM atom in the $L1_2$ structure. Figs. 10(a,b,c) present in the right panels the iso-surfaces of the difference charge density in the elementary cells of $Al_3(Sc,Ti,V)$ at 27×10^{-3} e/ \AA^3 . For comparison, on the left side, we present the difference charge density for two $L1_2$ cubes stacked along the z direction with the TM atom shifted to the central position, similar as in the $D0_{22}$ structure. As can be seen, in the series $Al_3Sc \rightarrow Al_3V$, the noticeable difference in the distribution of bonding charge inside the virtual cuboctahedron gradually vanishes. For Al_3V , these two bonding objects are almost equal. Although in the other compounds the difference is more pronounced, one common feature can be noticed in all of them. The concentration of charge in inter-planar –CDE– region of the $L1_2$ structures due to the saturation of d^3 hybrids (d_{xz}, d_{yz}, d_{z^2}) exists also in $D0_{22}$ structure.

The d^4 hybridisation (d_{xz} , d_{yz} , d_{z^2} , $d_{x^2-y^2}$) was identified as a dominant bonding mechanism in the $D0_{22}$ structures, however its major part consists of atomic orbitals active in d^3 hybridisation¹. It can be shown that the occupancy of $d_{x^2-y^2}$ and in particular d_{xy} atomic orbital is substantially higher in $D0_{22}$ structures in comparison to $L1_2$ structures. This corresponds to the formation of $-BA'B-$ inter-atomic bonds at a lower degree of band-filling, due to well saturated d^4 hybrids.

The maximal value of Y along $\langle 110 \rangle$ (the hard direction) can be explained by a superposition of two hard directions — $\langle 112 \rangle$ and $\langle 110 \rangle$ — active in $D0_{22}$ structure. The first one is connected with the concentration of bonding charge in the inter-planar region along the $[111]$ direction of $L1_2$ structures due to the occupation of d^3 hybrids. This direction coincides in the $D0_{22}$ structure with the $\langle 112 \rangle$ direction. The second and dominant contribution comes from the saturation of d_{xy} atomic orbitals and creation of TM–Al₂ bonds in A and A' planes. Moreover, the hard direction is supported also by newly created Al₂–Al₂ bonds in plane B and partially by inter-planar $-B-A'-B-$ bonds. The easy $\langle 100 \rangle$ direction is a consequence of the charge movement into $\langle 110 \rangle$ direction. We note that the value of Y in $[001]$ (along inter-planar $-B-A'-B-$ bonds) scales well with the strength of bonds.

The Y anisotropy of Al₃Cr (Fig. 9) is reduced in comparison to Al₃V. This occupation of anti-bonding states is not so surprising, since the weak bonding due to the over-saturation of bonds and magnetic effects have been observed in the $L1_2$ structure before. Figs. 10(d,e) show the difference charge distribution in the ferromagnetic and anti-ferromagnetic states. Both situations are almost identical, except for the missing contribution of TM–Al₂ bonds in A and A' planes in the anti-ferromagnetic state. It seems that the occupation of d_{xy} atomic orbitals (responsible for in-planar covalent bond formation in planes A and A') is too low to provide sufficient bonding strength in the $\langle 110 \rangle$ direction (where these in-planar bonds act), see Fig. 9.

Although the basic mechanism behind the anisotropy of the $D0_{22}$ structures is well understood, one important thing has to be noticed. The comparison of the distribution of the difference charge density in the $D0_{22}$ structure (right) and in two stacked $L1_2$ cubes (left) [Figs. 10(a,b,c)] reveals that the $L1_2 \rightleftharpoons D0_{22}$ transformation induces substantial changes of bonding only for Al₃(Sc,Ti) compounds. Moreover, if we take the anisotropy level of the Young modulus (LOA) into account, the $D0_{22} \rightarrow L1_2$ transformation (high \rightarrow low anisotropy) is important only for these two compounds. The transformation of Al₃V into the $L1_2$ structure changes the bonding and anisotropy of this alloy in no way. Therefore, if we take the low Y anisotropy of pure Al (fcc) as a property of required good ductility, the transformation of trialuminides from $D0_{22} \rightarrow L1_2$ by addition of ternary elements can be achieved only for Al₃(Sc,Ti), where the LOA changes from 60.7 to 16.4 GPa and from 97.9 to 21.7 GPa. The transformation of Al₃Ti leads to the highest bonding change (the central bond charge is completely destroyed), hence a substantial change of mechanical properties can be expected. The structural transformation of Al₃V will even increase the LOA from 60.7 to 90.1 GPa.

5.4 Anisotropy of the Poisson ratio

For uniaxial tensile deformation, the Poisson ratio ν defined as the negative ratio between lateral and longitudinal strains, can be obtained directly from the elastic constants. Since it is connected to the change of structure in the perpendicular to the applied tension direction, its value can reveal how the crystal reacts on loading or which deformation path it will adopt. The Poisson ratio is associated with the volume change during uniaxial tensile deformation. A high value (close to 0.5) indicates almost no volume change. The volume increase due to expansion in one direction is cancelled by lateral shrinking. In this case, the structure easily deforms in both directions, as expected for weak inter-atomic bonding. A low ν value indicates a large volume change, caused by high resistance of the structure against lateral deformation. In general, a such behaviour will be observed in the presence of strong bonds in lateral directions.

¹The irreducible representation for d^4 hybridisation is $\Gamma^{\text{hyb}} = A_{1g} \oplus E_g \oplus B_{1g}$. It can be decomposed into $A_{1g} \oplus E_g$ and B_{1g} , i.e. d^3 hybrids of d_{xz} , d_{yz} , d_{z^2} atomic orbitals and a separate contribution of $d_{x^2-y^2}$ atomic orbital.

5.4.1 $L1_2$ structures. The anisotropy of the Poisson ratio for $L1_2$ crystal structures under uniaxial tension in [001], [110], and [111] directions is presented in Figs. 11(a,b,c). As can be seen, [001] tension [Fig. 11(a)], will lead to deformation with small volume change. The structures will shrink equally in all lateral directions, conserving the square lattice of A and B planes (as expected for a tetragonal deformation). Al_3V has the highest value of ν , indicating the lowest resistance against lateral contraction, since there are no strong inter-planar bonds in $\langle 100 \rangle$ directions. The series $\text{Al}_3\text{V} \rightarrow \text{Al}_3\text{Sc}$ lead to an increase of bond charge in this direction and consequently the value of ν decreases. An interesting behaviour can be noticed for [110] tension [Fig. 11(b)]. Tension along $\langle 110 \rangle$ induces an orthorhombic deformation path with strongly differing lateral deformations in the $[\bar{1}10]$ and $[001]$ directions. We note that along the $[\bar{1}10]$ direction TM-Al bonds (first neighbours) alternate, while along the $[001]$ direction we have rows of second-neighbour TM-TM bonds. We have already discussed the gradual saturation of TM-Al bonds with increasing band-filling: Al-V bonds are substantially stronger than Al-Sc bonds. This explains the strong variation of $\nu[\bar{1}10]$ in the $\text{Al}_3\text{Sc} \rightarrow \text{Al}_3\text{V}$ series. As can be seen, the strength of Al-V bonds leads to almost zero lateral deformation along $\langle 110 \rangle$ ($\nu = 0.014$). The situation for the $[001]$ direction is just the reverse. The outflow of bonding charge from the space along the $[001]$ direction in the $\text{Al}_3\text{V} \rightarrow \text{Al}_3\text{Sc}$ series (due to the formation of covalent bonds, see Sec. 5.3.1) leads to the highest value of $\nu[001]$ for Al_3V , since no inter-planar ABAB bonds exist here. The situation for [111] tension is similar to tension in the $[001]$ direction. A tetragonal deformation path is adopted with equal deformations in all lateral directions according to strength of bonds.

5.4.2 $D0_{22}$ structures. The anisotropy of Poisson ratio for $D0_{22}$ -type compounds for uniaxial tension in [001], [100], [110], [101], and [111] directions is presented on Fig. 12. A tetragonal deformation path is adopted only for [001] tension, otherwise a strong orthorhombic deformation takes a place. We notice some common features in the anisotropy of ν . The presence an Al-TM alternation of atoms in some lateral directions is associated with a substantial decrease of ν (a hard direction). Otherwise, TM-TM alternation leads generally to higher values of ν (easy direction). For example, the strength of strong covalent BA'B inter-planar bonds leads [see Fig. 12(b)] to a high resistance against deformation in the lateral [001] direction in comparison to [010]. However, under [110] tension [Fig. 12(c)], this resistance is low in the hard $[\bar{1}10]$ direction ($\nu \sim \text{zero}$). A high anisotropy of the Poisson ratio for [101] and [111] tensions [Figs. 12(d,e)] arises also from an alternation of atoms in the lateral directions and can be understood in terms of the presence or absence of covalently bonded Al-TM chains.

6 Conclusion

We have presented an investigation of the tensile anisotropy of the trialuminides of the first four early 3d transition-metal elements in the elastic limit. The intermetallic compounds $\text{Al}_3(\text{Sc,Ti,V,Cr})$ have been investigated using *ab-initio* density-functional calculations in both the $L1_2$ and $D0_{22}$ crystal structures. This study is motivated by the desire to understand the intrinsic mechanisms causing the brittleness of these compounds. In previous work [14, 15, 22] we have proved the existence of strong directional metallo-covalent bonds in aluminium-rich compounds. When one is interested in good mechanical properties, a certain degree of covalency is desired, since it increases bond strength and consequently leads to higher mechanical strength and hardness. However, it leads also to an undesired high brittleness. The series $\text{Al}_3(\text{Sc,Ti,V,Cr})$ alloys to study the gradual formation of covalent bonds with increasing *d*-band filling is leading to substantial changes in the mechanical properties.

For a better understanding of covalent bond formation, chemical bonding in both crystal structures has been re-investigated and presented in some new way (but fully compatible with our previous work [14, 15]). Of central importance is regular (for $L1_2$) or slightly deformed (for $D0_{22}$) cuboctahedron (with O_h symmetry) around the TM site formed by 12 aluminium atoms. Such a configuration leads to the formation of sd^5 hybrids promoting the TM-Al bond interaction. The decomposition of this set of hybrid orbitals according to the D_{3d} and D_{4h} subgroups has been found to be very fruitful as it allows to identify two variants of active bonding geometries inside the cuboctahedron. The main bonding character comes

from the saturation of dominant hybrid orbitals located on the TM atoms [d^3 hybrids (d_{xz} , d_{yz} , and d_{z^2}) for the $L1_2$ structure and d^4 hybrids ($d^3 + d_{x^2-y^2}$) for the $D0_{22}$ structure].

In the series $\text{Al}_3\text{Sc} \rightarrow \text{Al}_3\text{Cr}$ these bonding configurations are gradually saturated. In $L1_2$ structures, due to the d^3 hybrids, charge is concentrated in the tetrahedral holes along the $\langle 111 \rangle$ directions and leads to the formation of covalent bonds between closed-packed $\{111\}$ planes which are strongest for the Al_3V compound. This mechanism provides Al_3V ($L1_2$) with a high resistance against all deformations connected with the separation of $\{111\}$ planes. In addition the saturation of sd^2 hybrids (s , d_{xy} , and $d_{x^2-y^2}$) forms in-planar bond in these planes. For $D0_{22}$ structures, the saturation of the d^4 hybrids leads to charge concentration along the $\langle 112 \rangle$ directions and formation of inter-planar bonds between $\{001\}$ planes. Simultaneously, the occupation of sd hybrids (s and d_{xy}) leads to the creation of in-planar bonds. This mechanism provides the Al_3V ($D0_{22}$) compound with a high resistance against all deformations leading to an increase of the separation between the $\{001\}$ planes. Including the Al_3Cr compound in the series $\text{Al}_3(\text{Sc}, \text{Ti}, \text{V})$ shows the limits of the saturation process. All obtained results confirm that Al_3V represents the fully saturated state, and adding more d -electrons (as for Al_3Cr) leads to the occupation of non-bonding and later anti-bonding states. Together with the magnetism of Cr thus leads to a substantial redistribution of charge and to a worsening of the conditions for covalent bond formation. Therefore Al_3Cr (both in ferromagnetic and anti-ferromagnetic configurations) shows weaker mechanical properties.

The formation of strong directional inter-atomic bonds leads to increase of almost all computed elastic constants and to a change of the anisotropy of the Young modulus Y and the Poisson ratio ν . For $L1_2$ structures the effect of the saturation of the covalent bonds can be seen in the variation of Y v. tensile direction curves only and leads to a high anisotropy of Al_3V with a dominant peak for tension along the $\langle 111 \rangle$ direction. This hard direction is associated with the presence of strong covalent bonds between closed-packed $\{111\}$ planes. The high localisation of charge also leads to the presence of an easy direction along $\langle 100 \rangle$. For $D0_{22}$ structures the saturation of the bonds leads only to a shift of Y to higher values with only a slight impact on the shape. The hard direction results from the superposition of two hard directions [$\langle 112 \rangle$ and $\langle 110 \rangle$] as a consequence of the saturation of the bonding d^4 and sd hybrids. A high anisotropy of the Poisson ratio arises from the alternation of atoms in the lateral directions and can be understood in the same terms. A presence of strong Al-TM chains leads to a high resistance against the lateral shrinking during the uniaxial tension.

Our present study of the elastic anisotropy represents only a first step toward an understanding of the origin of the brittleness of most TM trialuminides. The following steps must include an investigation of the tensile behaviour of a large range of strains, up to the maximum stress sustained by the materials, as well as the factors determining the formation and mobility of dislocation. Such studies are under way, results will be reported in due course. The present analysis shows that the structural transformation of $\text{Al}_3(\text{Sc}, \text{Ti})$ from $D0_{22}$ to $L1_2$ leads to a significant reduction of the anisotropy of Young modulus, while Al_3V remains strongly anisotropic even in the cubic $L1_2$ phase. As ductile behaviour requires a small difference between the easy and hard direction of tension, this is a first (but not sufficient) condition for an improved ductility of $L1_2$ -type Al_3Ti (Al_3Sc is already stable in this structure). Furthermore, $L1_2$ -type $\text{Al}_3(\text{Sc}, \text{Ti})$ are predicted to display a very low anisotropy of the Poisson ratio under uniaxial strain — again in contrast to $L1_2$ - Al_3V which shows a very high anisotropy under $[110]$ tension. However, further studies beyond the elastic regime will be required to substantiate a prediction that stabilisation of $L1_2$ -type Al_3Ti will possible lead to a reduced brittleness of this material.

Acknowledgements

Work at the Vienna University has been supported by the VASP project. We acknowledge support also from the Grant Agency for Science in Slovakia (Grant No. 2/5096/25).

References

- [1] Y. V. Milman, D. B. Miracle, S. I. Chugunova, I. V. Voskoboinik, N. P. Korzhova, T. N. Legkaya, and Y. N. Podrezov, *Intermetallics* 9 839 (2001).

- [2] H. A. Calderon, V. Garibay-Febles, M. Umemoto, and M. Yamaguchi, *Mat. Sci. Eng. A* **329-331** 196 (2002).
- [3] K. Venkateswarlu, L. C. Pathak, A. K. Ray, G. Das, P. K. Verma, M. Kumar, and R. N. Ghosh, *Mat. Sci. Eng. A* **383** 374 (2004).
- [4] K. S. Kumar, in *Structural Intermetallics, Microstructure and mechanical properties of ternary L1₂ aluminum-rich intermetallics*, edited by R. Darolia, J. J. Lweandowski, C. T. Liu, and P. L. Martin (TMS Minerals, Metals, and Materials Society, 1993), pp. 87–96.
- [5] P. Villars, *Pearson's Handbook of Crystallographic Data for Intermetallic Phases* (American Society for Metals, Materials Park, OH, 1997).
- [6] R. B. Schwarz, P. B. Desch, S. Srinivasan, and P. Nash, *Nanostruc. Mater.* **1** 37 (1992).
- [7] A. Raman and K. Schubert, *Z. Metallkd.* **56** 99 (1965).
- [8] E. P. George, D. P. Pope, C. L. Fu, and J. H. Schneibel, *ISIJ Int.* **31** 1063 (1991).
- [9] T. Takahashi, K. Tominaga, Y. Tsuchida, S. Motizuki, F. Kawai, and T. Hasegawa, *Mat. Sci. Eng. A* **329-331** 474 (2002).
- [10] M. V. Karpets, Y. V. Milman, O. M. Barabash, N. P. Korzhova, O. N. Senkov, D. B. Miracle, T. N. Legkaya, and I. V. Voskoboinik, *Intermetallics* **11** 241 (2003).
- [11] E. P. George, J. A. Horton, W. D. Porter, and J. H. Schneibel, *J. Mater. Res.* **5** 1639 (1990).
- [12] M. Yamaguchi and H. Inui, in *Intermetallic Compounds, Al₃Ti and its L1₂ variations*, edited by J. Westbrook and R. Fleischer (John Wiley & Sons, New York, 1994), pp. 147–172.
- [13] K. S. Kumar, *Int. Mater. Rev.* **35** 293 (1990).
- [14] M. Krajčí and J. Hafner, *J. Phys.: Condens. Matter* **14** 1865 (2002).
- [15] M. Jahnátek, M. Krajčí, and J. Hafner, *Phys. Rev. B* **71** 024101 (2005).
- [16] J. B. Dunlop, G. Grüner, and A. D. Caplin, *J. Phys. F: Met. Phys.* **4** 2203 (1974).
- [17] C.-S. Lue, S. Chepin, J. Chepin, and J. H. Ross, Jr., *Phys. Rev. B* **57** 7010 (1998).
- [18] T. J. Bastow, C. T. Forwood, M. A. Gibson, and M. E. Smith, *Phys. Rev. B* **58** 2988 (1998).
- [19] C.-S. Lue and J. H. Ross, Jr., *Phys. Rev. B* **60** 8533 (1999).
- [20] A. D. Caplin, G. Grner, and J. B. Dunlop, *Phys. Rev. Lett.* **30** 1138 (1973).
- [21] R. Hoffmann, *Solids and Surfaces: A Chemist's View of Bonding in Extended Structures* (VCH, New York, 1988).
- [22] M. Jahnátek, M. Krajčí, and J. Hafner, *J. Phys.: Condens. Matter* **15** 5675 (2003).
- [23] R. von Mises, *Z. Angew. Math. Mech.* **8** 161 (1928).
- [24] M. H. Yoo and C. L. Fu, *ISIJ Int.* **31** 1049 (1991).
- [25] S. H. Wang and P. W. Kao, *Acta Mater.* **46** 2675 (1998).
- [26] S. H. Wang, P. W. Kao, and C. Chang, *Scripta Mater.* **40** 289 (1999).
- [27] W. Voigt, *Lerhbuch der Kristallphysik* (Teubner-Verlag, Leipzig, 1928).
- [28] A. Reuss, *Z. Angew. Math. Mech.* **9** 49 (1929).
- [29] R. Hill, *Proc. Phys. Soc. Lond.* **A65** 349 (1952).
- [30] S. C. Cowin and G. Yang, *J. Elasticity* **46** 151 (1997).
- [31] M. Moakher, *J. Elasticity* **82** 273 (2006).
- [32] G. Kresse and J. Furthmüller, *Comput. Mat. Sci.* **6** 15 (1996).
- [33] G. Kresse and J. Furthmüller, *Phys. Rev. B* **54** 11169 (1996).
- [34] P. Blöchl, *Phys. Rev. B* **50** 17953 (1994).
- [35] G. Kresse and D. Joubert, *Phys. Rev. B* **59** 1758 (1999).
- [36] J. P. Perdew, J. A. Chevary, S. H. Vosko, K. A. Jackson, M. R. Pederson, D. J. Singh, and C. Fiolhais, *Phys. Rev. B* **46** 6671 (1992).
- [37] H. J. Monkhorst and J. D. Pack, *Phys. Rev. B* **13** 5188 (1976).
- [38] P. E. Blöchl, O. Jepsen, and O. K. Andersen, *Phys. Rev. B* **49** 16223 (1994).
- [39] S. H. Vosko, L. Wilk, and M. Nusair, *Can. J. Phys.* **58** 1200 (1980).
- [40] Y. Le Page and P. Saxe, *Phys. Rev. B* **63** 174103 (2001).
- [41] G. Bester and M. Fahnle, *J. Phys.: Condens. Matter* **13** 11551 (2001).
- [42] C. L. Condon, G. J. Miller, J. D. Strand, S. L. Budko, and P. C. Canfield, *Inorg. Chem.* **42** 8371 (2003).
- [43] G. G. Hall and D. Rees, *Int. J. Quantum Chem.* **63** 197 (1997).
- [44] C. Amador, J. J. Hoyt, B. C. Chakoumakos, and D. de Fontaine, *Phys. Rev. Lett.* **74** 4955 (1995).
- [45] J. Turley and G. Sines, *J. Appl. Phys.* **41** 3722 (1970).
- [46] J. Turley and G. Sines, *J. Phys. D: Appl. Phys.* **4** 264 (1971).
- [47] J. F. Nye, *Physical Properties of Crystals: Their Representation by Tensors and Matrices* (Oxford University Press Inc., New York, 1985).
- [48] A. Cazzani and M. Rovati, *Int. J. Solids. Struct.* **40** 1713 (2003).
- [49] A. Cazzani and M. Rovati, *Int. J. Solids. Struct.* **42** 5057 (2005).
- [50] M. Rovati, *Scripta Mater.* **48** 235 (2003).
- [51] P. M. Sutton, *Phys. Rev.* **91** 816 (1953).
- [52] G. Simmons and H. Wang (Editors), *Single Crystal Elastic Constants and Calculated Elastic Properties: A Handbook* (M.I.T., Cambridge, MA, 1971).
- [53] M. Nakamura and K. Kimura, *J. Mater. Sci.* **26** 2208 (1991).
- [54] R. Sot and K. J. Kurzydłowski, *Materials Science-Poland* **23** 587 (2005).
- [55] C. L. Fu, *J. Mater. Res.* **5** 971 (1990).
- [56] D. Farkas, *Modelling Simul. Mater. Sci. Eng.* **2** 975 (1994).
- [57] W. Wang and K. Lu, *J. Mater. Res.* **17** 2314 (2002).

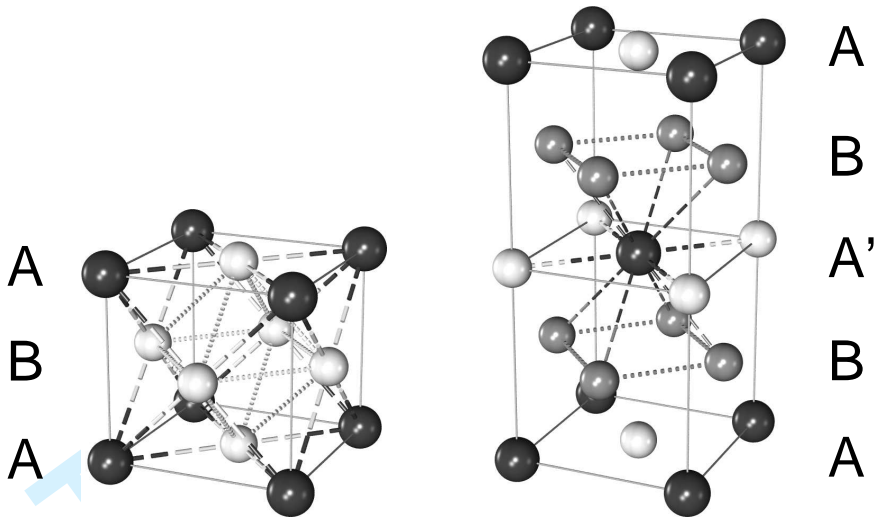


Figure 1. An elementary cell of Al_3V in $L1_2$ (left) and $D0_{22}$ (right) crystal structure. Positions of aluminium atoms are represented by white (Al_1 for $D0_{22}$ and Al for $L1_2$) and gray (Al_2) spheres; positions of vanadium atoms are represented by black spheres. Three types of covalent bonds are sketched: $\text{V}-\text{Al}_2$ ($D0_{22}$) and $\text{Al}-\text{V}$ ($L1_2$) are marked as dashed lines, $\text{V}-\text{Al}_1$ ($D0_{22}$) bonds are displayed as dash-dotted lines, Al_2-Al_2 ($D0_{22}$) and $\text{Al}-\text{Al}$ ($L1_2$) bonds are marked by dotted line segments.

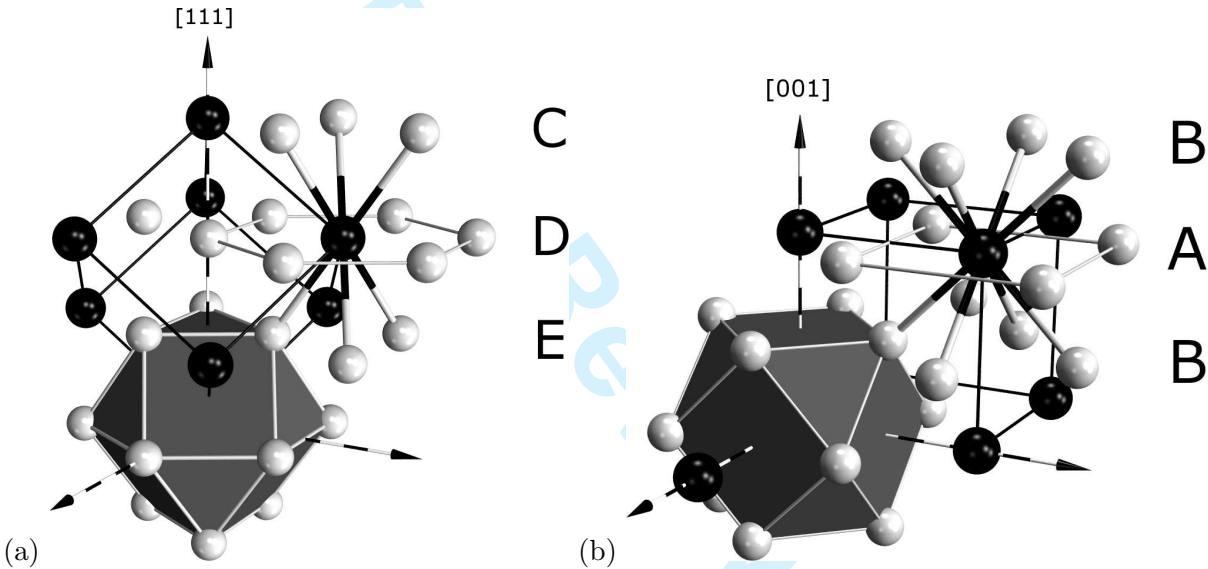


Figure 2. Each TM atom in the $L1_2$ crystal structure is surrounded by 12 equivalent aluminium nearest neighbours forming a regular cuboctahedron with full O_h symmetry; leading to sd^5 hybridisation on TM-site. However, it can be cleared by decomposition into two correlating groups (D_{3d} and D_{4h}) acting along two different rotational axes (three-fold and four-fold) of cuboctahedron. (a) Decomposition according to D_{3d} symmetry group along three-fold axis (C_3) coinciding with the $[111]$ direction of cubic $L1_2$. In this direction the $L1_2$ structure can be viewed as an $-CDE-$ stacking of hexagonal C, D, and E planes. In this way, the sd^5 hybrids can be decomposed into d^3 and sd^2 hybrids acting along the rotational axis and in the perpendicular plane, respectively. (b) Decomposition according to D_{4h} symmetry group along a four-fold axis (C_4) coinciding with the $[001]$ direction of cubic $L1_2$. In this direction the $L1_2$ structure can be viewed as an $-ABAB-$ stacking of square A and B planes. The sd^5 hybrids can be decomposed into d^4 and sd hybrids acting along the rotational axis and in the perpendicular plane, respectively.

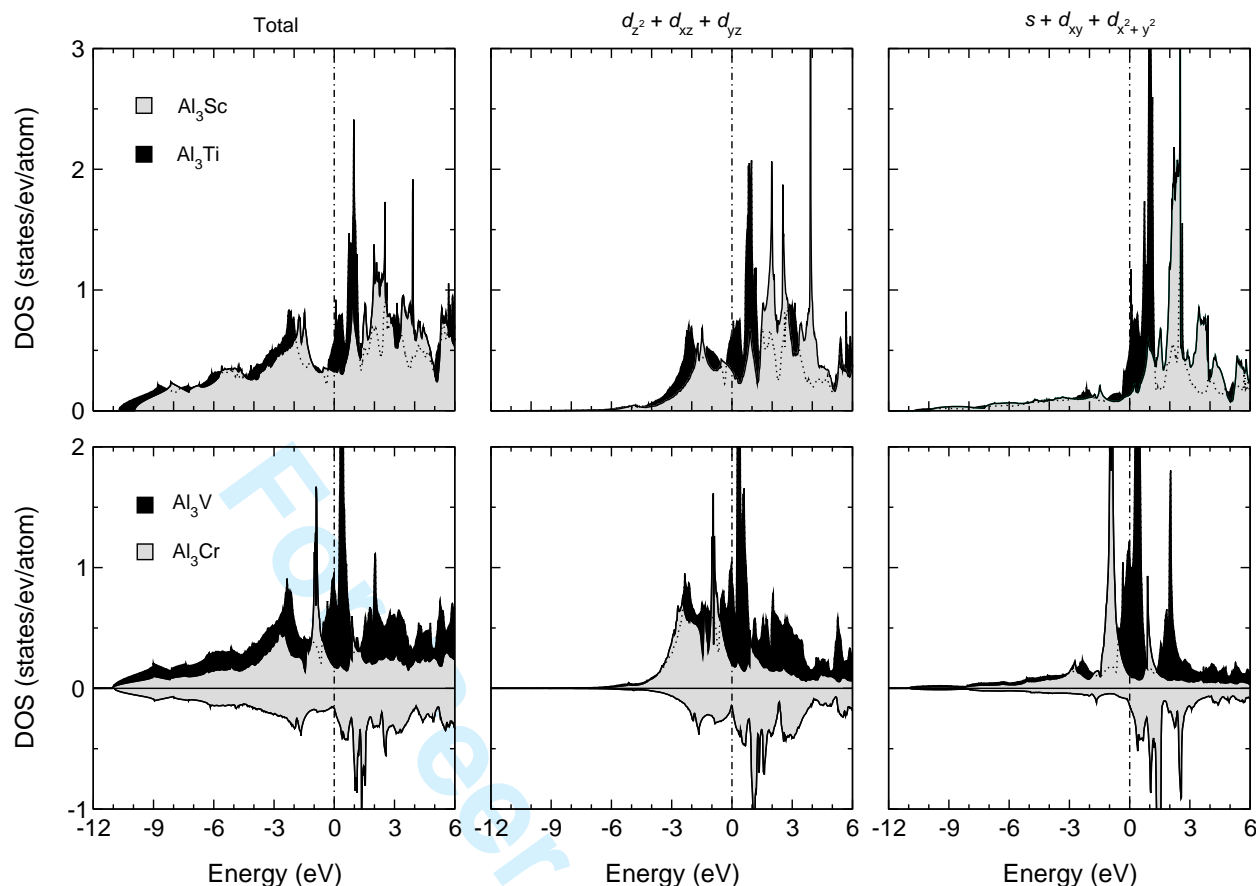


Figure 3. Total (left) and partial (centre and right) density of states (DOS and PDOS) of $\text{Al}_3(\text{Sc}, \text{Ti}, \text{V}, \text{Cr}^{\text{fm}})$ in the $L1_2$ crystal structure. The Al_3Sc and Al_3Ti portions are presented on the upper panel by gray and black colour, respectively. On the lower panel, the situation for Al_3V and $\text{Al}_3\text{Cr}^{\text{fm}}$ is shown. In case of $\text{Al}_3\text{Cr}^{\text{fm}}$, the spin up and spin down portions of DOS are presented as positive and negative value, respectively. The contributions of d orbitals localised on the TM atom are grouped according to the decomposition of the sd^5 hybrids under D_{3d} symmetry. The d^3 hybrid orbitals comes from the d_{z^2} , d_{yz} , and d_{zx} atomic orbitals; the sd^2 hybrids consist of s , d_{xy} , and $d_{x^2-y^2}$ atomic orbitals. As can be seen, in the series $\text{Al}_3\text{Sc} \rightarrow \text{Al}_3\text{V}$, the d^3 hybrids are well saturated from the start (centre); the position of sd^2 hybrids is gradually developed by addition of d electrons (right). The position of the Fermi energetic level was shifted to zero.

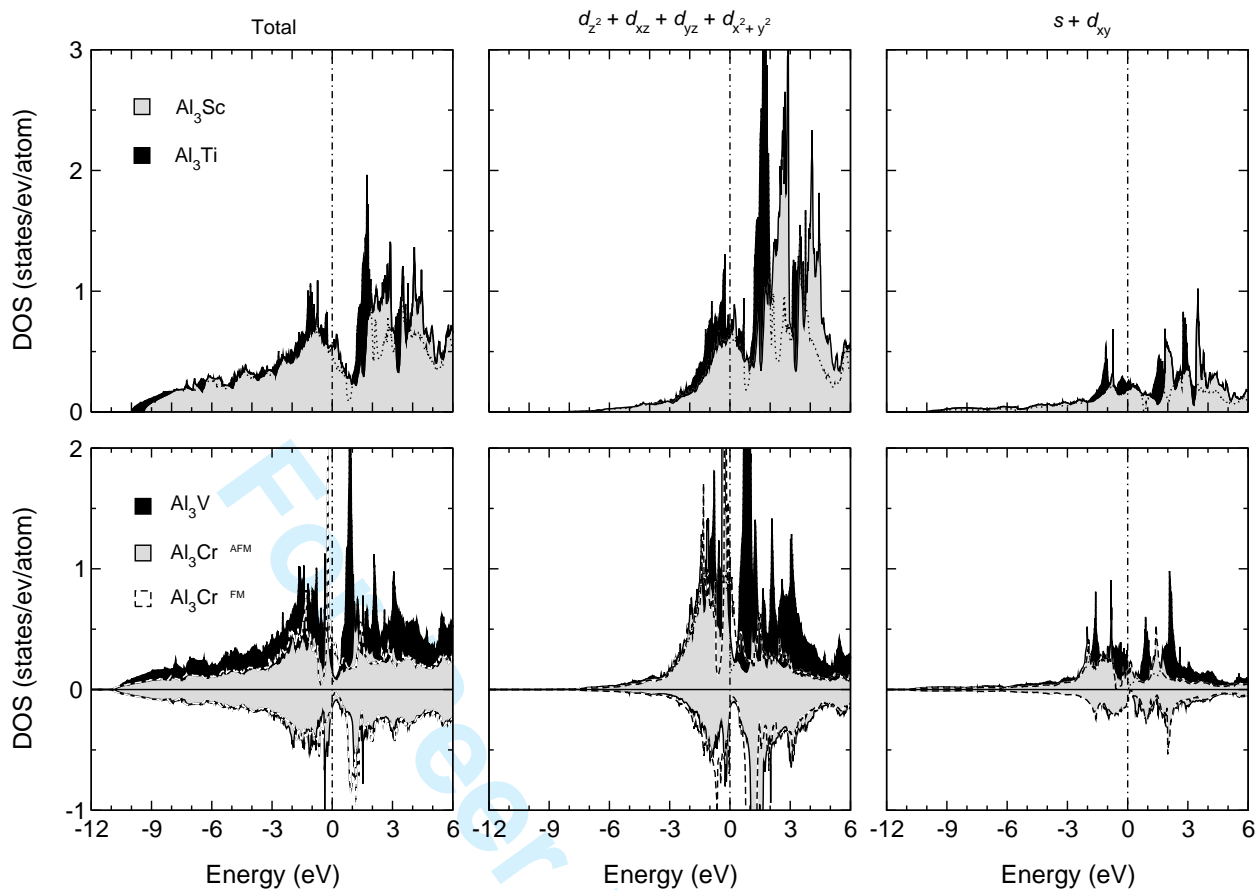


Figure 4. Total (left) and partial (centre and right) density of states (DOS and PDOS) of $\text{Al}_3(\text{Sc}, \text{Ti}, \text{V}, \text{Cr}^{\text{fm}}, \text{Cr}^{\text{afm}})$ in the D_{022} crystal structure. In the upper panel the Al_3Sc and Al_3Ti portions are presented by the gray and black colour, respectively. The lower panel shows the situation for Al_3V , $\text{Al}_3\text{Cr}^{\text{fm}}$, and $\text{Al}_3\text{Cr}^{\text{afm}}$ by gray, black colours, and the dashed line, respectively. The contributions of d orbitals localised on the TM atom are grouped according to the decomposition of the sd^5 hybrids under D_{4h} symmetry. The d^4 hybrid orbitals comes from the d_{z^2} , d_{yz} , d_{zx} , and $d_{x^2-y^2}$ atomic orbitals; the sd hybrids consist of s and d_{xy} atomic orbitals. As can be seen, in the series $\text{Al}_3\text{Sc} \rightarrow \text{Al}_3\text{V}$, the d^4 hybrids (centre) are well saturated from the start; the position of sd hybrids is gradually developed by addition of d electrons (right). We note an unusually deep pseudo-gap formation can be observed very close to the Fermi level. As was shown elsewhere [15] a strong hybridisation between the $\text{Al}(s, p)$ and $\text{V}(d)$ orbitals is responsible for it and associates with the formation of inter-planar $-\text{B}-\text{A}'-\text{B}-$ covalent bonds. The position of the Fermi energetic level was shifted to zero.

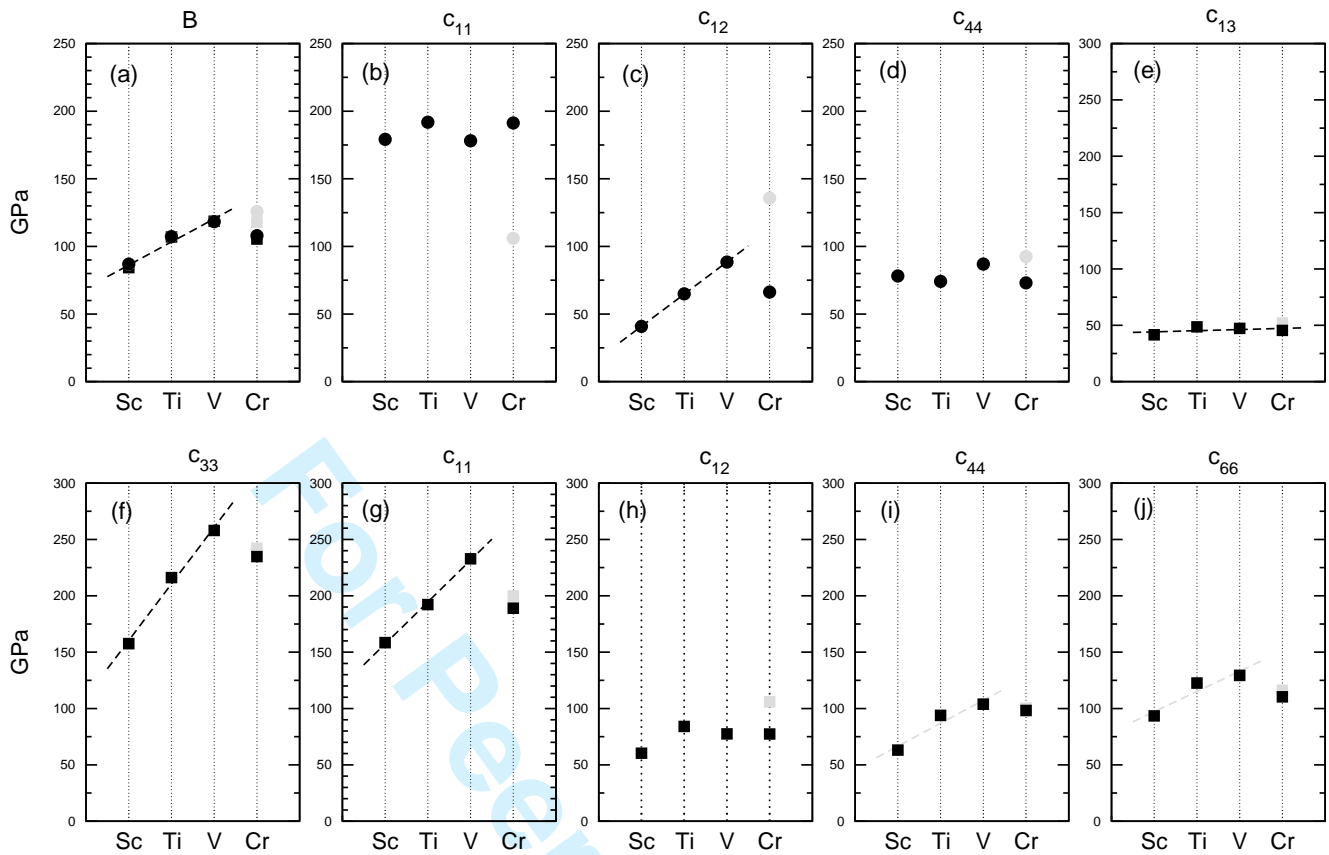


Figure 5. Variation of the computed bulk modulus and elastic constants in the series $\text{Al}_3(\text{Sc,Ti,V,Cr})$ in both the $L1_2$ (circle) and $D0_{22}$ (square) crystal structures. For Al_3Cr ($L1_2$) the black and gray circle refer to the ferromagnetic and non-magnetic states, respectively; for the $D0_{22}$ structure the black and gray square refer to the anti-ferromagnetic and ferromagnetic states, respectively. The panels are ordered as: (a) Bulk modulus (B) for both crystal structures; (b,c, and d) states for c_{11} , c_{12} , and c_{44} elastic constant for $L1_2$ structures; (e,f,g,h,i, and j) states for c_{13} , c_{33} , c_{11} , c_{12} , c_{44} , and c_{66} for $D0_{22}$ structures.

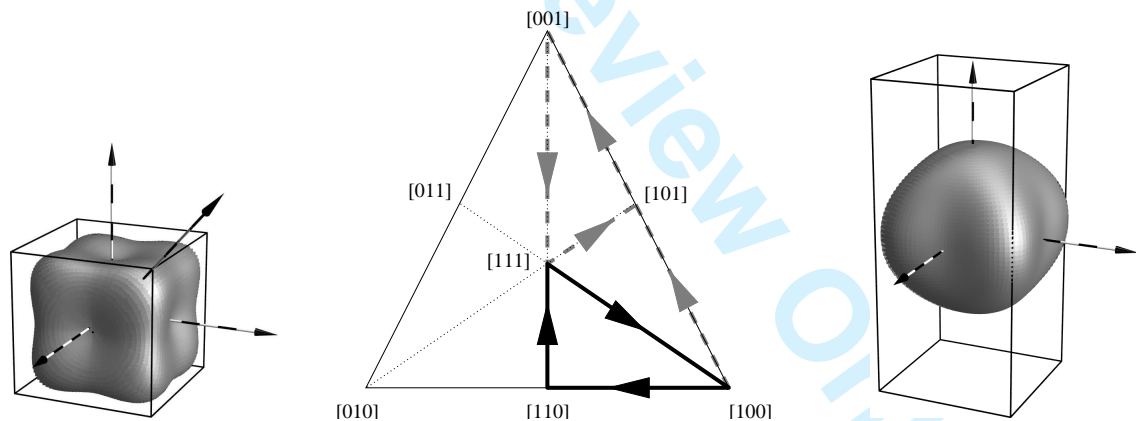


Figure 6. Definition of the paths along which Young modulus is plotted in Fig. 7 and 9. On the left, the $Y(r, \phi, \theta)$ spatial function of Al_3V in $L1_2$ crystal structure is presented. The high symmetry of cubic lattice allows very short un-reproducible path for the full characterisation of anisotropy ($[100] \rightarrow [110] \rightarrow [111] \rightarrow [100]$). It is sketched by black solid line in the middle part of the figure. On the right, the $Y(r, \phi, \theta)$ spatial function of Al_3V in $D0_{22}$ crystal structure is presented. For full characterisation of anisotropy, it is necessary to link a next path ($[100] \rightarrow [101] \rightarrow [001] \rightarrow [111] \rightarrow [101]$); sketched by gray dashed line.

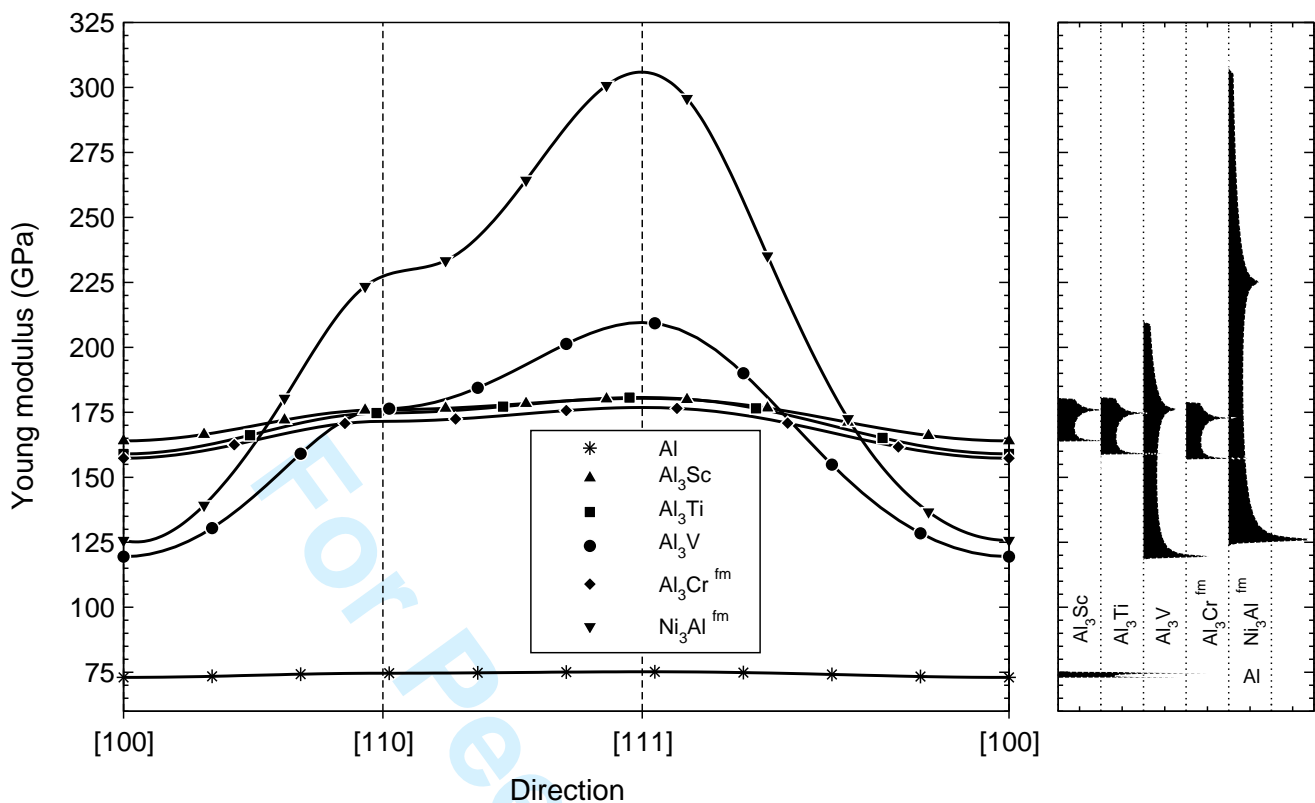


Figure 7. The anisotropy of Young modulus for $\text{Al}_3(\text{Sc}, \text{Ti}, \text{V}, \text{Cr}^{\text{fm}})$ compounds in the L_{12} crystal structure along symmetry directions. For comparison Y for two ductile materials, pure Al (fcc) and Ni_3Al (L_{12}), is also presented. On the right side, the histogram of Young modulus is presented. Its dispersion we refer as a level of anisotropy (LOA). The highest peaks correspond to values of Y which can be measure with the high possibility on the polycrystalline samples. The experimental values of Y for $\text{Al}_{61}\text{Cr}_{12}\text{Ti}_{27}$ and $\text{Al}_{66}\text{Mn}_{11}\text{Ti}_{23}$ phases (an transformed Al_3Ti compound from the $D0_{22}$ to L_{12} structure by addition of ternary element) obtained by Milman *et al.* [1], i.e. 178 and 168 GPa, respectively, reasonably fit into value range for Al_3Ti .

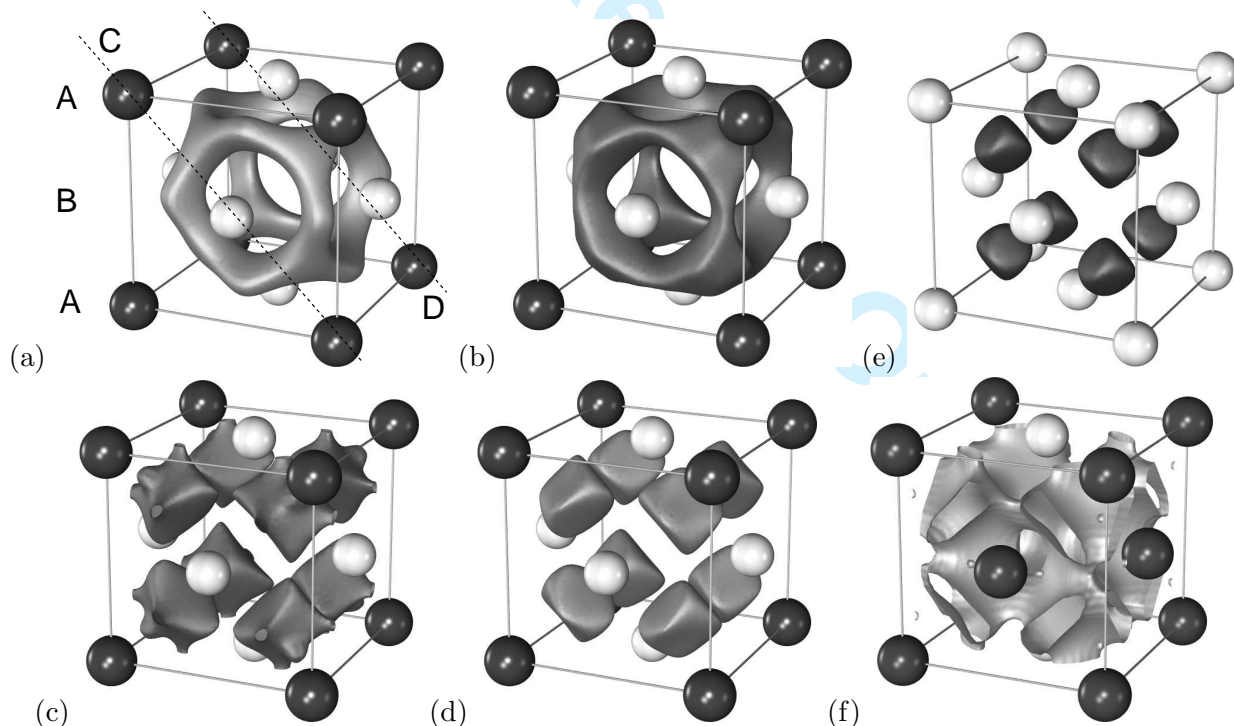


Figure 8. The iso-surfaces of the difference charge density at $27 \times 10^{-3} \text{ e}/\text{\AA}^3$ level in the elementary cells of L_{12} structures [(a) Al_3Sc , (b) Al_3Ti , (c) Al_3V , (d) $\text{Al}_3\text{Cr}(\text{fm})$]. For comparison, the Al (fcc) [e] and Ni_3Al (L_{12}) [f] are also presented.

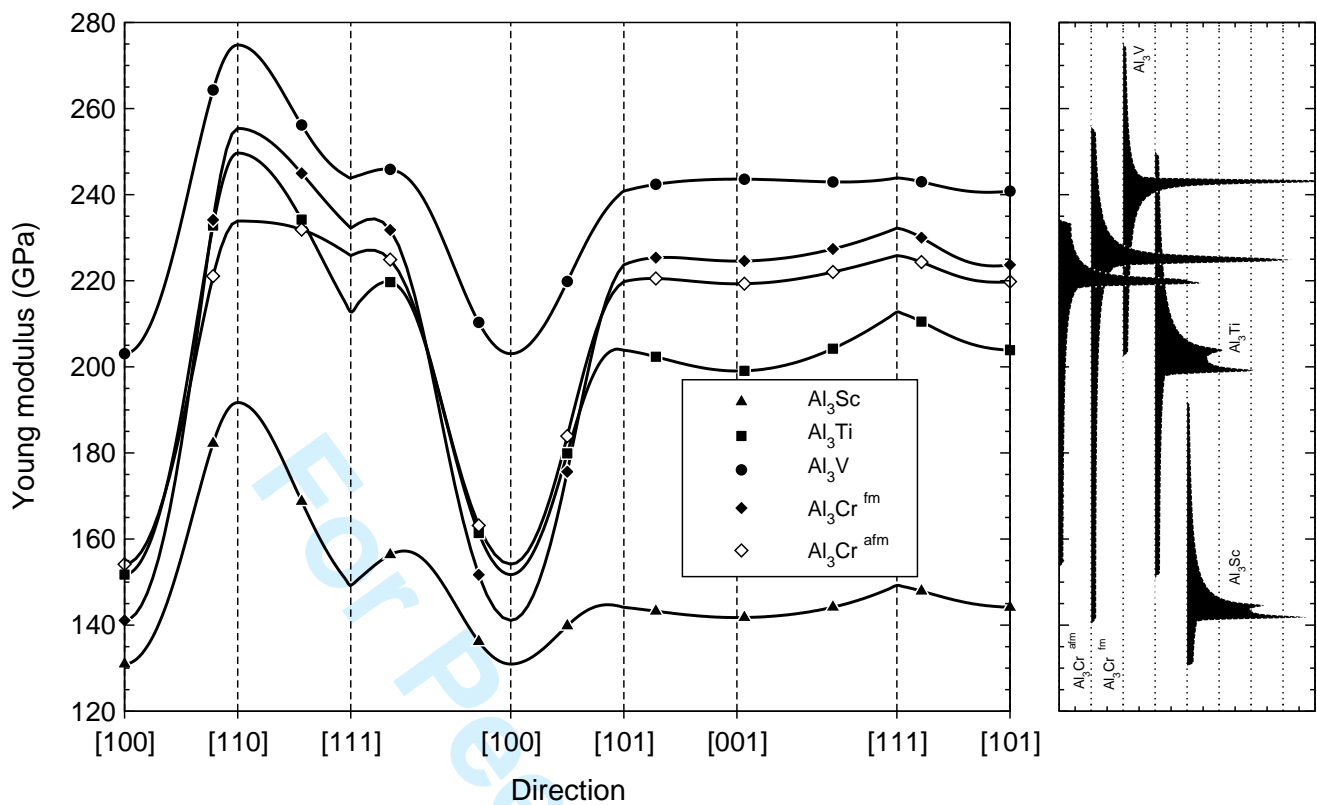


Figure 9. The anisotropy of the Young modulus for $\text{Al}_3(\text{Sc}, \text{Ti}, \text{V}, \text{Cr})$ compounds in the DO_{22} crystal structure. On the right side, the "density of states" for Young modulus is presented. The dispersion of the Y (an analogy to the band width) we called as a level of anisotropy (LOA). The most representative values (the highest peaks) correspond to the most experimentally observable values of polycrystalline samples. The experimental value of Y for Al_3Ti compound (156 GPa) obtained by Milman *et al.* [1] in bending tests is very close to the value of Y in the $\langle 100 \rangle$ direction, indicating the orientation of the "testing" grain during the indentation.

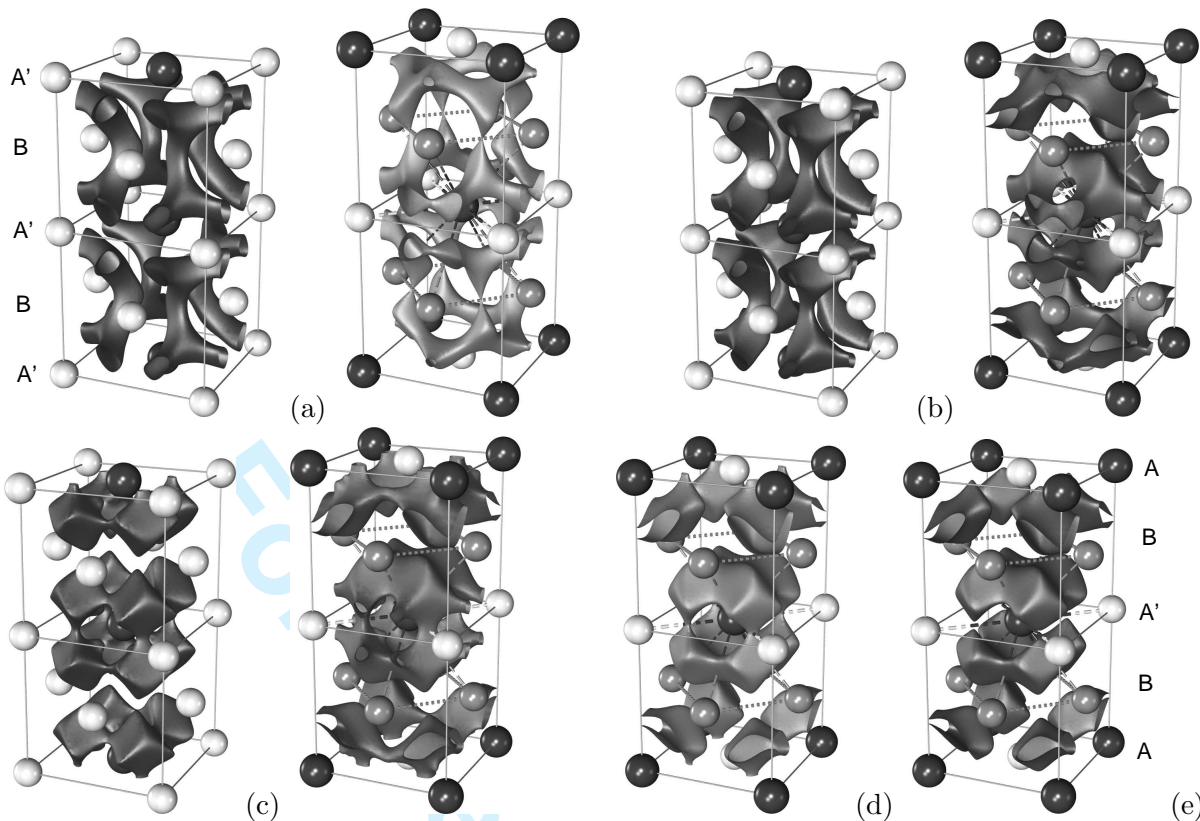


Figure 10. The iso-surfaces of the difference charge density at $27 \times 10^{-3} \text{ e}/\text{\AA}^3$ level in two $L1_2$ cubic structures stacked along z direction (left) and the elementary cell of $D0_{22}$ structure (right). The (a) figures represents the situation for Al_3Sc , (b) for Al_3Ti , and (c) for Al_3V . Figures (d) and (e) corresponds to Al_3Cr in the ferromagnetic and the anti-ferromagnetic state, respectively.

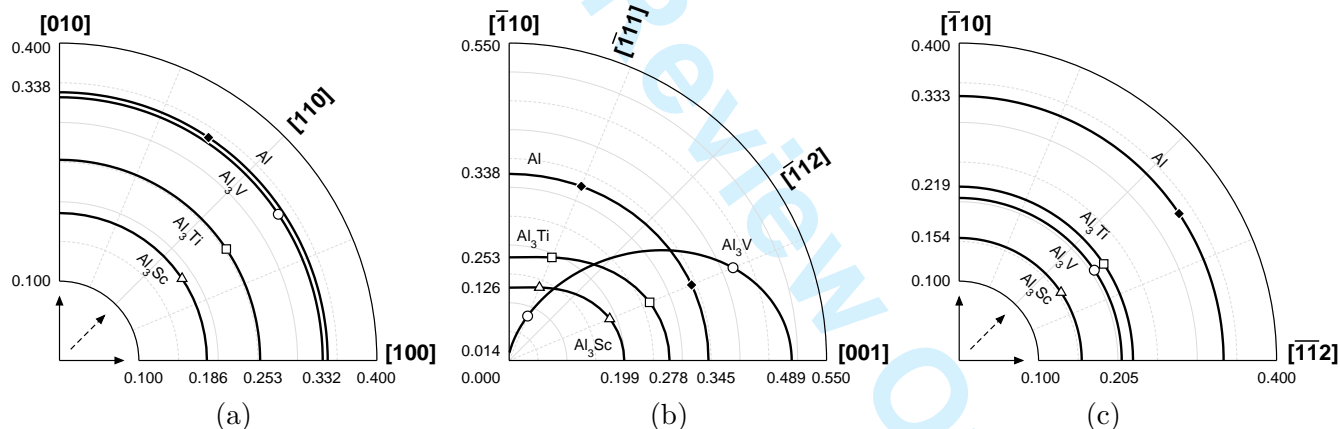


Figure 11. The anisotropy of Poisson ratio ν for $\text{Al}_3(\text{Sc,Ti,V})$ compounds in $L1_2$ crystal structure (marked as Δ , \square , and \circ , respectively). The (a), (b), (c) graphs correspond to tension in $[001]$, $[110]$, and $[111]$ direction, respectively. For comparison, the anisotropy for pure Al (fcc) is also presented (marked as \blacklozenge).

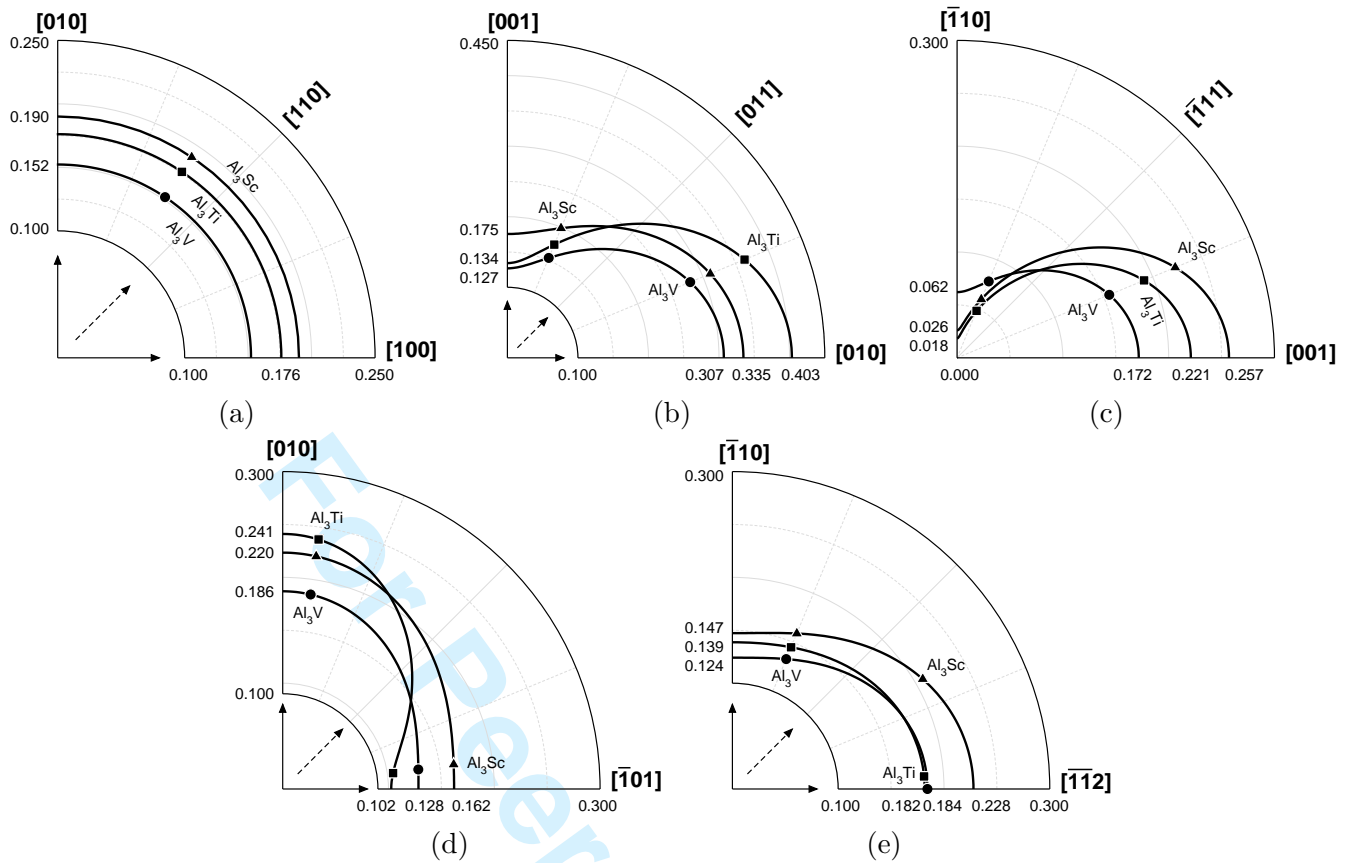
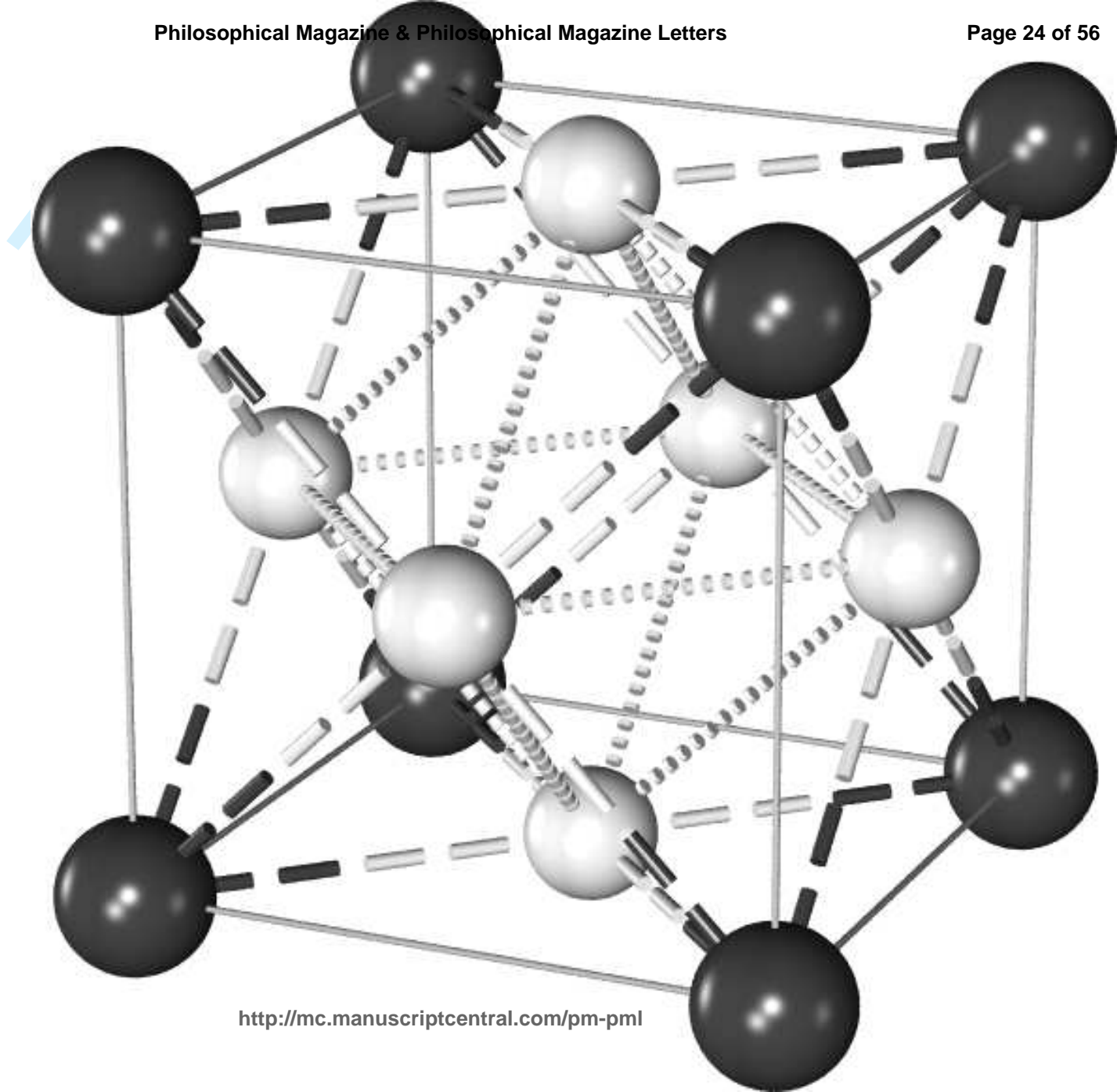


Figure 12. The anisotropy of Poisson ratio ν for $\text{Al}_3(\text{Sc,Ti,V})$ compounds in $D0_{22}$ crystal structure (marked as \blacktriangle , \blacksquare , and \bullet , respectively). The (a-e) graphs correspond to tension in [001], [100], [110], [101], and [111] direction, respectively.

Table 1. Computed structural and elastic properties of trialuminide compounds; ΔE represents structural energy difference $D0_{22}$ - $L1_2$ in meV/atom (for Al_3Cr we used $L1_2$ -ferromagnetic state as a reference state), a and c/a denote lattice constants in Å, V_0 equilibrium volume in Å³/atom, B bulk modulus in GPa, and c_{ij} a appropriate set of elastic constants, all in GPa. The superscript "fm" and "afm" denotes the ferromagnetic and anti-ferromagnetic configuration, respectively. The values for two well ductile materials, Al and Ni_3Al , are presented for comparison.

System	Symmetry	ΔE	a	c/a	V_0	B	c_{11}	c_{12}	c_{13}	c_{33}	c_{44}	c_{66}
Al	A1	...	4.046	...	16.56	75	111	57	28	...
Al_3Sc	$D0_{22}$	91.200	4.021	2.194	17.83	84	158	60	42	158	63	93
Al_3Sc	$L1_2$...	4.104	...	12.28	87	179	41	78	...
Al_3Ti	$D0_{22}$	-25.853	3.851	2.227	15.93	107	192	84	49	216	94	122
Al_3Ti	$L1_2$...	3.977	...	15.74	107	192	65	74	...
Al_3V	$D0_{22}$	-147.292	3.766	2.207	14.73	118	233	77	47	258	104	129
Al_3V	$L1_2$...	3.897	...	14.79	118	178	88	87	...
$\text{Al}_3\text{Cr}^{\text{afm}}$	$D0_{22}$	-62.011	3.794	2.126	14.51	105	189	77	45	235	98	110
$\text{Al}_3\text{Cr}^{\text{fm}}$	$D0_{22}$	-40.207	3.769	2.139	14.32	118	200	106	52	242	100	116
Al_3Cr	$L1_2$...	3.851	...	14.28	126	106	136	92	...
$\text{Al}_3\text{Cr}^{\text{fm}}$	$L1_2$...	3.897	...	14.80	108	191	66	73	...
Ni_3Al	$L1_2$...	3.566	...	11.33	182	234	156	120	...
$\text{Ni}_3\text{Al}^{\text{fm}}$	$L1_2$...	3.567	...	11.35	181	242	151	124	...



1
2
3
4
5
6
7
8
9
10
11
12
13
14
15
16
17
18
19
20
21
22
23
24
25
26
27
28
29
30
31
32
33
34
35
36
37
38
39
40
41
42
43
44
45
46
47
48
49
50
51
52
53
54
55
56
57
58
59
60

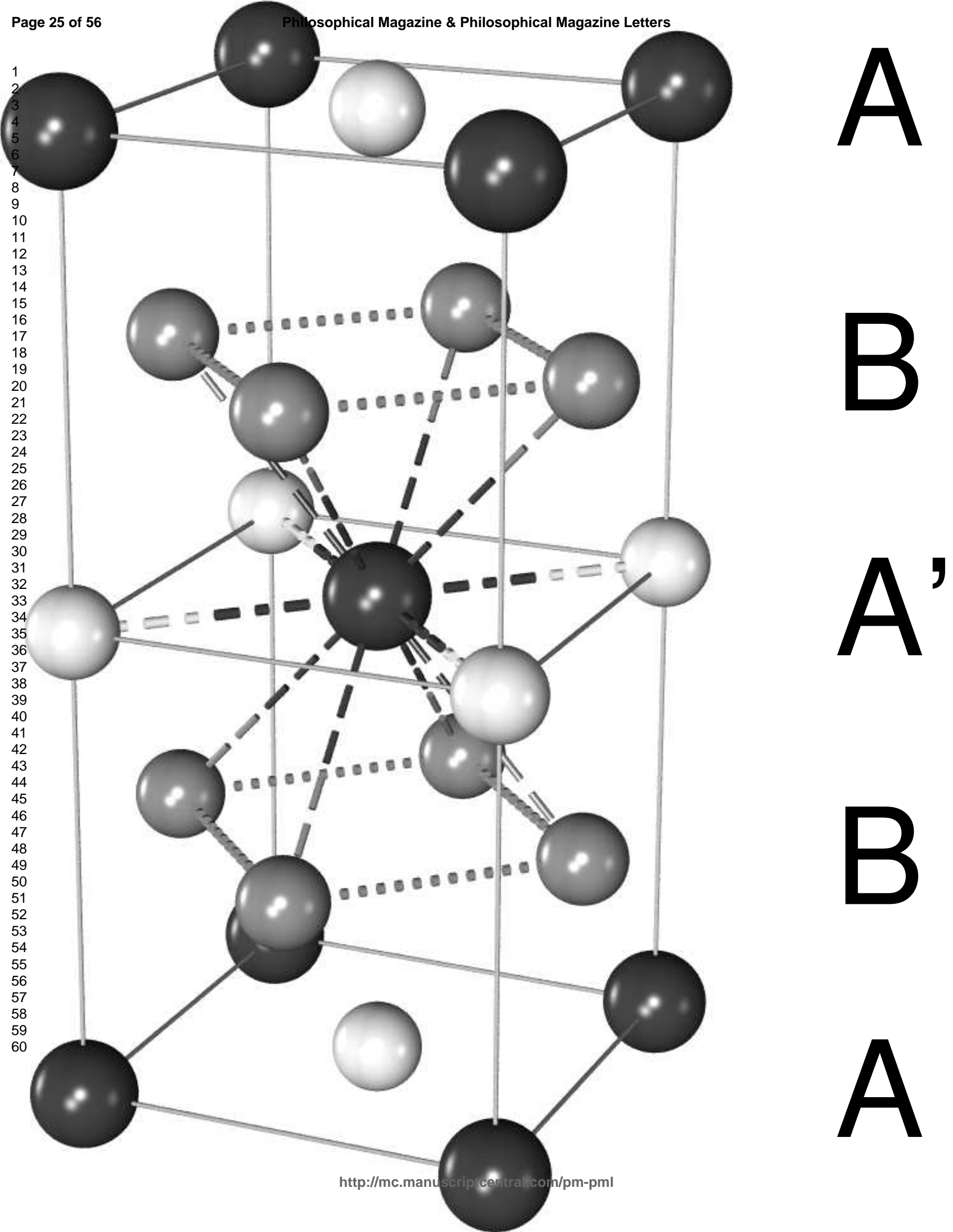
A

B

A'

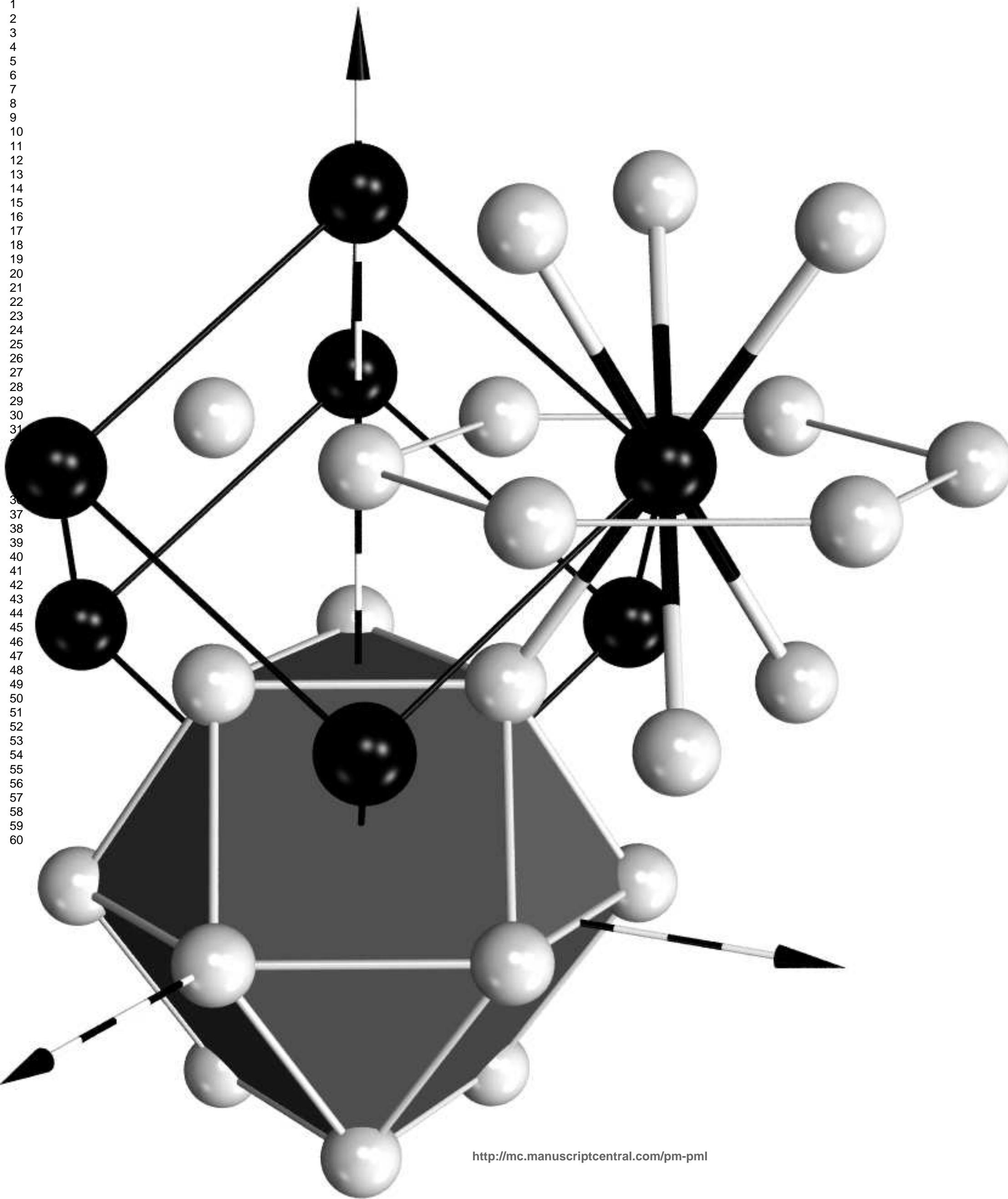
B

A



[111]

1
2
3
4
5
6
7
8
9
10
11
12
13
14
15
16
17
18
19
20
21
22
23
24
25
26
27
28
29
30
31
32
33
34
35
36
37
38
39
40
41
42
43
44
45
46
47
48
49
50
51
52
53
54
55
56
57
58
59
60



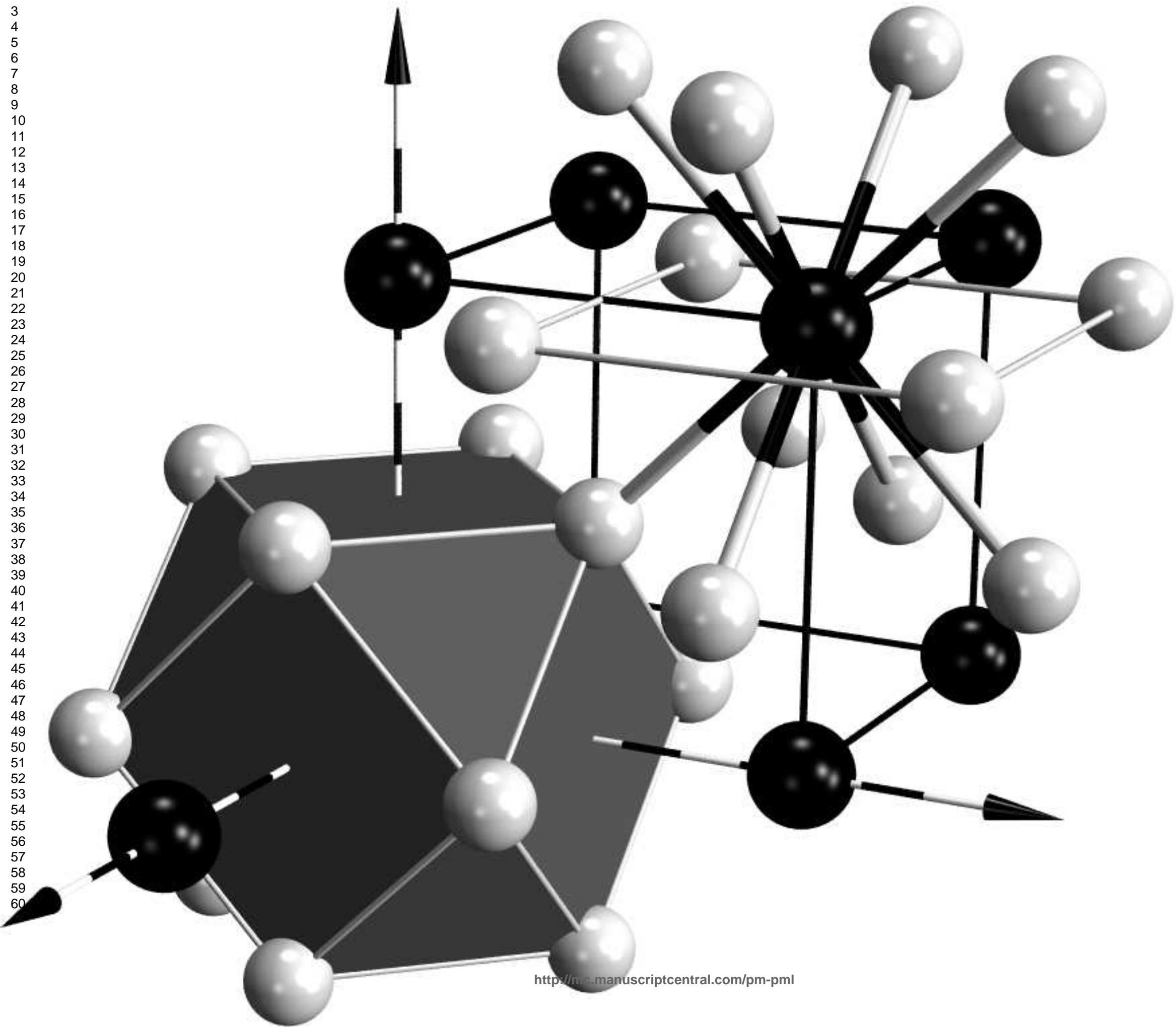
C

D

E

[001]

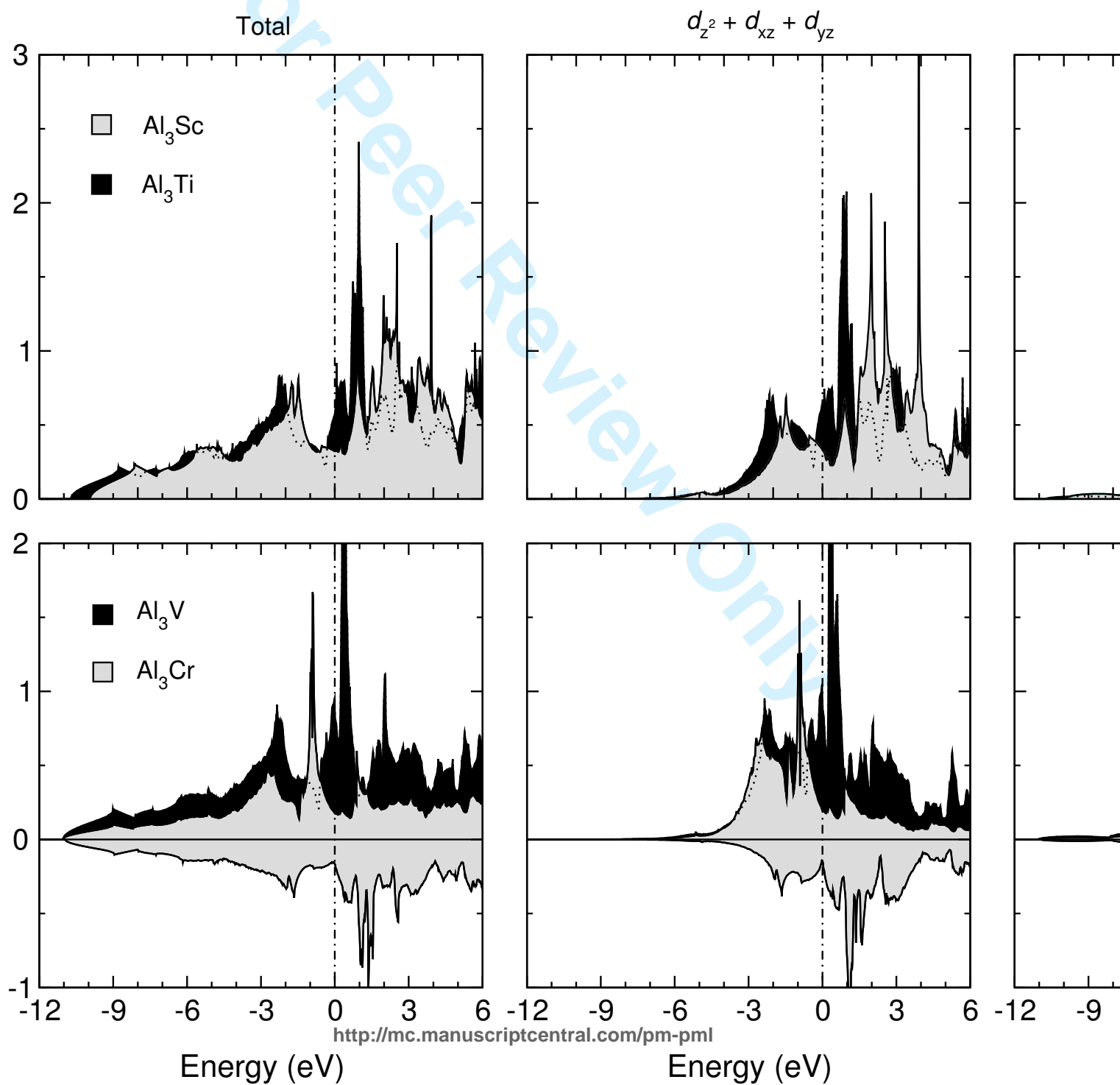
1
2
3
4
5
6
7
8
9
10
11
12
13
14
15
16
17
18
19
20
21
22
23
24
25
26
27
28
29
30
31
32
33
34
35
36
37
38
39
40
41
42
43
44
45
46
47
48
49
50
51
52
53
54
55
56
57
58
59
60



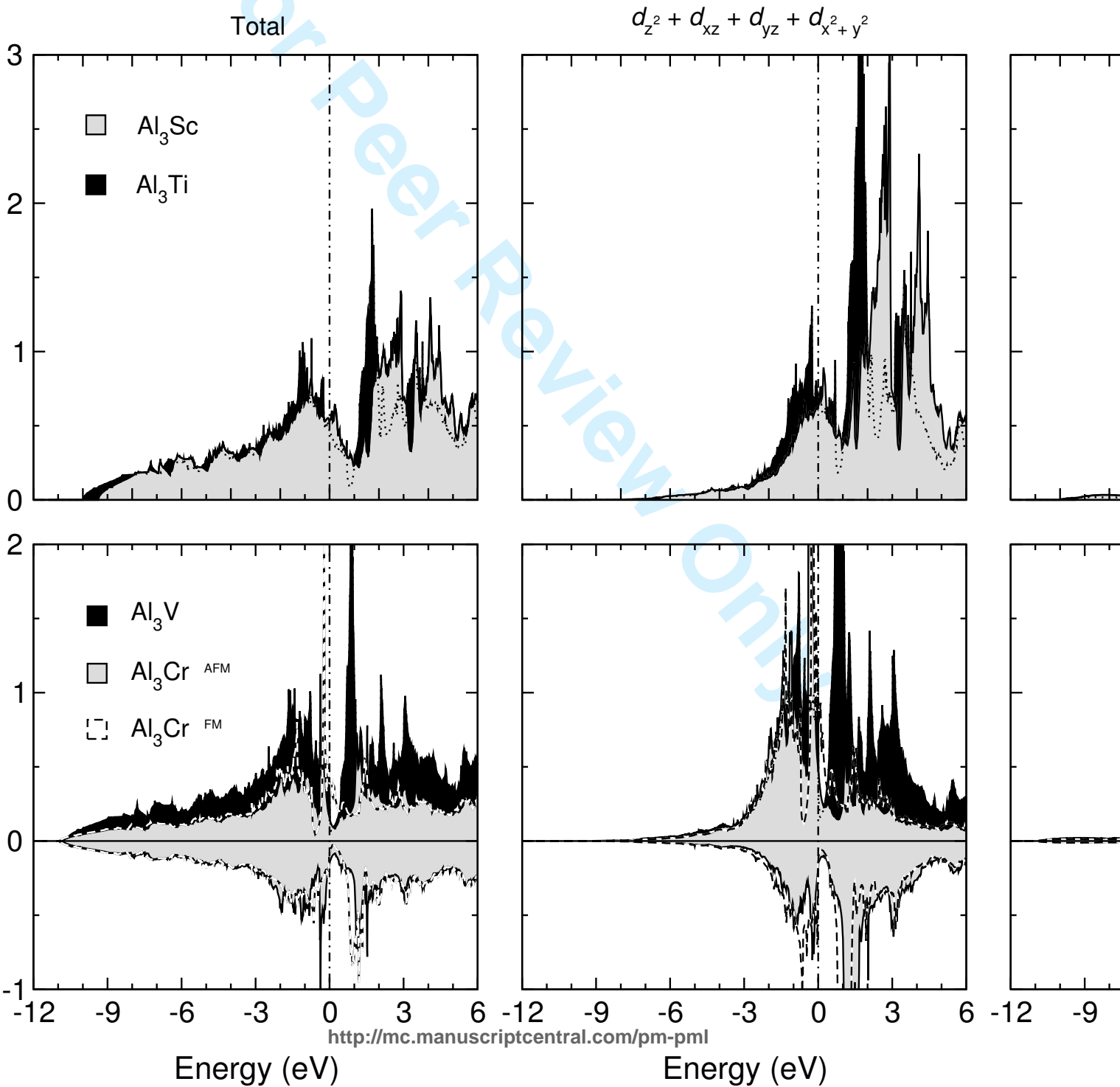
B

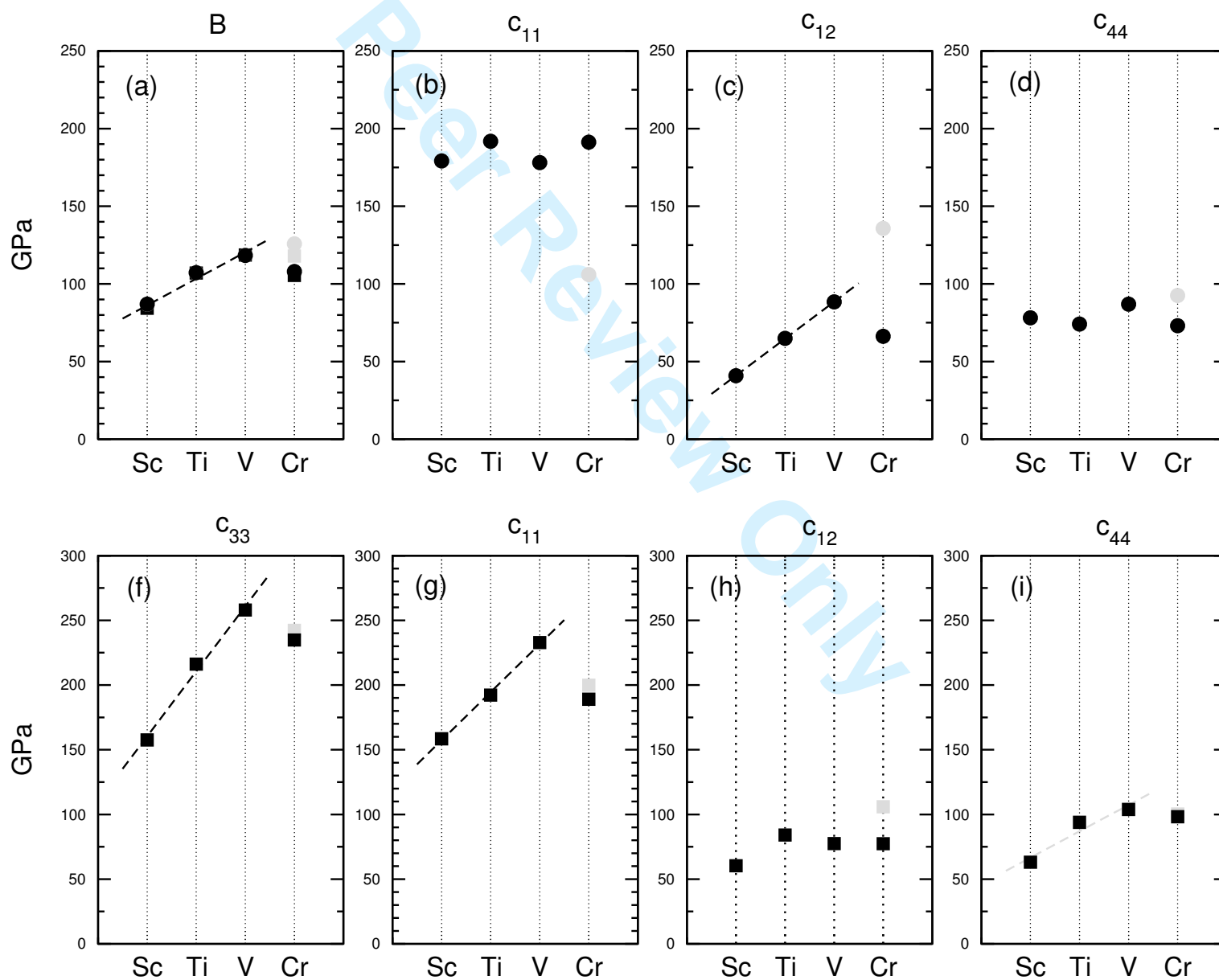
A

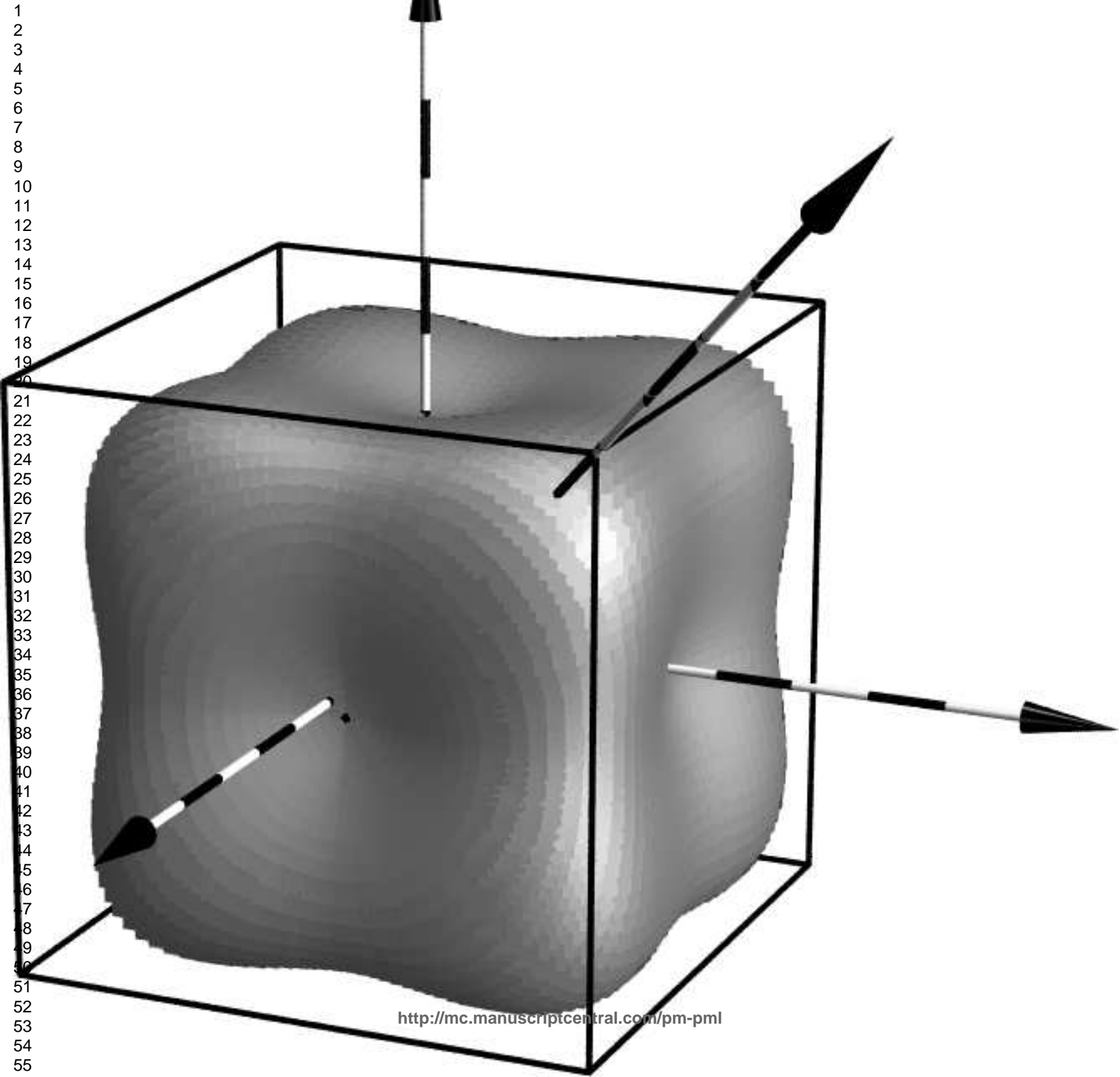
B



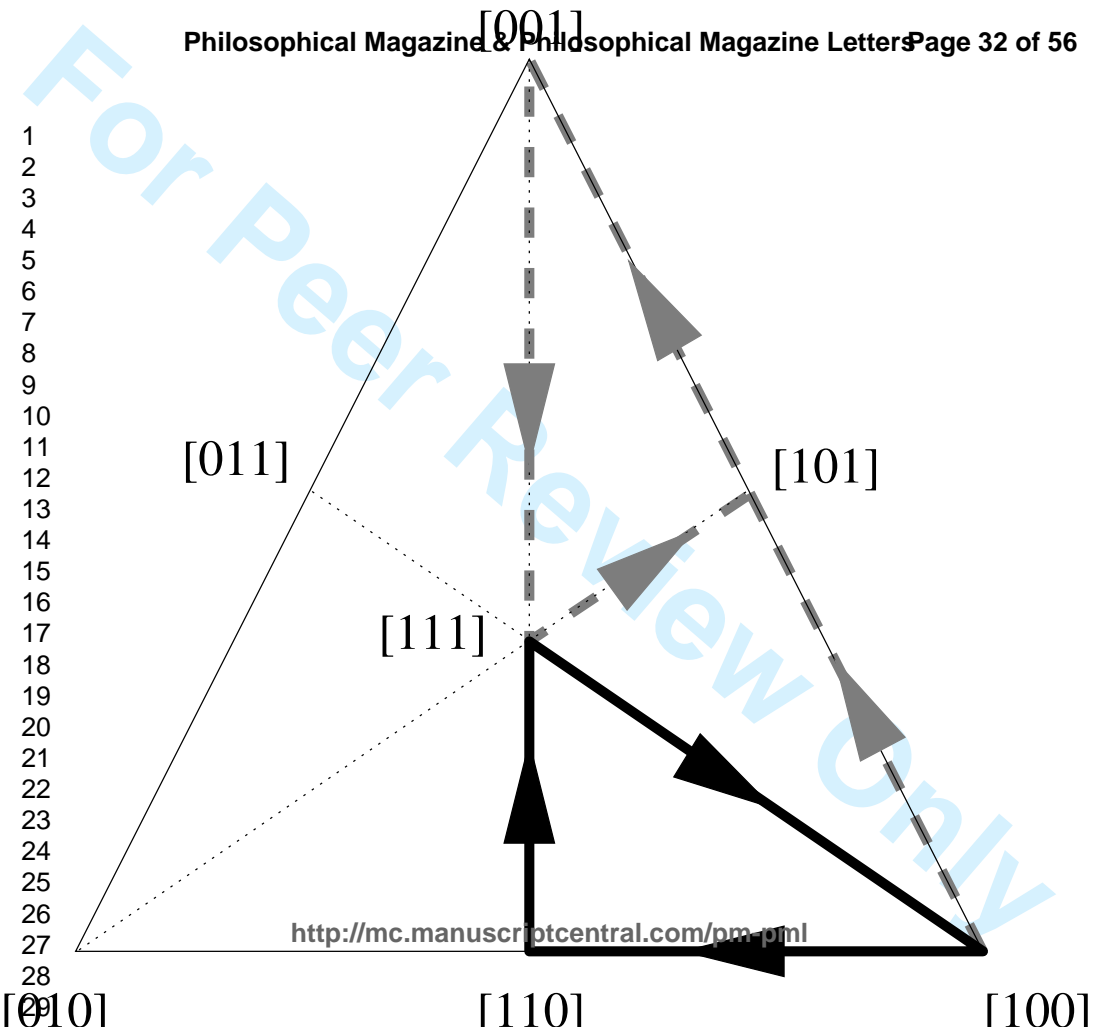
1
2
3
4
5
6
7
8
9
10
11
12
13
14
15
16
17
18
19
20
21
22
23
24
25
26
27
28
29
30
31
32
33
34
35
36
37
38
39
40
41
42
43
44
45
46
47
48
49
50
51
52
53
54
55
56
57
58
59
60



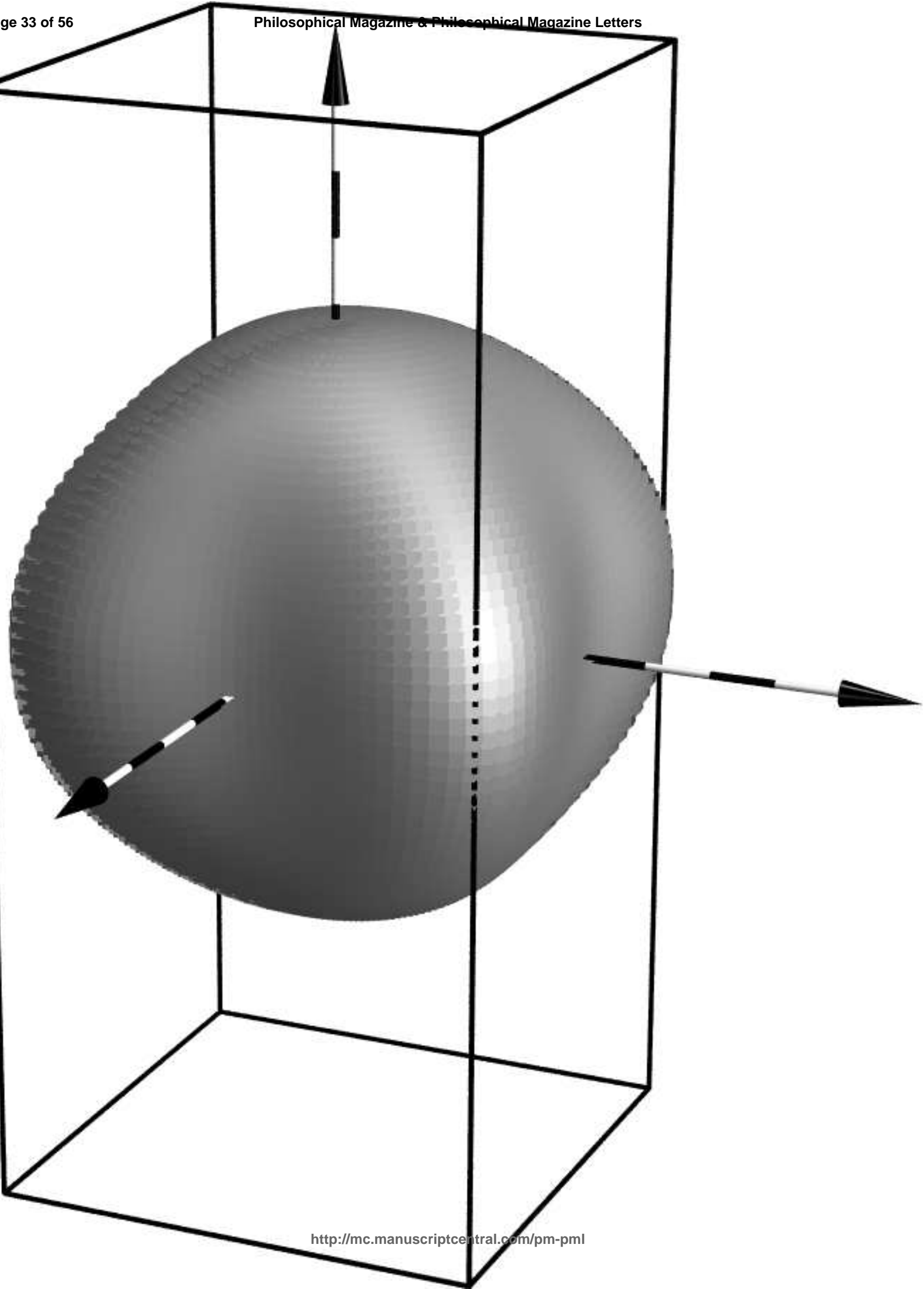


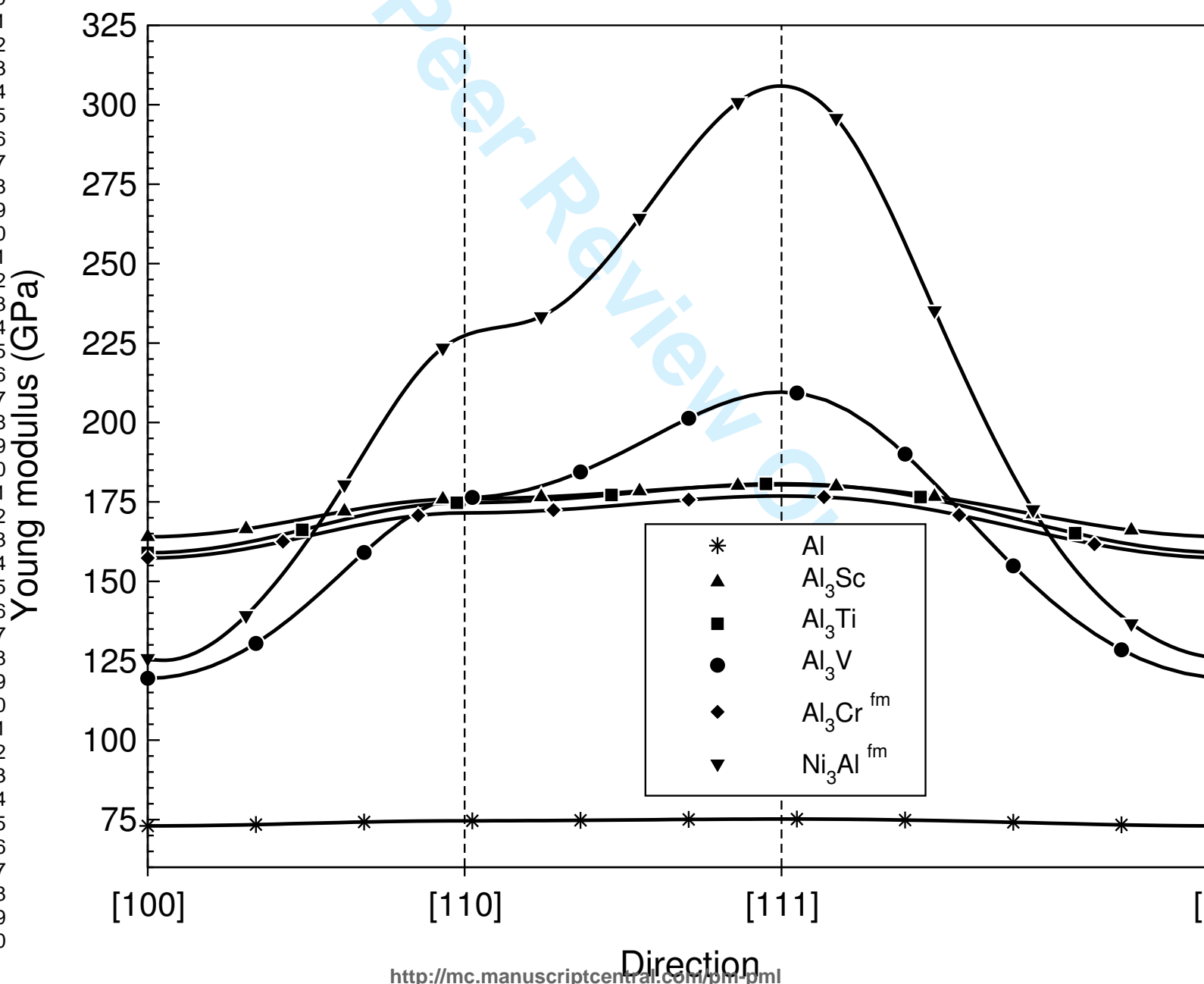


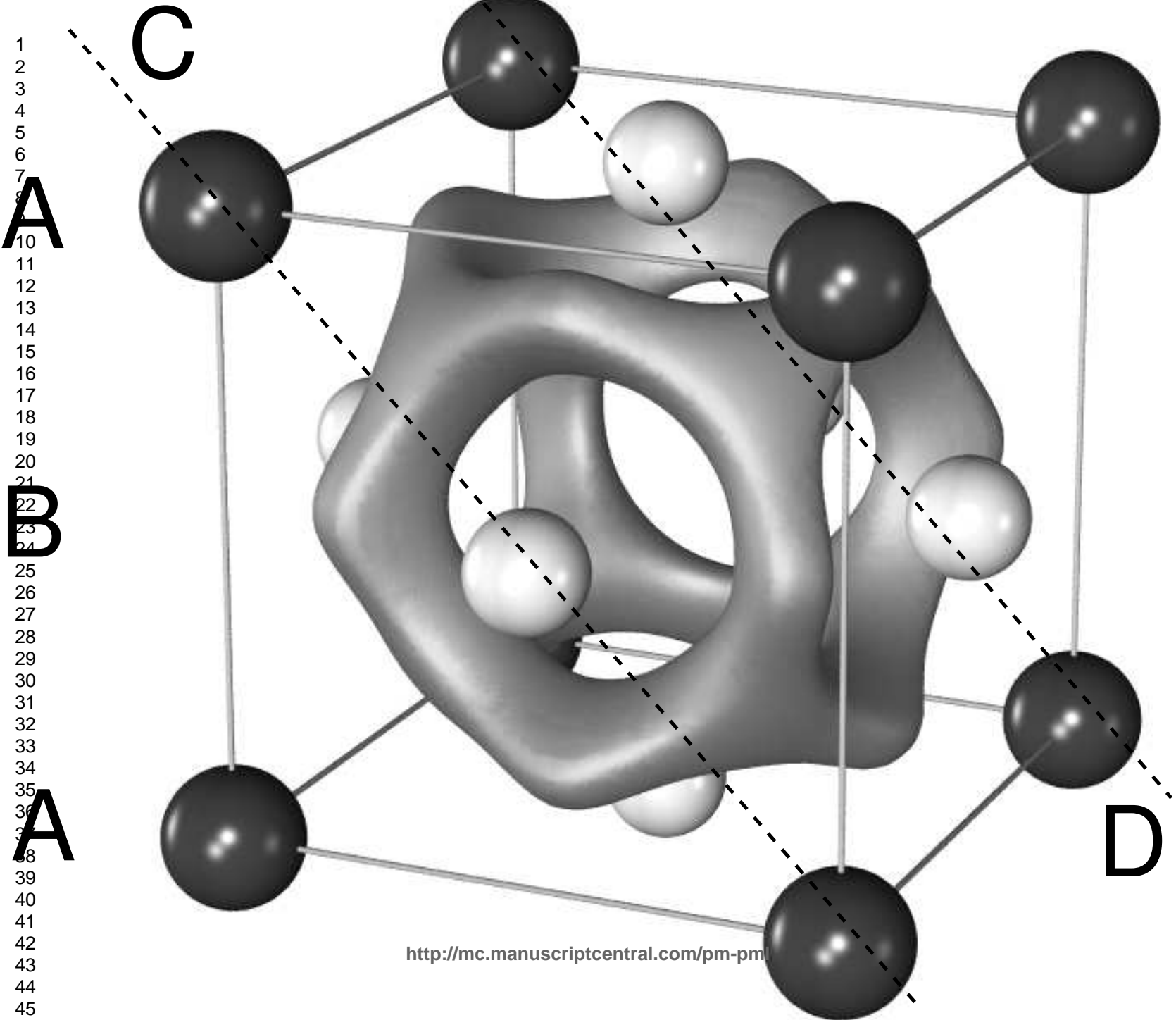
1
2
3
4
5
6
7
8
9
10
11
12
13
14
15
16
17
18
19
20
21
22
23
24
25
26
27
28
29



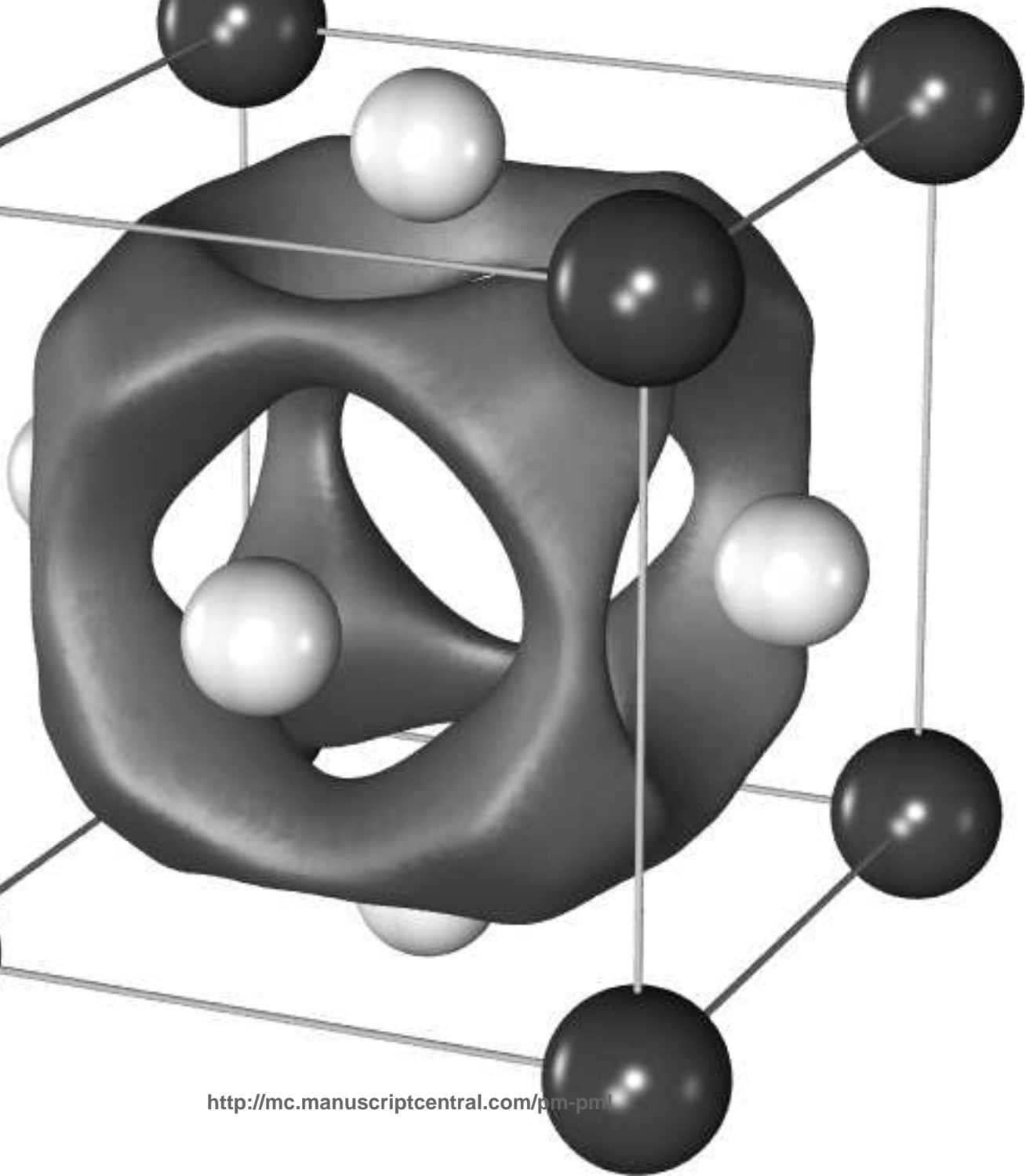
1
3
4
5
6
7
8
9
10
11
12
13
14
15
16
17
18
19
20
21
22
23
24
25
26
27
28
29
30
31
32
33
34
35
36
37
38
39
40
41
42
43
44
45
46
47
48
49
50
51
52
53
54
55
56
57
58
59
60



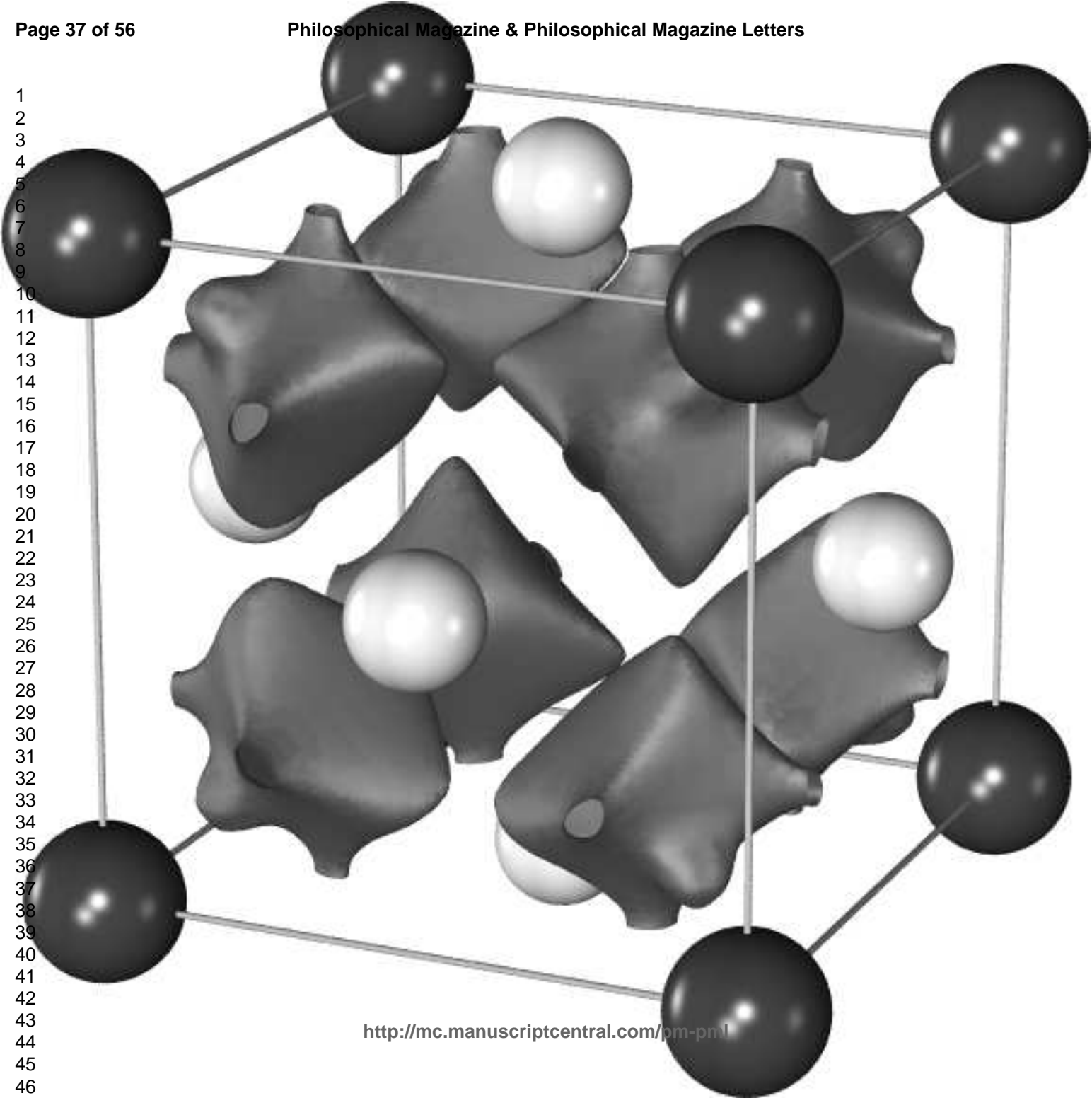




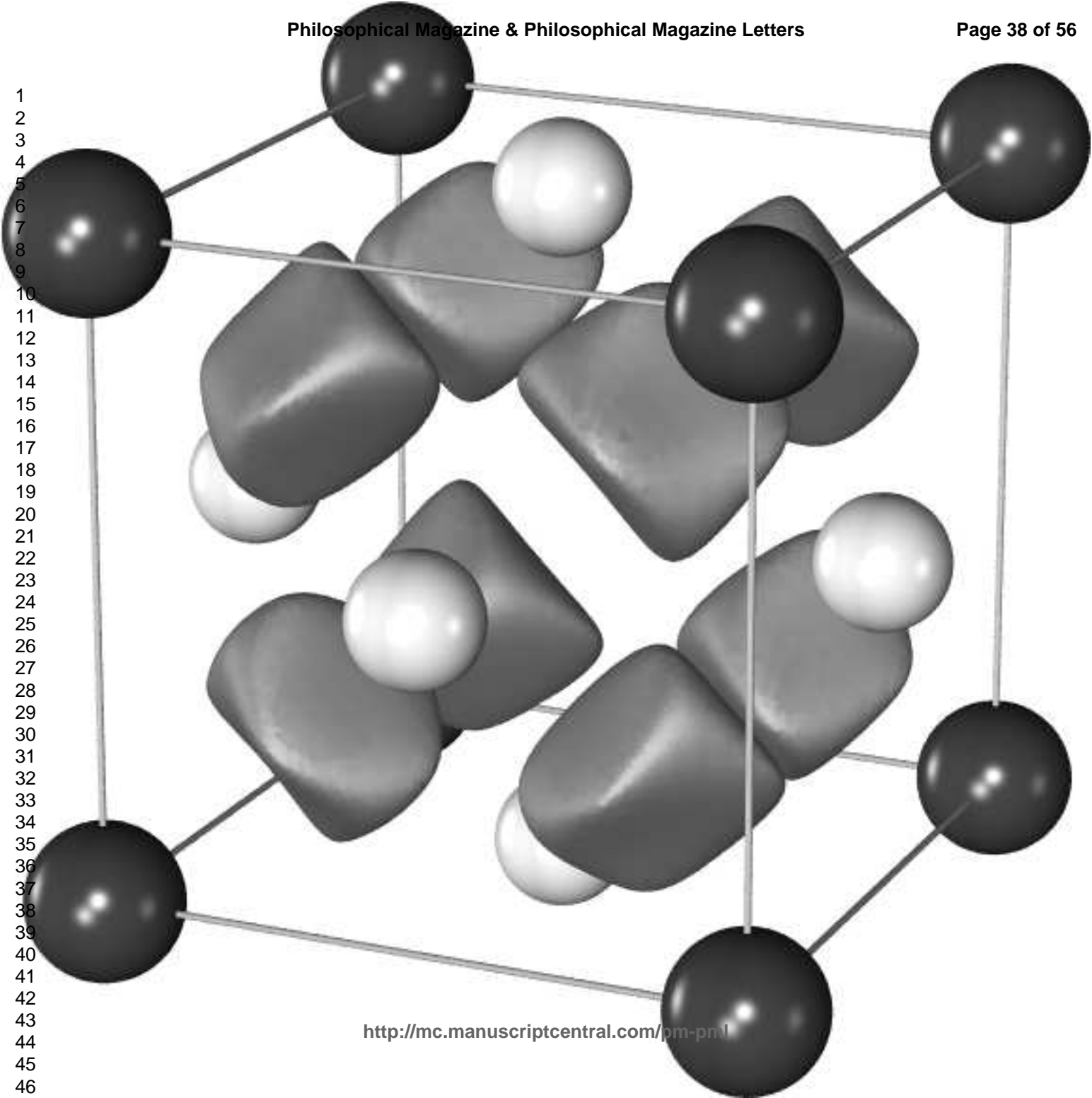
1
2
3
4
5
6
7
8
9
10
11
12
13
14
15
16
17
18
19
20
21
22
23
24
25
26
27
28
29
30
31
32
33
34
35
36
37
38
39
40
41
42
43
44
45
46
47



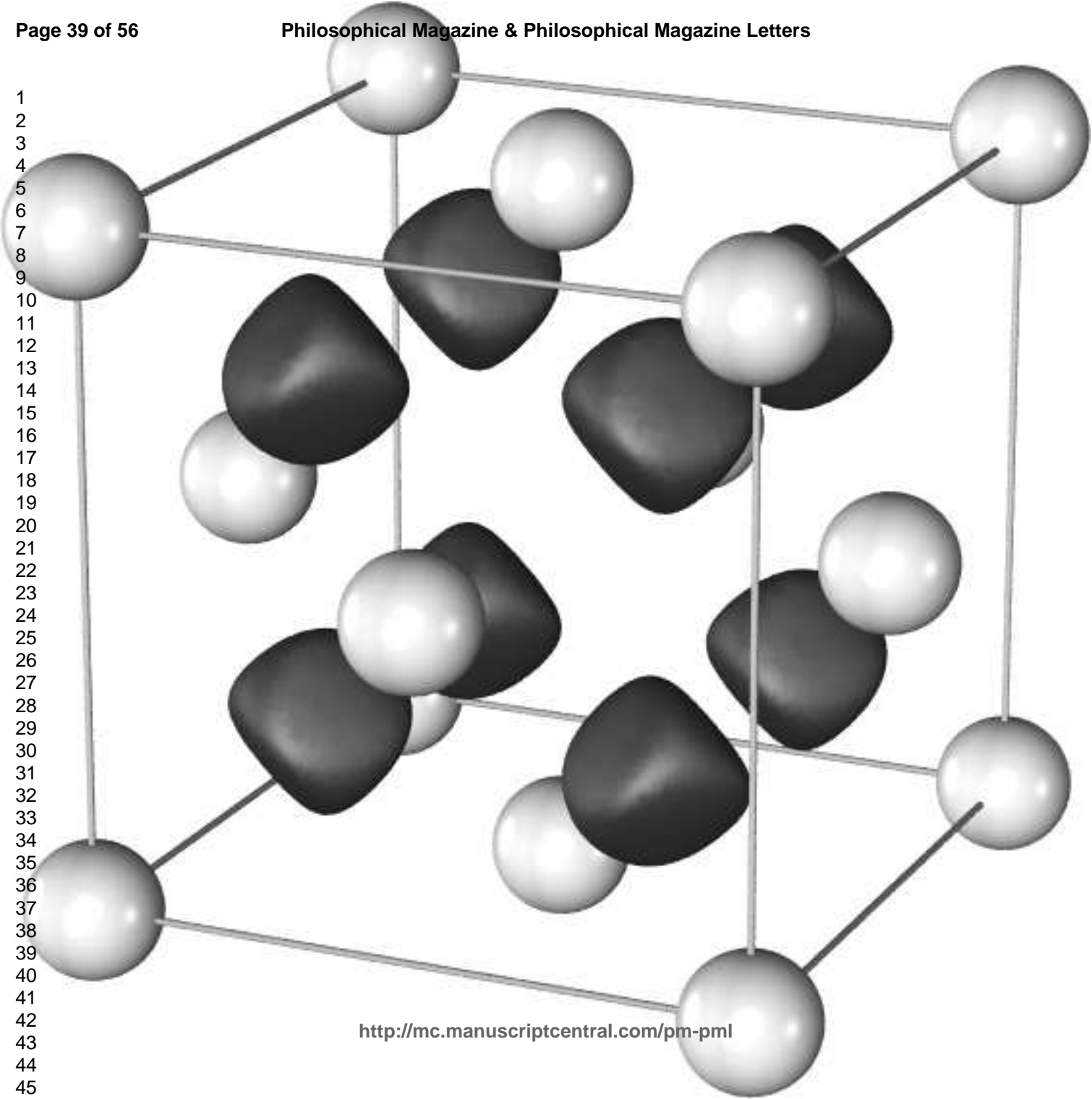
1
2
3
4
5
6
7
8
9
10
11
12
13
14
15
16
17
18
19
20
21
22
23
24
25
26
27
28
29
30
31
32
33
34
35
36
37
38
39
40
41
42
43
44
45
46

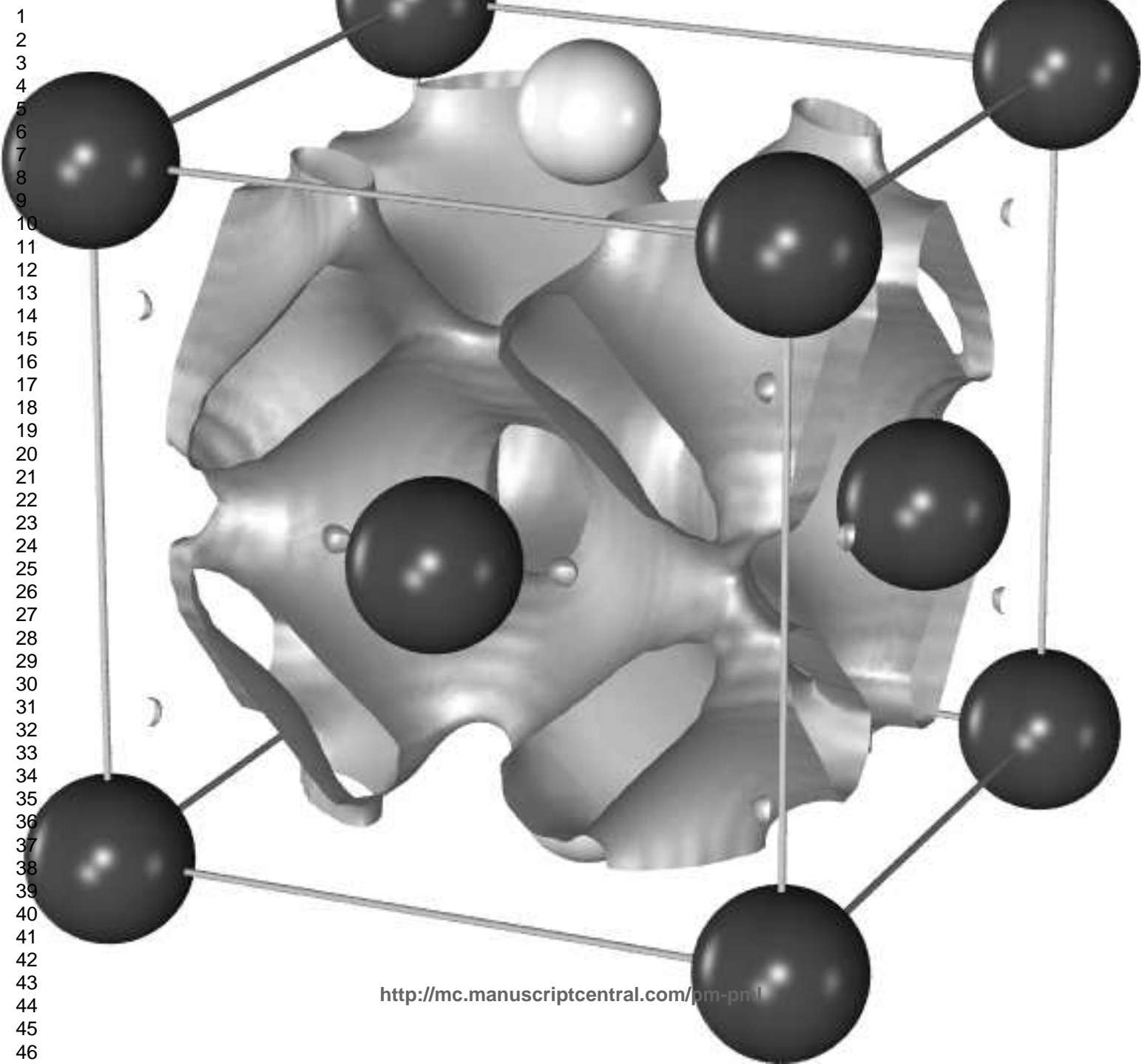


1
2
3
4
5
6
7
8
9
10
11
12
13
14
15
16
17
18
19
20
21
22
23
24
25
26
27
28
29
30
31
32
33
34
35
36
37
38
39
40
41
42
43
44
45
46

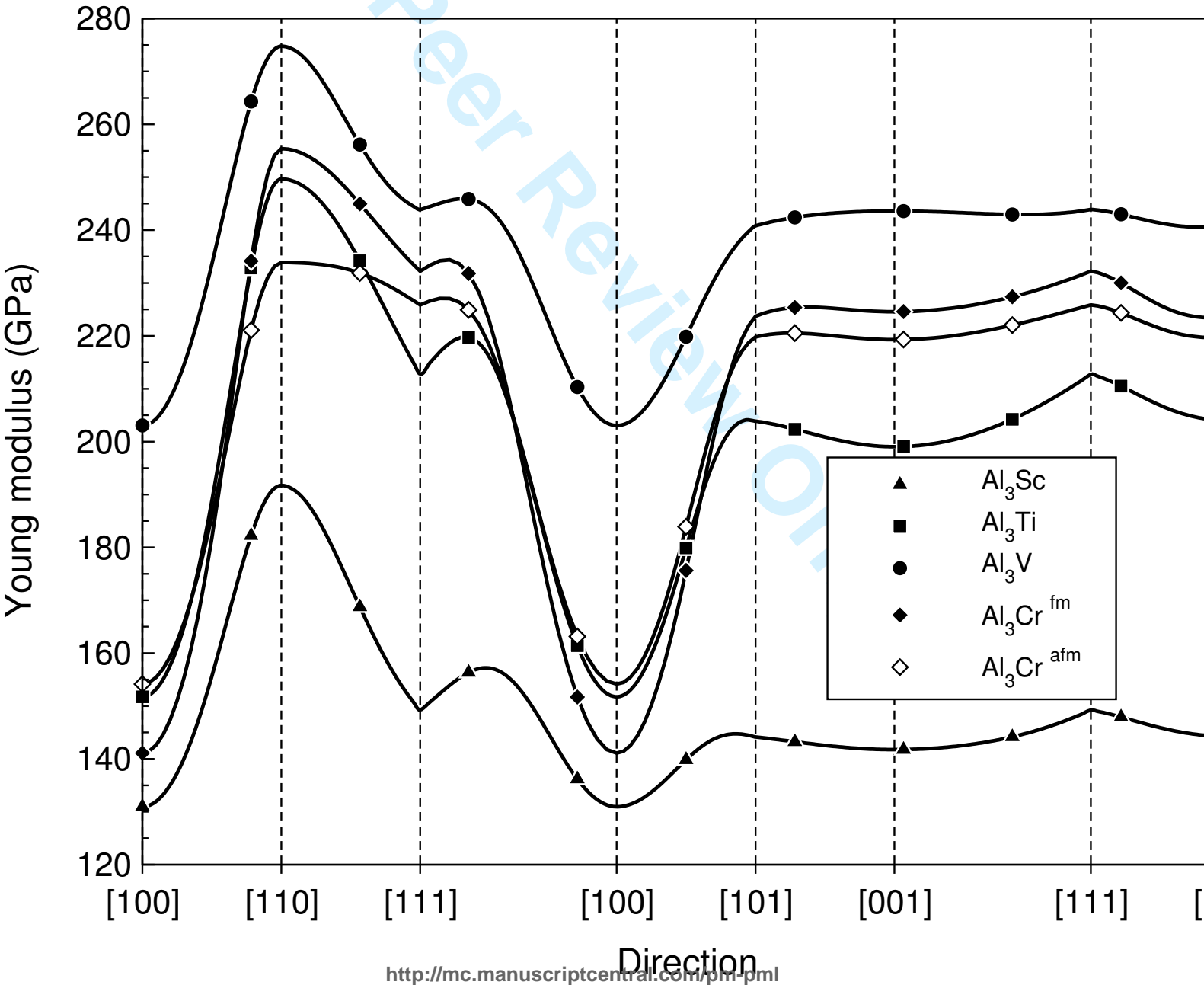


1
2
3
4
5
6
7
8
9
10
11
12
13
14
15
16
17
18
19
20
21
22
23
24
25
26
27
28
29
30
31
32
33
34
35
36
37
38
39
40
41
42
43
44
45

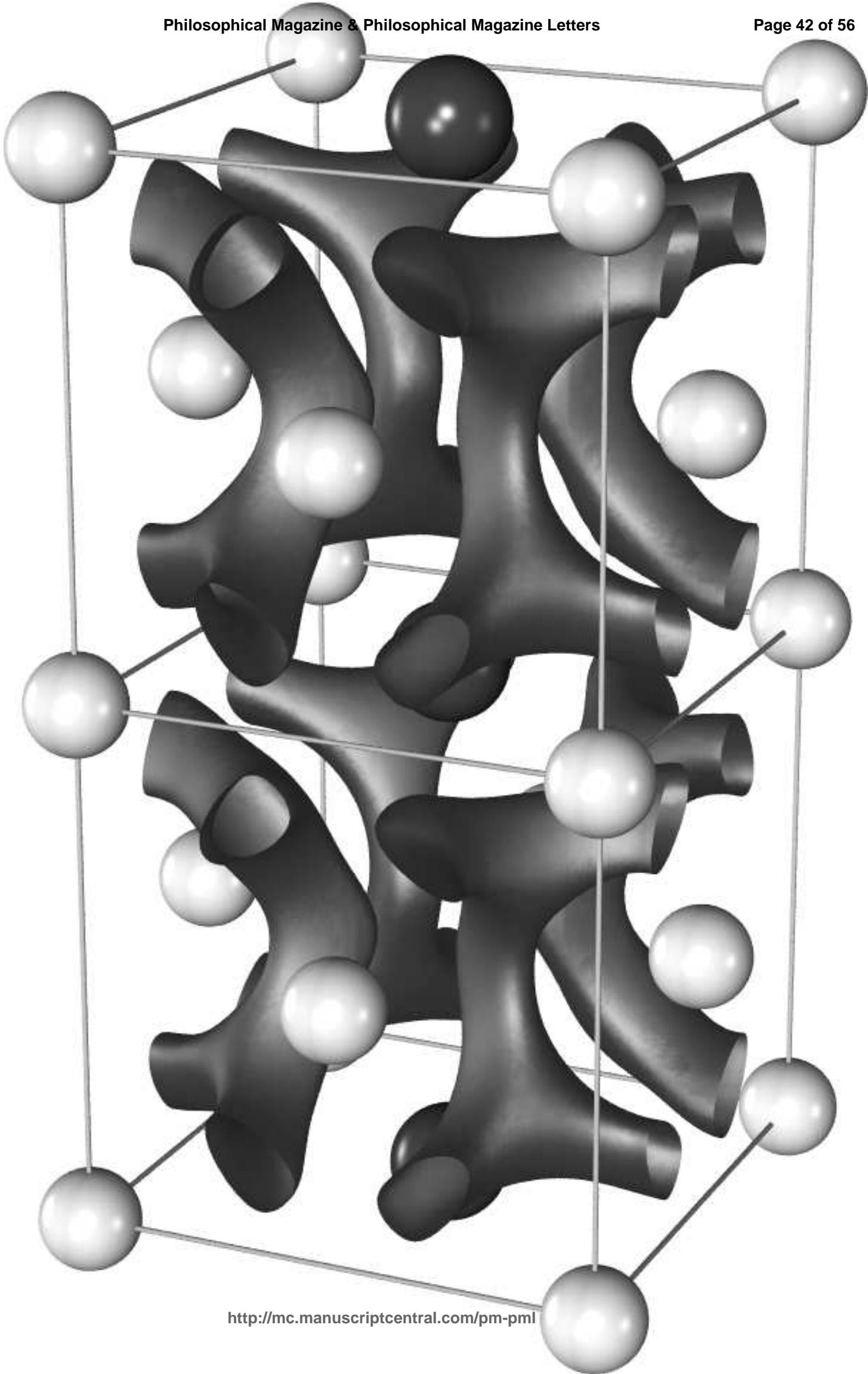




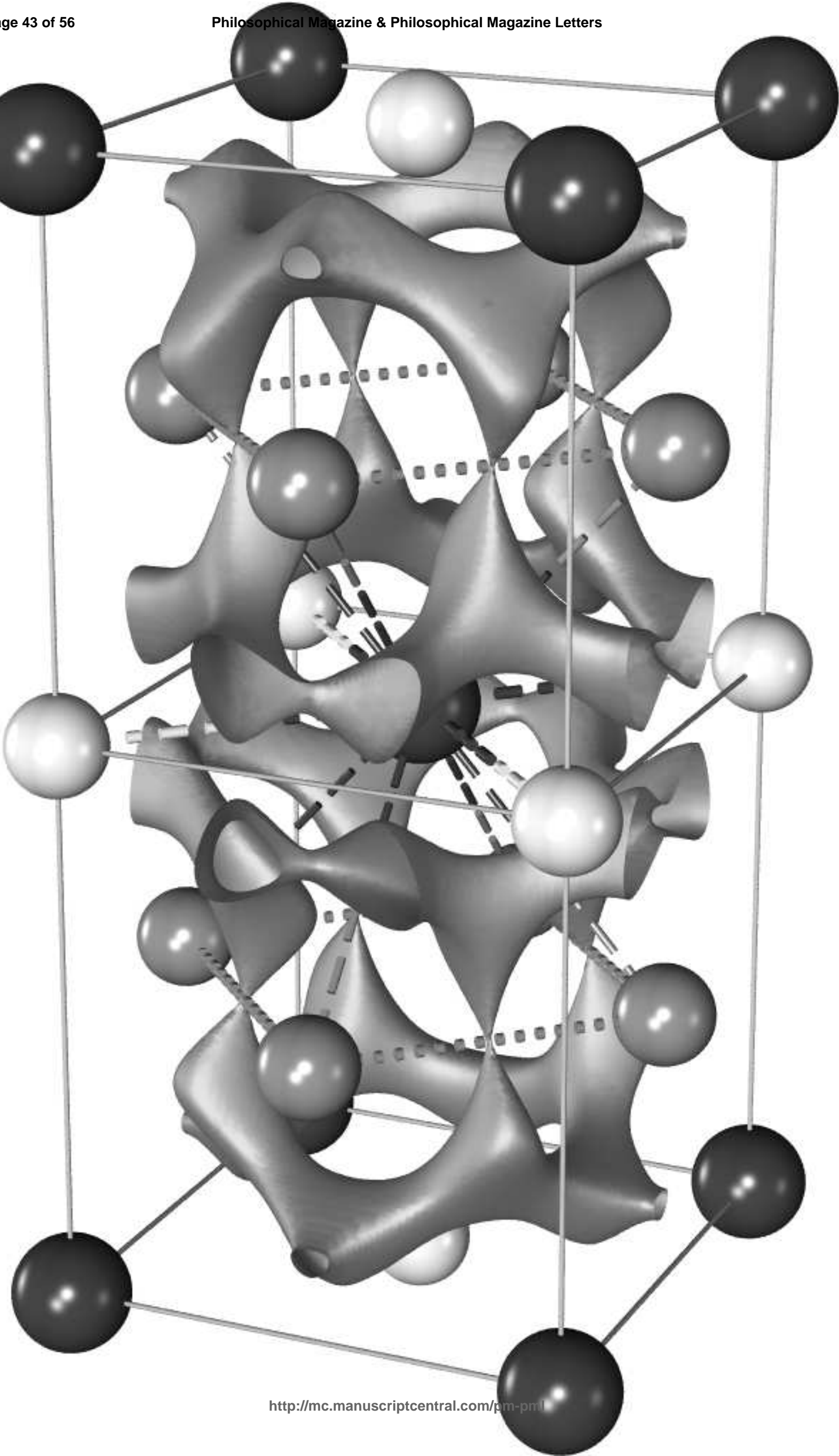
1
2
3
4
5
6
7
8
9
10
11
12
13
14
15
16
17
18
19
20
21
22
23
24
25
26
27
28
29
30
31
32
33
34
35
36
37
38
39
40
41
42
43
44
45
46
47
48
49
50
51
52
53
54
55
56
57
58
59
60

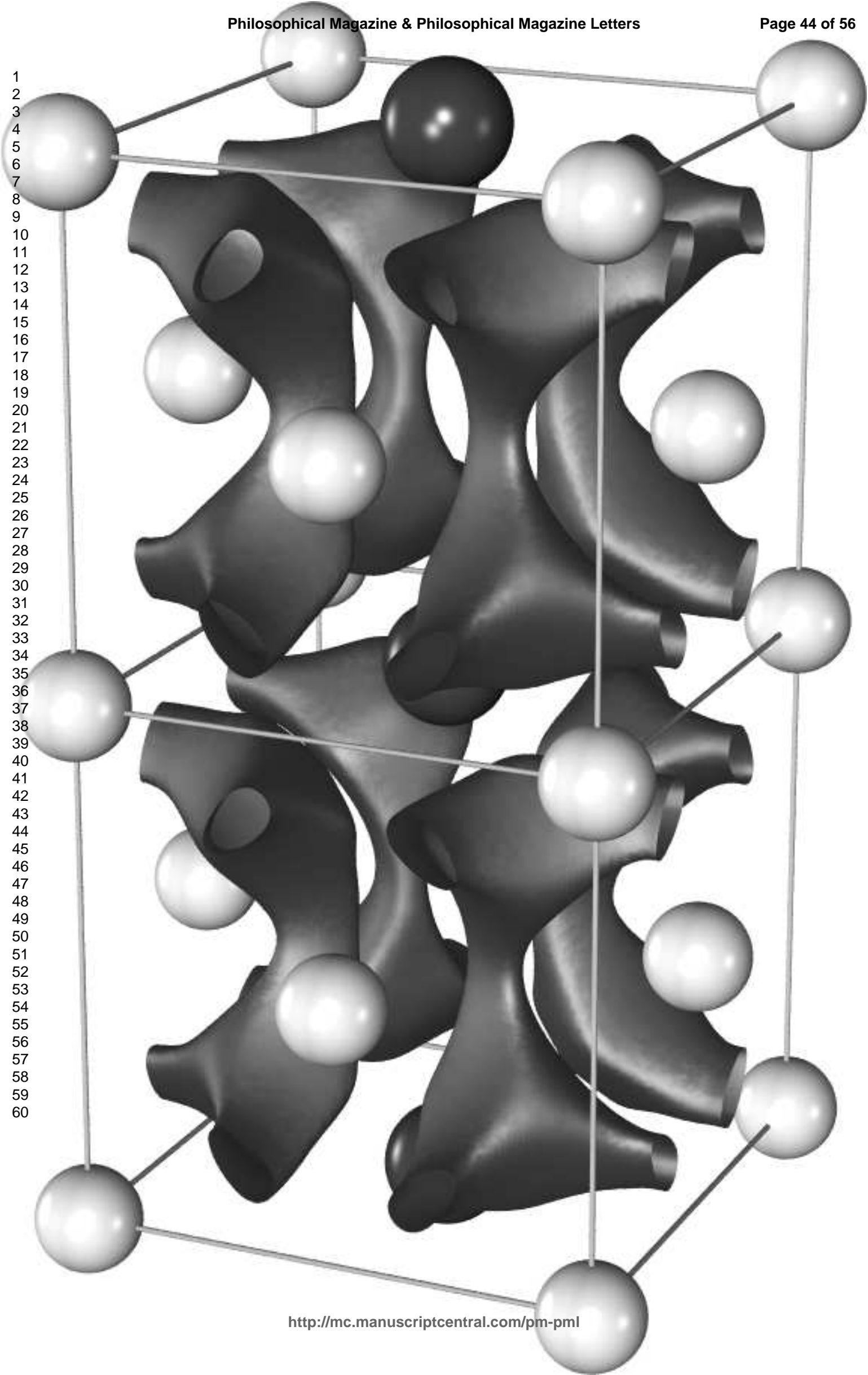


1
2
3
A'
4
5
6
7
8
9
10
11
12
13
14
15
16
B
17
18
19
20
21
22
23
24
25
26
27
28
29
30
31
32
A'
33
34
35
36
37
38
39
40
41
42
43
44
45
46
B
47
48
49
50
51
52
53
54
55
56
57
58
59
60
A'

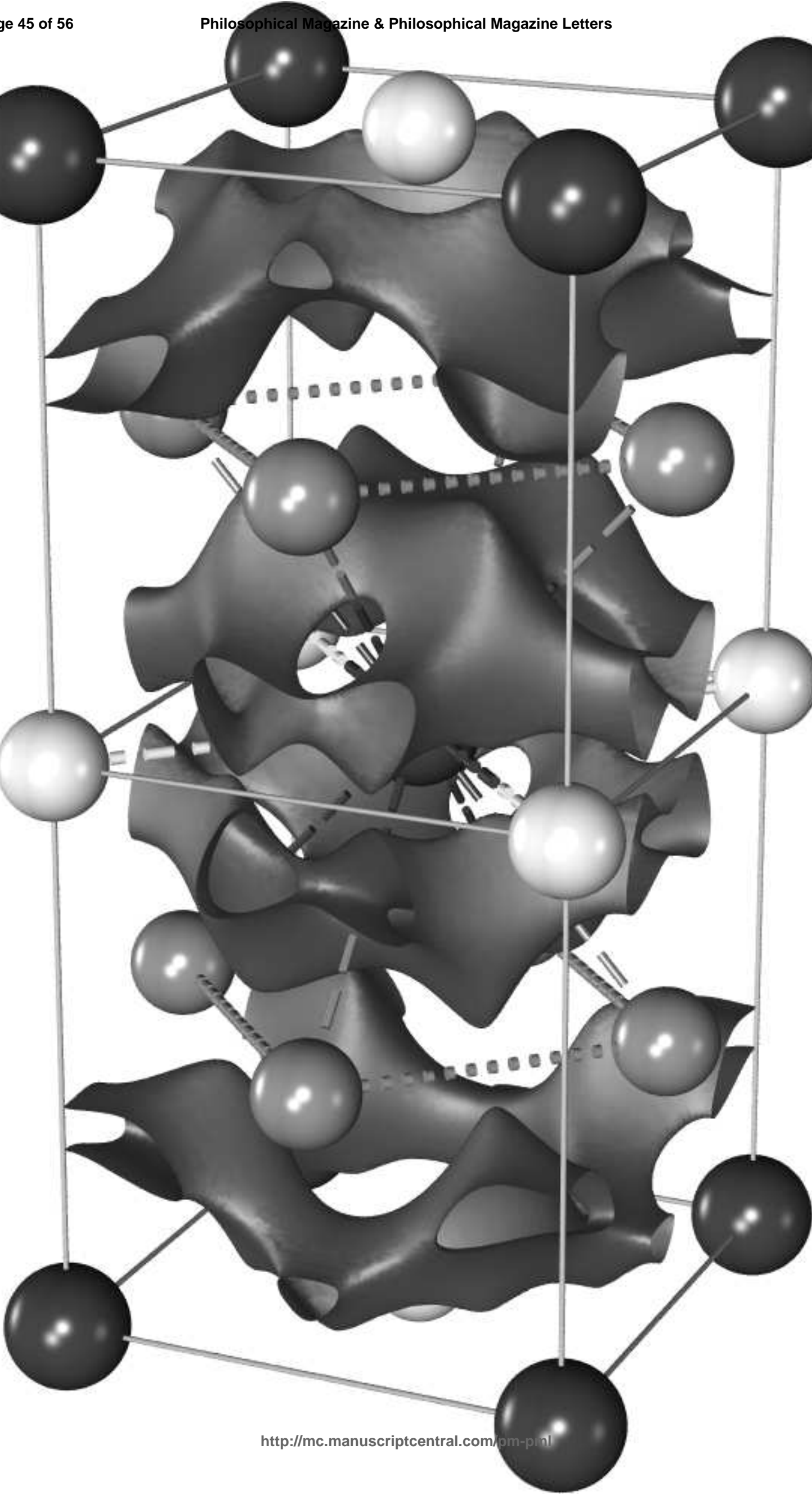


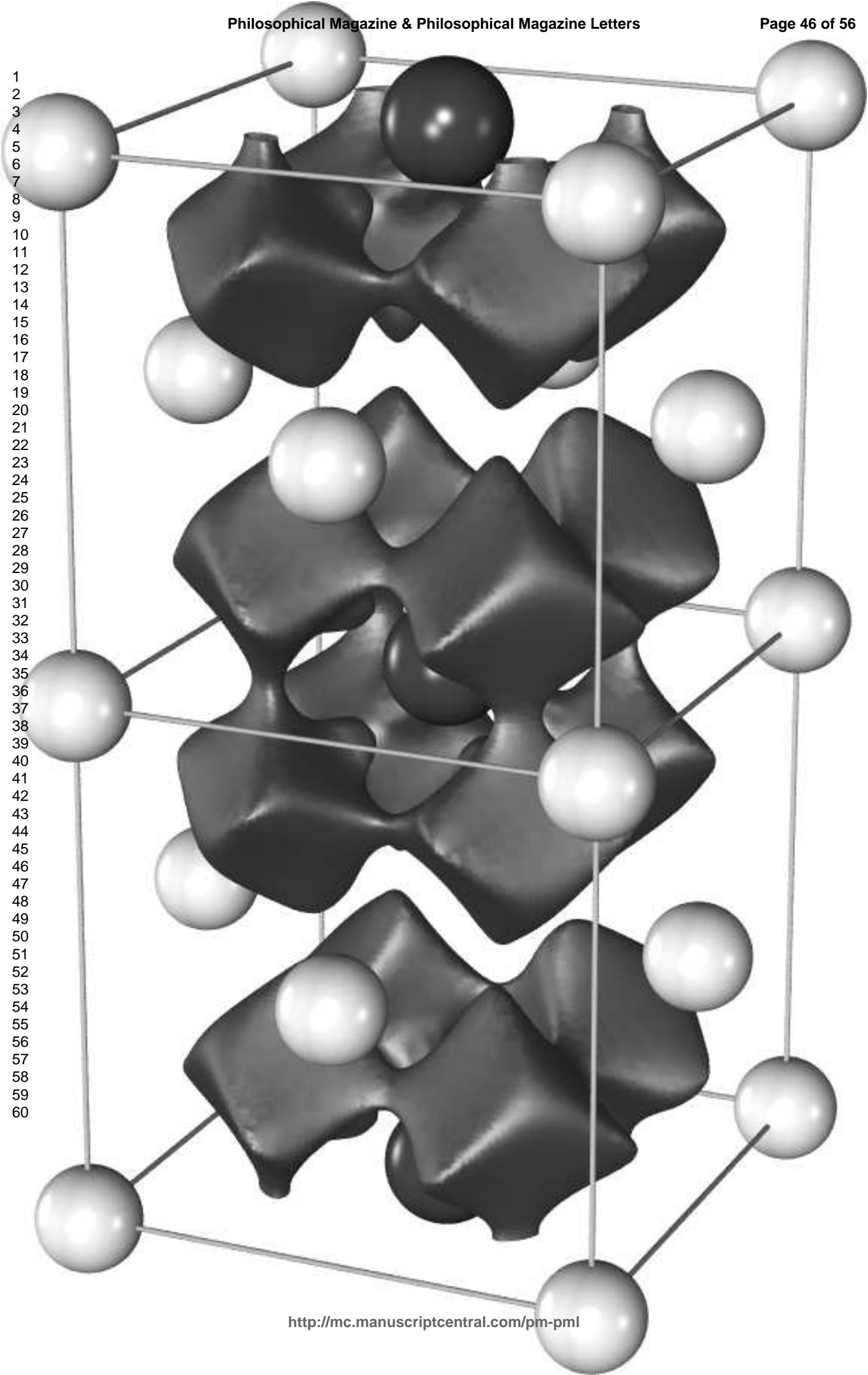
1
2
3
4
5
6
7
8
9
10
11
12
13
14
15
16
17
18
19
20
21
22
23
24
25
26
27
28
29
30
31
32
33
34
35
36
37
38
39
40
41
42
43
44
45
46
47
48
49
50
51
52
53
54
55
56
57
58
59
60



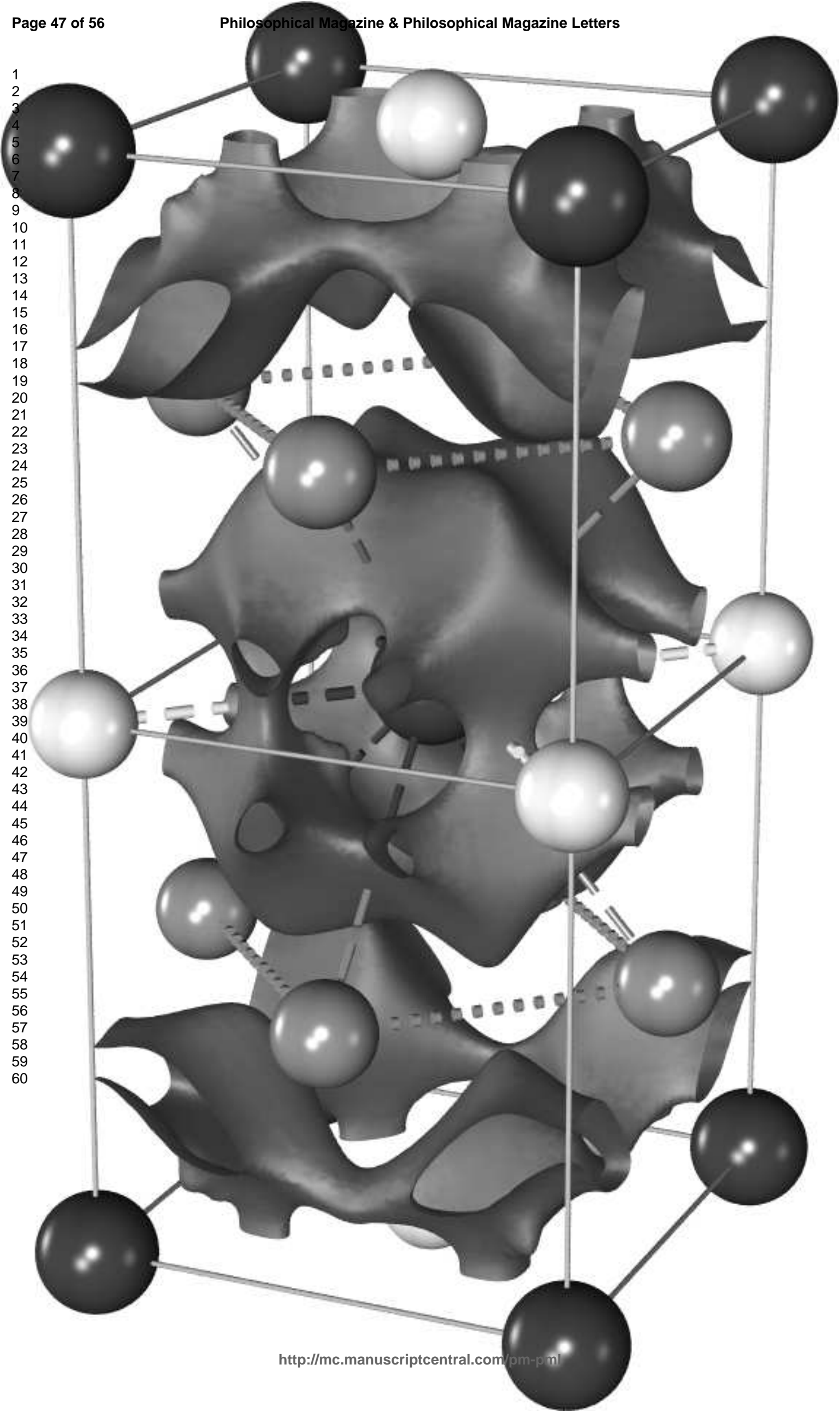


1
2
3
4
5
6
7
8
9
10
11
12
13
14
15
16
17
18
19
20
21
22
23
24
25
26
27
28
29
30
31
32
33
34
35
36
37
38
39
40
41
42
43
44
45
46
47
48
49
50
51
52
53
54
55
56
57
58
59
60

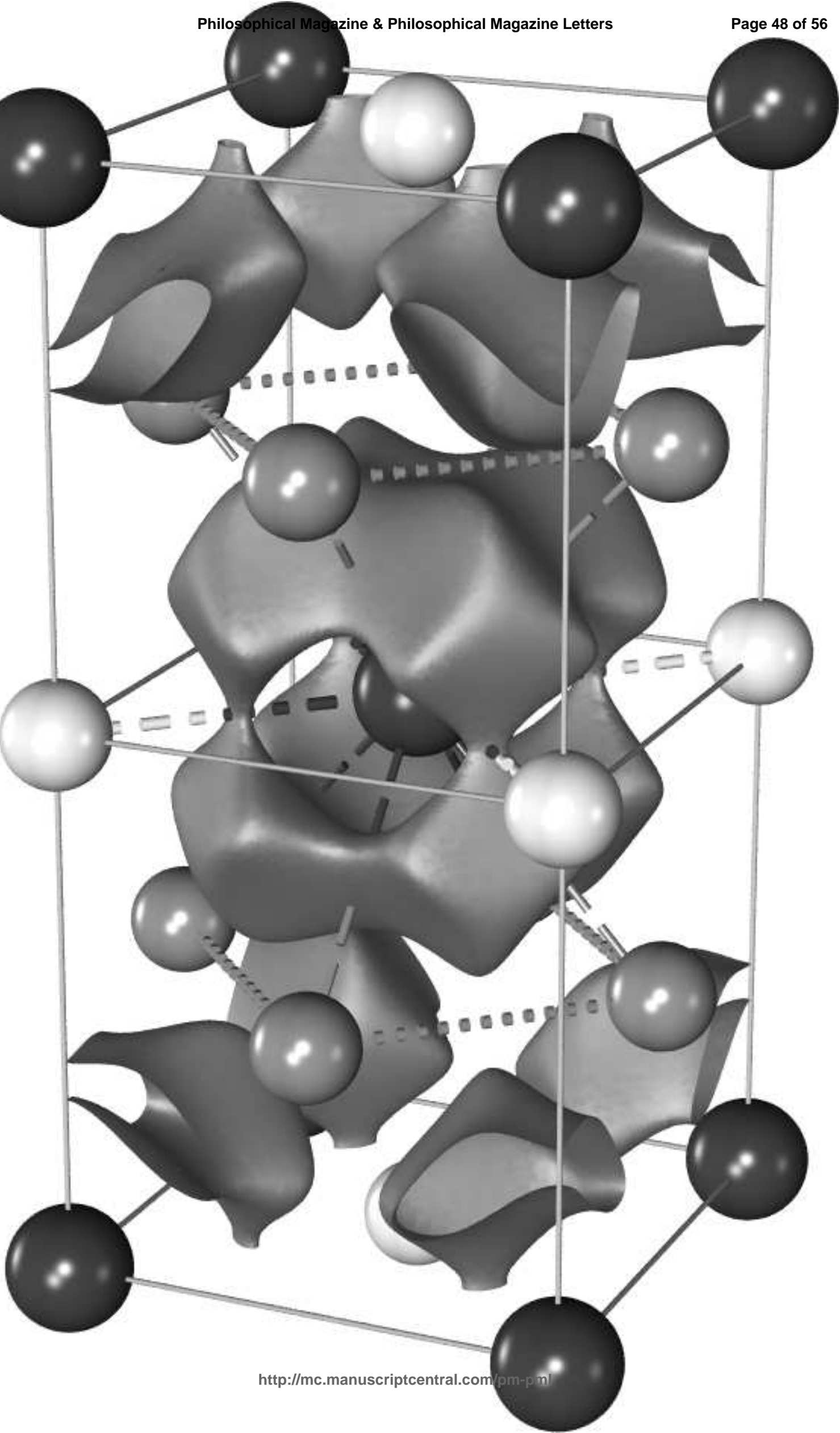




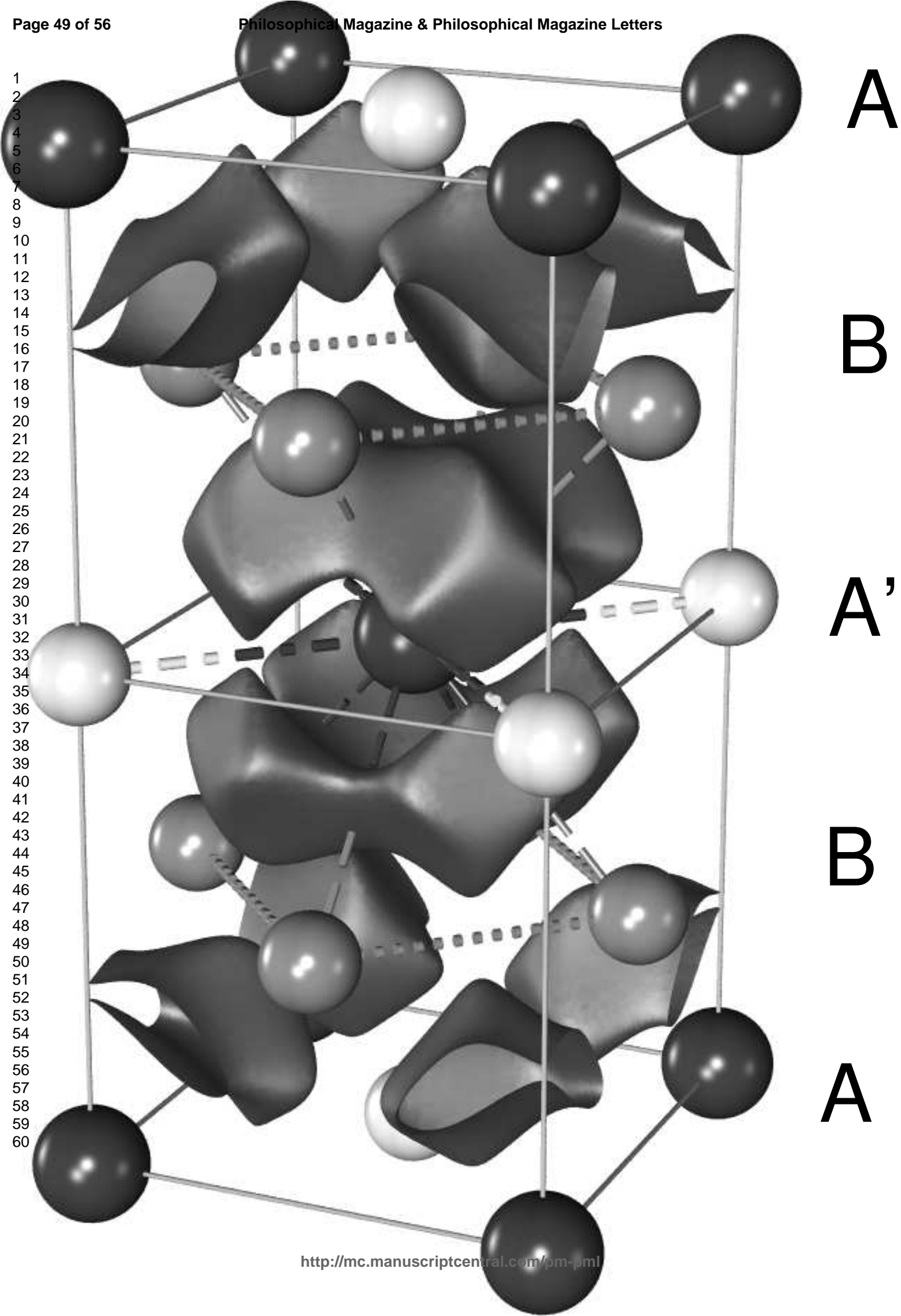
1
2
3
4
5
6
7
8
9
10
11
12
13
14
15
16
17
18
19
20
21
22
23
24
25
26
27
28
29
30
31
32
33
34
35
36
37
38
39
40
41
42
43
44
45
46
47
48
49
50
51
52
53
54
55
56
57
58
59
60

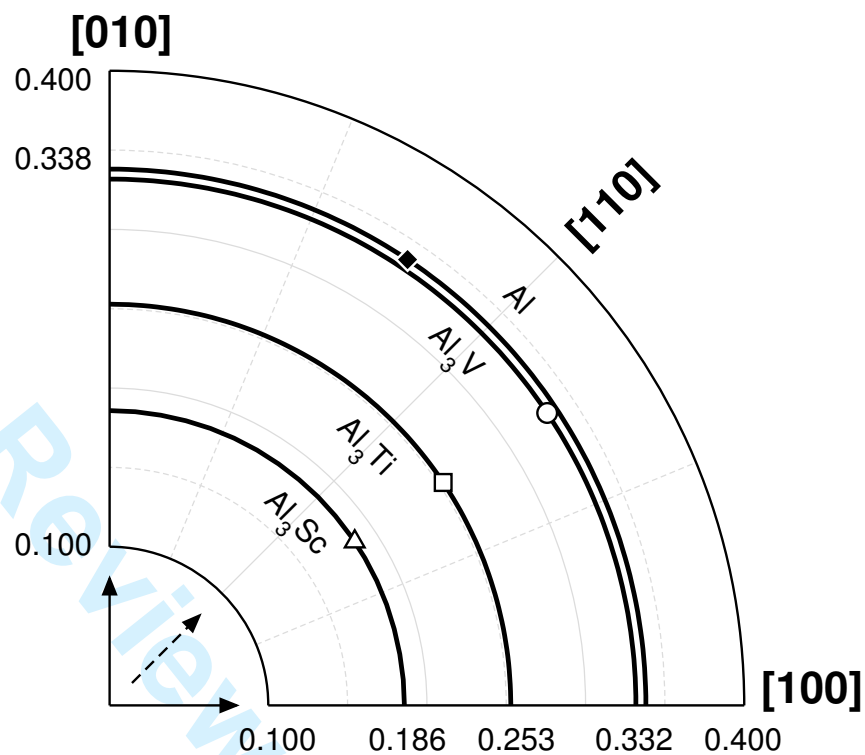


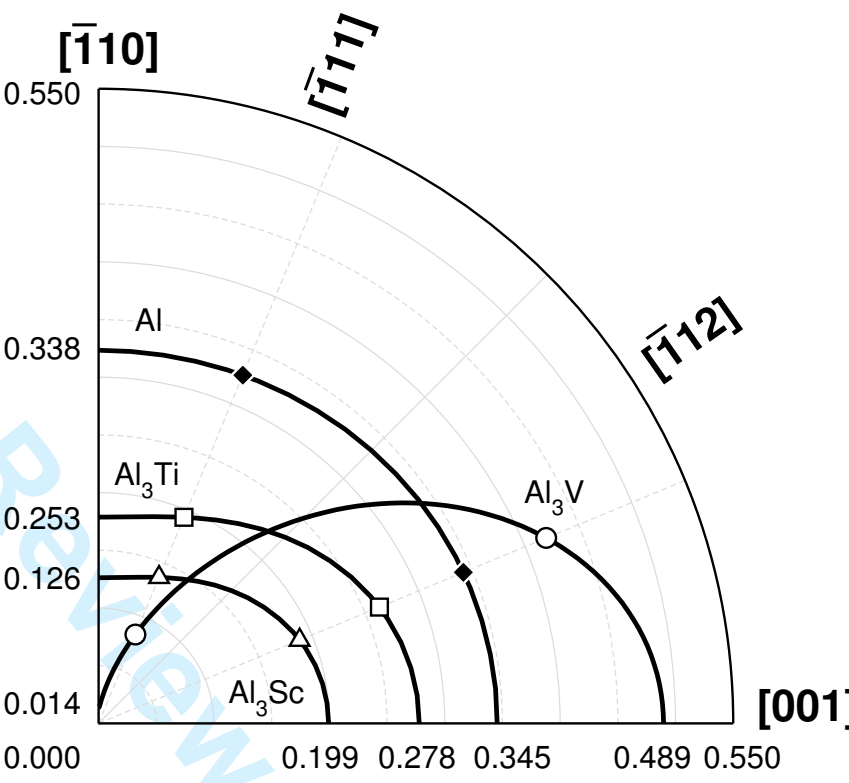
1
2
3
4
5
6
7
8
9
10
11
12
13
14
15
16
17
18
19
20
21
22
23
24
25
26
27
28
29
30
31
32
33
34
35
36
37
38
39
40
41
42
43
44
45
46
47
48
49
50
51
52
53
54
55
56
57
58
59
60

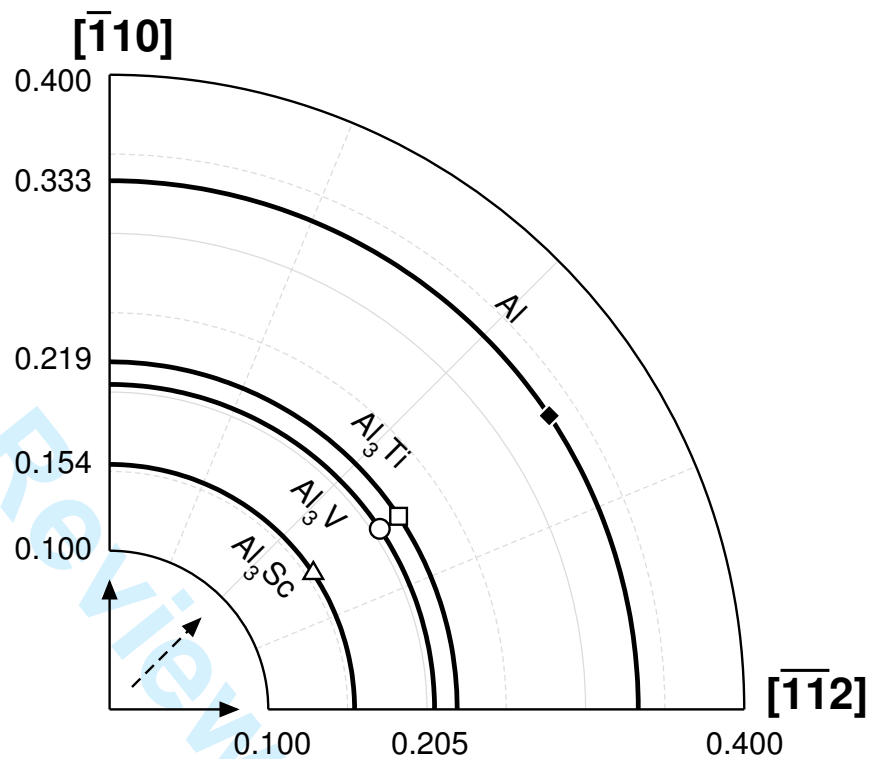


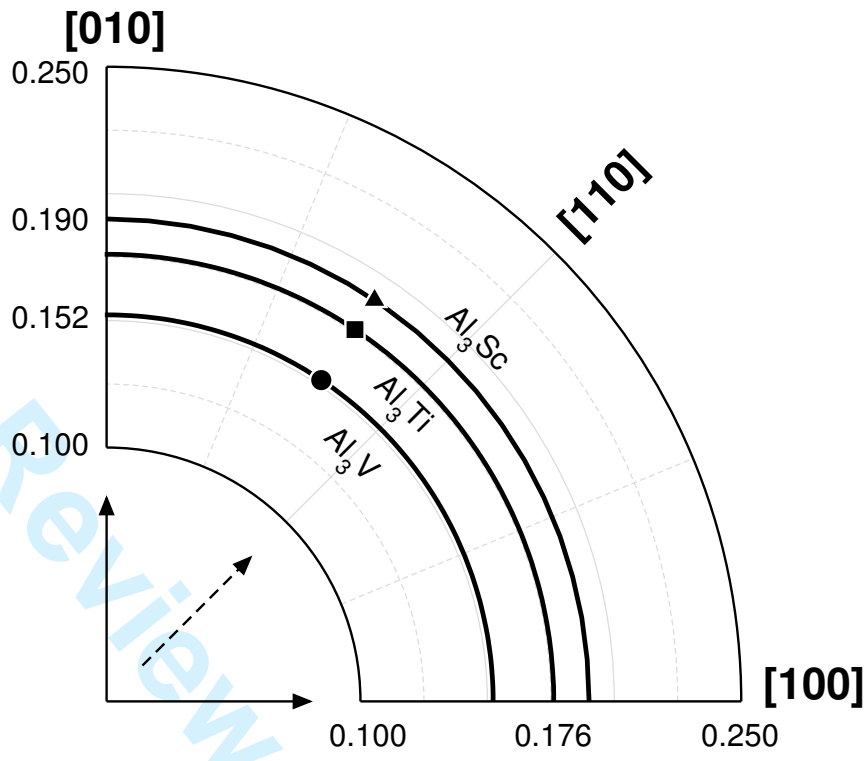
A

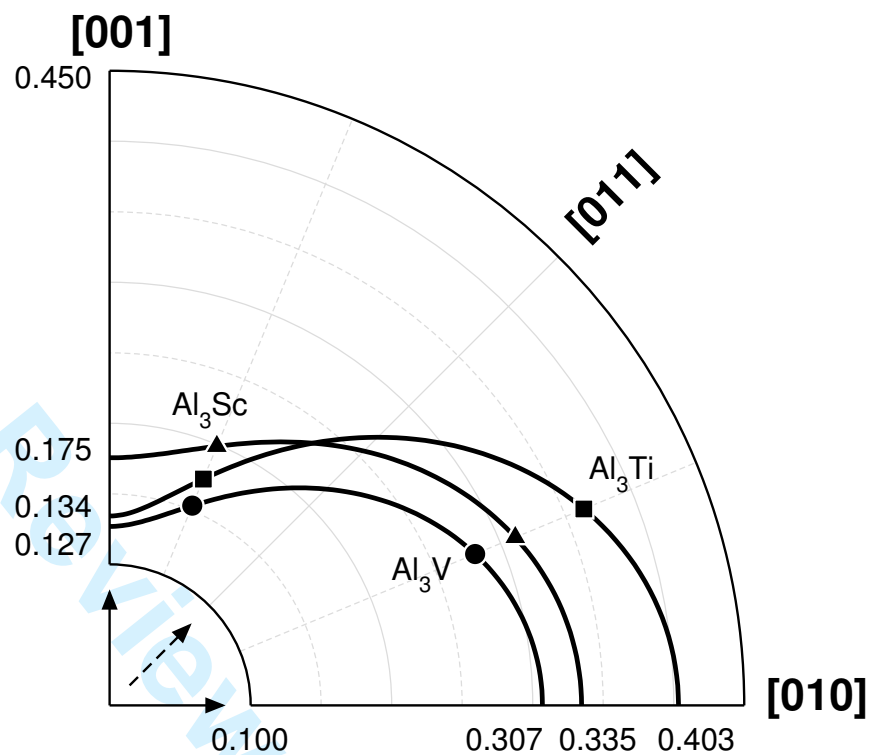


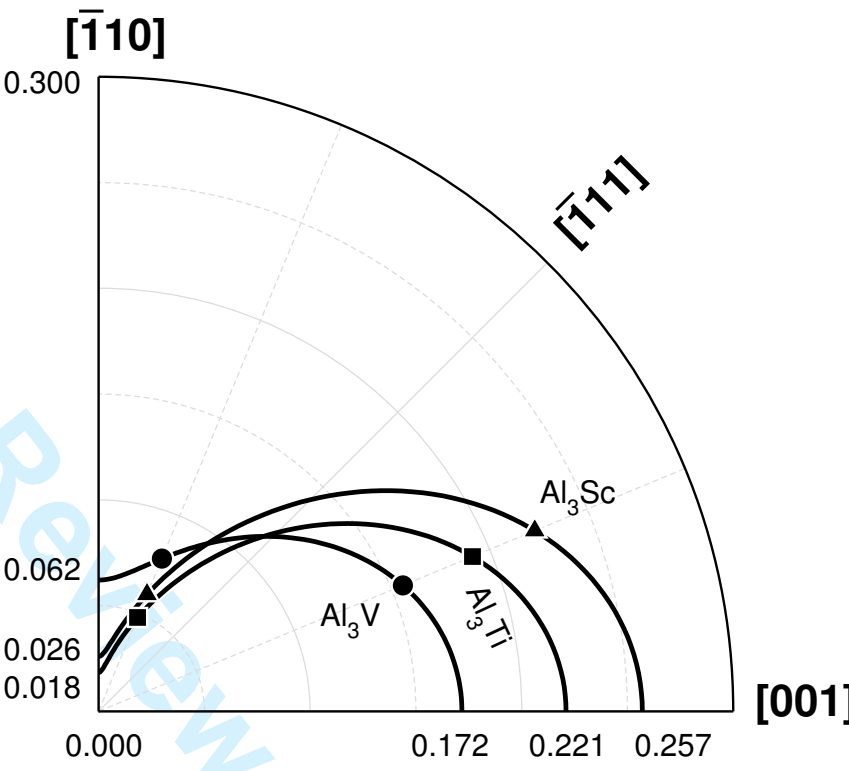


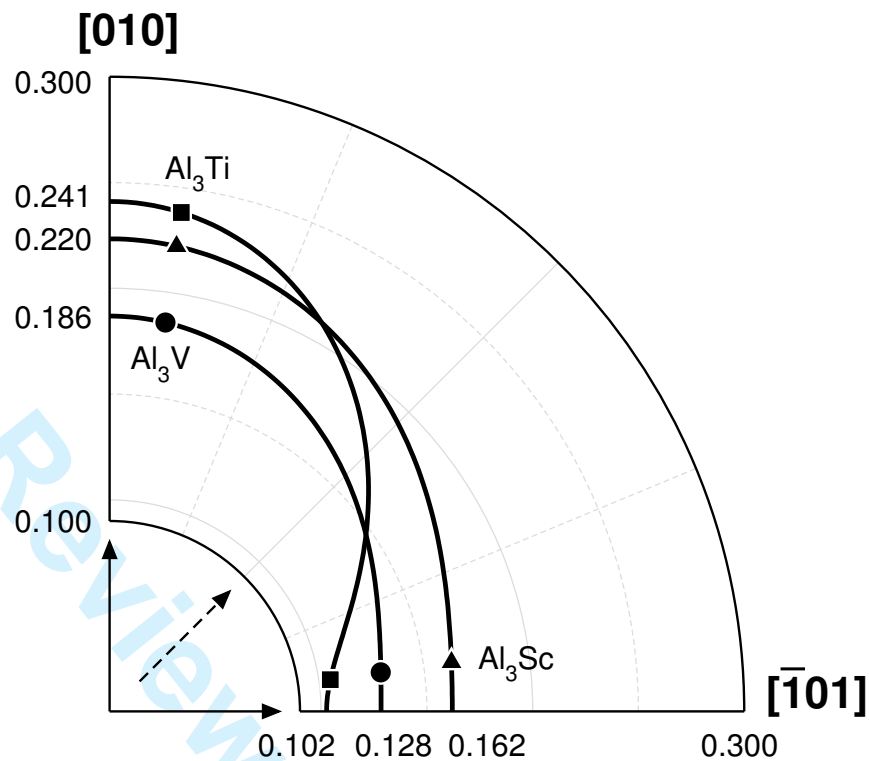












1
2
3
4
5
6
7
8
9
10
11
12
13
14
15
16
17
18
19
20
21
22
23
24
25
26
27
28
29
30
31
32
33
34
35
36
37
38
39
40
41
42
43
44
45
46
47
48
49
50
51
52
53
54
55
56
57
58
59
60

For Peer Review Only

